Electron-Neutrino Angular Correlation Measurement in the Decay of ^{8}Li

Gang Li

A thesis submitted in partial fulfillment

of the requirements for the degree of

Doctor of Philosophy

Department of Physics

McGill University

Montreal, Quebec, Canada

June 1, 2012

ACKNOWLEDGMENTS

Previously when I read other people's acknowledgements, I thought it was a courtesy. After I finished this thesis, I understand it is absolutely not just a courtesy; it is what I really want to say, what I have to say.

I would like to sincerely thank my advisors at McGill: Fritz Buchinger, John Crawford and Jonathan Lee. I would not even know how to start the research in the first year without their encouragement, patience and hands-on help, because I majored in plasma physics in the undergraduate school and realized that the nuclear physics experimental techniques are quite different.

Special thanks should be given to Guy Savard and Ralph Segel. I thank them for the help throughout the whole study, from the experimental design, setup, to the data analysis, and thesis writing. No matter whether it was a theoretical question or a technical difficulty, or even a grammar mistake in thesis writing, they always helped me generously.

I am very thankful to Nicholas Scielzo who preceded me working on this project. Without his previous work, it would have been impossible for me to complete this project. Although our stays at Argonne only overlapped for one week, he has been giving me instructions in every aspect throughout of years.

Many thanks to Jason Clark who coordinated our group for the preparation of the experiment, and did so much work directly for the project. His enthusiasm, conscientious attitude make me sincerely believe our experiment will work well.

Thanks to other scientists and post-docs in Argonne National Laboratory, from whom I received valuable support. Without the discussion with Dariusz Seweryniak, Alan Wuosmaa and Shaofei Zhu I would need a much longer time to know how to operate these detectors.

I am also very thankful to fellow students in our group, with whom I worked together, enjoyed a lot of fun from interesting lab work for 5 years. Specific thanks to Dan Lascar, Jennifer Fallis, Jon Van Schelt for helping me understand the whole system, and for preparation on the front end of my thesis experiment. Special thanks to Shane Caldwell for working together to fulfill the design of my favorite cryogenic pump. Thanks to Matt Sternberg for the computer program and data analysis. Thanks to Ryan Yee for the upgrading of our detector system.

So many people have been involved and it is impossible to recall all of them. I would like to thank Sidney Gulick who came all the way from Montreal to Chicago to help preparing the experiment. My thanks to the operations staff at the ATLAS facility, secretaries, and engineers.

My warm thanks to my Mom and Dad who always supported me for the whole life. Even I am thousands of miles away from them for many years they never complain and have been always willing to help me in everything they can think of.

In conclusion I want to express my most sincere thanks to my beloved wife, Wei Xiao, for unfailing support in my life. She gave up everything she had in China and came here to be with me, took good care of me with incredible patience every day. Without her love and care I wouldn't know how to get through all of these.

TABLE OF CONTENTS

LIST OF TABLES

LIST OF FIGURES

ABSTRACT

The Standard Model has been very successful in describing existing experimental data in nuclear and particle physics, but it still depends on numerous experiments for the determination of several important properties. For example, the assumption that only Vector(V) and Axial-Vector(A) interactions are present out of five possible types of weak interactions: V, A, Scalar(S), Pseudoscalar(P) and Tensor(T) is based on experimental results.

The ion trap is an promising way for precise measurement of the β-ν angular correlation parameter $a_{\beta\nu}$ in beta decay. The unperturbed observation of the recoiled nucleus and electron allows reconstruction of the full decay kinematics. The goal of the BPT (Beta-decay Paul Trap) project is to measure $a_{\beta\nu}$ in the decay of ^{8}Li. A deviation from the predicted value $a_{\beta\nu}$ =–1/3 would be an indication of a tensor contribution.

^{8}Li was produced at the Argonne National Laboratory and about 20,000 events were recorded. By measuring the energy shift of the alpha particles in the ^{8}Li decay, $a_{\beta\nu}$ is determined to be $a_{\beta\nu}$ =–0.329±0.009. This measurement is consistent with the Standard Model prediction. Upgrade of the system for a higher precision measurement is discussed.

RÉSUMÉ

Le Modèle Standard a connu un très grand succès pour décrire les mesures expérimentales autant en physique nucléaire qu'en physique des particules. Cependant, plusieurs expériences tentent toujours de vérifier certaines de ses hypothèses de base. Par exemple, c'est grâce à des résultats expérimentaux, que l'on sait que seules les interactions de type Vecteur (V) et Axial-Vecteur (A) sont présentes dans le Modèle Standard, bien qu'il y a théoriquement trois autres types d'interactions faibles possibles : Scalaire (S), Pseudoscalaire (P) et Tenseur (T).

Les pièges d'ions sont une avenue prometteuse pour mesurer précisément le paramètre de correlation angulaire β-ν, $a_{\beta\nu}$, des désintégrations bêta. L'observation du noyau de recul et de l'électron en l'absence de perturbations externes permet la reconstruction de la cinématique complète des désintégrations. Le but du projet BPT (*Beta-decay Paul Trap*) est de mesurer $a_{\beta\nu}$ à partir de désintégrations d'ions ^{8}Li. Toute déviation des mesures par rapport à la valeur théorique $a_{\beta\nu} = -1/3$ serait une indication d'une contribution d'interactions de type Tenseur.

Des ions ^{8}Li ont été produits au *Argonne National Laboratory*, où près de 20 000 événements ont été enregistrés. En mesurant le décalage énergétique des particules alpha originant de désintégrations ^{8}Li, une valeur de $a_{\beta\nu} = -0.329 \pm 0.009$ a été déterminée pour le paramètre de corrélation angulaire. Cette valeur est en accord avec la prédiction du Modèle Standard. Une amélioration du dispositif pour permettre des mesures de plus grande précision est discutée.

Chapter 1 Standard Model and β decay

Introduction

The purpose of an electron-neutrino angular correlation measurement in β-decay is to determine the form of the weak interaction. The angular correlation between the electron and the neutrino is sensitive to the strength of the various coupling constants that describe the weak interaction.

1.1 Fermi's theory

Beta decay has been a valuable tool in the study of the weak interaction. The first successful theoretical framework for describing the weak interaction was constructed by Fermi in 1934 [1] (the translated English version of [1] is in [2]). His idea of β decay is shown in Figure 1.1,

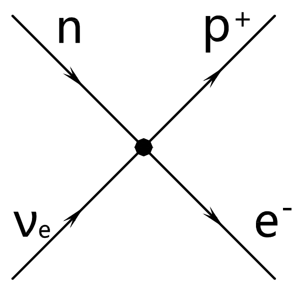

Figure 1.1: Fermi’s 4-point interaction.

which indicates that all the β-processes can be represented in the "Normal Relation":

$$p + e^{-} \leftrightarrow n + \nu \tag{1.1}$$

In analogy to the theory of electromagnetic radiation, which is expressed as the four-vector current $j_u = \bar{\psi}\gamma_u\psi$, Fermi's theory states that the beta decay rate is proportional to the product of two currents, a hadron current $J_H = \bar{\psi}_p O \psi_n$ and a lepton current $J_L = \bar{\psi}_e \mathrm{O} \psi_v$, each current being associated with a charged and a neutral particle:

$$H = g_F(\bar{\psi}_p O \psi_n)(\bar{\psi}_e O \psi_v) + \text{Hermitian Conjugate} \tag{1.2}$$

where ψ_p, ψ_n, ψ_e and ψ_v are the proton, neutron, electron and neutrino wave functions respectively, and g_F is Fermi's fundamental coupling constant, responsible for the magnitude of the interaction, to be determined by experiment.

To determine the operators O, Fermi first imposed the requirement of relativistic invariance, appropriate for a process involving a neutrino which has no rest mass (as thought at that time), which had been previously shown by Pauli [3]. As the simplest assumption, he chose the operator to consist of only bilinear combinations of the Dirac components γ_u given by:

$$\gamma_k = \begin{pmatrix} 0 & -i\sigma_k \\ i\sigma_k & 0 \end{pmatrix}, \text{ k = 1,2,3}$$

$$\gamma_4 = \begin{pmatrix} I & 0 \\ 0 & -I \end{pmatrix} \tag{1.3}$$

$$\gamma_5 = \gamma_1\gamma_2\gamma_3\gamma_4 = \begin{pmatrix} 0 & -I \\ -I & 0 \end{pmatrix}$$

where the σ_k are the 2×2 Pauli spin matrices:

$$\sigma_1 = \begin{pmatrix} 0 & 1 \\ 1 & 0 \end{pmatrix}, \ \sigma_2 = \begin{pmatrix} 0 & -i \\ i & 0 \end{pmatrix}, \ \sigma_3 = \begin{pmatrix} 1 & 0 \\ 0 & -1 \end{pmatrix} \tag{1.4}$$

and I is the 2×2 unit matrix. With these conditions, there are 16 linear independent terms which can be grouped into five classes according to their transformation properties (Table 1.1). According to the transformation properties of $\overline{\psi}_a O_i \psi_b$, they are called Scalar (S), Pseudoscalar (P), Vector (V), Axial Vector (A) and Tensor (T) type weak interactions. A scalar does not change sign under a parity transformation, while a pseudoscalar behaves like a scalar, except that it changes sign under a parity inversion. An example is the longitudinal polarization $\vec{\sigma} \bullet \vec{p}$, where $\vec{\sigma}$ is the spin and $\vec{p}$ is the momentum. Because the momentum changes sign under a parity transformation but the spin does not, the dot product $\vec{\sigma} \bullet \vec{p}$ changes sign and is therefore a pseudoscalar.

Theoretically there is no reason to believe that nature might prefer one type of interaction over another; therefore arbitrary linear combinations of them, each with coefficient C_i are allowed:

$$H = \sum_i g_F C_i (\overline{\psi}_p O_i \psi_n)(\overline{\psi}_e O_i \psi_\nu) + \text{h.c.} \tag{1.5}$$

The Hermitian conjugate (h.c.) in equation (1.5) ensures that β^+-decay is also taken into account.

Type	Operator O_i	Parity	Number of independent matrices
Scalar	1	+	1
Vector	γ_μ	-	4
Tensor	$\gamma_\mu\gamma_\nu - \gamma_\nu\gamma_\mu$	**N/A**	6
Axial vector	$\gamma_\mu\gamma_5$	+	4
Pseudoscalar	γ_5	-	1

Table 1.1: Five types of weak interactions that satisfy the requirement of Lorentz invariance.

Fermi pointed out the possible existence of all of these interaction types. However, in analogy to the electromagnetic interaction where it was known that the currents were vector in nature, and because a vector interaction generally agreed with the experimental data at that time, Fermi chose to use only the vector form of the interaction [1], so he came up with the following Hamiltonian for β decay:

$$H = g_F(\bar{\psi}_p\gamma_\mu\psi_n)(\bar{\psi}_e\gamma^\mu\psi_\nu) + h.\mathrm{c.} \tag{1.6}$$

Just like the electromagnetic interaction, this interaction was invariant under a parity transformation.

1.2 Parity violation

In 1956, when T.D. Lee and C.N. Yang were trying to solve the θ-τ puzzle, they concluded that if parity were not conserved then the θ and τ could just be two different decay modes of the same particle [4]. This led them to examine the evidence for parity conservation. They found that although experiments supported the conservation of parity in the strong and electromagnetic interactions to a high degree of accuracy, there was no evidence in favor of parity conservation in the weak interactions, and they suggested several possible tests [4]. Immediately after Lee's suggestion, C.S. Wu and collaborators devised and carried out their famous experiment on the decay of ^{60}Co and determined that parity conservation is indeed violated [5]. In the same year, two other experiments performed by Garwin et al. [6] on the decay of the μ^+, and by Friedman et al. [7] on the π^+ decay also observed parity violation. Lee and Yang gave a general form of Hamiltonian for beta decay including parity non-conserving terms [4]:

$$\begin{aligned} H_\beta \propto\ & (\bar{\psi}_p \psi_n)(C_S \bar{\psi}_e \psi_\nu + C_S{}' \bar{\psi}_e \gamma_5 \psi_\nu) \\ & + (\bar{\psi}_p \gamma_\mu \psi_n)(C_V \bar{\psi}_e \gamma_\mu \psi_\nu + C_V{}' \bar{\psi}_e \gamma_\mu \gamma_5 \psi_\nu) \\ & + \tfrac{1}{2}(\bar{\psi}_p \sigma_{\lambda\mu} \psi_n)(C_T \bar{\psi}_e \sigma_{\lambda\mu} \psi_\nu + C_T{}' \bar{\psi}_e \sigma_{\lambda\mu} \gamma_5 \psi_\nu) \\ & - (\bar{\psi}_p \gamma_\mu \gamma_5 \psi_n)(C_A \bar{\psi}_e \gamma_\mu \gamma_5 \psi_\nu + C_A{}' \bar{\psi}_e \gamma_\mu \psi_\nu) \\ & + (\bar{\psi}_p \gamma_5 \psi_n)(C_P \bar{\psi}_e \gamma_5 \psi_\nu + C_P{}' \bar{\psi}_e \psi_\nu) \\ & + h.c. \end{aligned} \tag{1.7}$$

where $\sigma_{\lambda\mu} = -\frac{1}{2} i(\gamma_\lambda \gamma_\mu - \gamma_\mu \gamma_\lambda)$. The ten constants C and C' are all real if time-reversal invariance is preserved. The general Hamiltonian of (1.7) contains two types of coupling forms:

$$H^{even} = \sum_i g_F C_i (\bar{\psi}_p O_i \psi_n)(\bar{\psi}_e O_i \psi_\nu) + h.c. \tag{1.8}$$

and

$$H^{odd} = \sum_i g_F C_i' (\bar{\psi}_p O_i \psi_n)(\bar{\psi}_e O_i \gamma_5 \psi_\nu) + h.c. \tag{1.9}$$

The superscripts even and odd refer to the behavior under the parity operation as $\langle H^{even} \rangle$ = scalar and $\langle H^{odd} \rangle$ = pseudoscalar. Let us take a quick look back at the generalized Hamiltonian for β decay proposed by Fermi (1.5), which is also the even part in (1.7):

$$H^{even} = \sum_i g_F C_i (\bar{\psi}_p O_i \psi_n)(\bar{\psi}_e O_i \psi_\nu) + h.c.$$

Notice that the product $(\bar{\psi}_p O_i \psi_n)(\bar{\psi}_e O_i \psi_\nu)$ can take on any type of operator in Table 1.1, but the product of two scalars, the product of two pseudoscalars, or the scalar product of two axial vectors, are all scalars, which means (1.5) is always parity invariant. To obtain an object with odd parity, Lee and Yang added a γ_5 term to construct the pseudoscalar (refer to Table 1.1, γ_5 behaves as a pseudoscalar). After the discovery of parity non-conservation, the coexistence of scalar and pseudoscalar terms is needed to allow the violation of reflection invariance, and all that remains was to decide which interaction terms to include and to determine their constants through experiment.

1.3 V - A theory

Based on a set of experiments after the discovery of parity violation, the idea that the fundamental weak interaction is V-A law was first explicitly presented by Marshak and Sudarshan [8] [9], and independently by Feynman and Gell-Mann [10]. These works extended Fermi's theory to a universal theory which could describe all the weak interactions:

$$H_{V-A} = g_F \left\{ \left[\bar{A}\gamma_\mu (1+\gamma_5) B \right]^\dagger \left[\bar{C}\gamma_\mu (1+\gamma_5) D \right] + h.c. \right\} \tag{1.10}$$

where A, B, C, D are the four Dirac particle fields.

This formulation can be extended to incorporate several generations of fermions by adding more terms. The main statements of this theory are the following:

- Only the vector and axial-vector form of the interaction.
- A universal coupling constant for all weak interactions.
- Maximal parity violation and violation of charge conjugation.
- Massless neutrinos.
- In the relativistic limit v=c all leptons from weak decay are left-handed while all anti-leptons are right-handed.
- Conservation of lepton number.

When they presented the V-A theory, it agreed with all the weak interaction experiments except for four experiments [8]. These four experiments were redone very soon as suggested and by early 1959 all of the experimental evidence from weak interactions – nuclear beta decay, muon decay, pion decay, and electron capture – were generally in agreement with the V-A theory. However, the experimental constraints on the other interaction types (S, P, T) were very loose, and even today a global analysis of data from both neutron and nuclear β decay experiments yielded $|C_S/C_V| < 0.07$ and $|C_T/C_A| < 0.08$ (95.5% C.L.) [11].

1.4 Standard Model description of beta decay

The framework of the Standard Model began in the 1960's with the unification of the weak and electromagnetic gauge theories by Glashow, Weinberg, and Salam [12] [13] [14]. The unified electroweak theory is based on the gauge group

$$SU(2)_L \otimes U(1) \tag{1.11}$$

and both the SU(2) and U(1) symmetries are spontaneously broken. The weak interaction is mediated by three massive vector bosons: the $W^{\pm}$ that mediate the weak charged currents and the Z^0 bosons that mediate weak neutral interactions. The very large mass of $W^{\pm}$ makes this force extremely short-ranged, of the order of $1/M_W \approx 0.003$ fm; therefore Fermi's four fermion contact interaction model is valid to a very good approximation at low energies. The relation of Fermi's coupling constant to the weak coupling constant g_W is $g_F/\sqrt{2} = g_W^2/8M_W^2$. In fact the Standard Model description reduces to the simpler V-A theory in the low energy limit.

In 1970's, the unified electroweak interaction together with a description of the strong interaction became the basis for the Standard Model of particle physics. In the Standard Model there are 12 elementary particles: six leptons and six quarks which can be grouped as follows:

left-handed fermions form the SU(2) quark doublets

$$Q_L^i = \left\{ \begin{pmatrix} u^i \\ d^i \end{pmatrix}_L \right\} = \left\{ \begin{pmatrix} u \\ d \end{pmatrix}_L, \begin{pmatrix} c \\ s \end{pmatrix}_L, \begin{pmatrix} t \\ b \end{pmatrix}_L \right\} \tag{1.12}$$

and lepton doublets

$$L_L^i = \left\{ \begin{pmatrix} \nu_e \\ e \end{pmatrix}_L, \begin{pmatrix} \nu_\mu \\ \mu \end{pmatrix}_L, \begin{pmatrix} \nu_\tau \\ \tau \end{pmatrix}_L \right\}. \tag{1.13}$$

while right-handed fermions form the SU(2) singlets

$$e_R, \mu_R, \tau_R, \nu_{eR}, \nu_{\mu R}, \nu_{\tau R},\ u_R, d_R, c_R, s_R, t_R, b_R$$

The $W^{\pm}$ bosons couple only to the left-handed fermions, leading to the observed maximal parity violation.

The weak eigenstates of the quarks differ from those of the strong or electromagnetic interactions. In 1972, Kobayashi and Maskawa constructed the quark mixing matrix, which is called the Cabibbo-Kobayashi-Maskawa (CKM) matrix, to represent the quark mixing [15]:

$$\begin{pmatrix} d' \\ s' \\ b' \end{pmatrix} = \begin{pmatrix} V_{ud} & V_{us} & V_{ub} \\ V_{cd} & V_{cs} & V_{cb} \\ V_{td} & V_{ts} & V_{tb} \end{pmatrix} \begin{pmatrix} d \\ s \\ b \end{pmatrix}, \tag{1.14}$$

where the prime denotes the weak eigenstates. The normalization of the particle wave-function requires that the CKM matrix be unitary.

The V-A character of the weak interaction is one foundation of the Standard Model. Beta decay experiments have provided critical information in the development of V-A theory, and they are still playing an important role in testing the Standard Model assumptions and in searching for new physics. The β-ν angular correlation experiments are designed to search for physics beyond the V-A description by looking for evidence of Scalar, and Tensor interactions. The pseudoscalar vanishes to lowest order for β-decay in the non-relativistic nucleon limit [16].

1.5 β-ν angular correlation

For the general interaction of (1.7) the decay rate for an allowed β-transition from spin oriented nuclei is given by [17] (only the most important terms are included here):

$$\begin{aligned} & W(\langle\vec{I}\rangle,\vec{\sigma} \mid E_e,\Omega_e,\Omega_\upsilon)dE_e d\Omega_e d\Omega_\upsilon \propto F(\pm Z,E_e)p_e E_e(E_0-E_e)^2 dE_e d\Omega_e d\Omega_\upsilon \times \\ & \xi\left\{1+\frac{\vec{p}_e\bullet\vec{p}_\upsilon}{E_e E_\upsilon}a+\frac{m}{E_e}b+\frac{\vec{I}}{I}\cdot\left[\frac{\vec{p}_e}{E_e}A+\frac{\vec{p}_\upsilon}{E_\upsilon}B+\frac{\vec{p}_e\times\vec{p}_\upsilon}{E_e E_\upsilon}D\right]+\right. \\ & \left.\vec{\sigma}\cdot\left[\frac{\vec{p}_e}{E_e}G+\frac{\vec{p}_\nu}{E_\nu}H+\frac{\langle\vec{I}\rangle}{I}\times\frac{\vec{p}_e}{E_e}R+\ldots\right]\right\} \end{aligned} \tag{1.15}$$

where E, p and Ω denote the total energy, momentum and angular coordinates of the beta particle and the neutrino. E_0 is the total energy carried out by the electron and the neutrino, m is the rest mass of the electron, <I> is the nuclear polarization of the state with spin I, σ is the spin vector of the β-particle and $F(\pm Z, E_e)$ is the Fermi function which takes into account the interaction between the β particle and the nuclear charge. The upper (lower) sign refers to $\beta^-(\beta^+)$-decay. The explanations and expressions for all the coefficients a, b, A, B, D, G, H, R in the allowed approximation can be found in [17].

Parity violation was first observed in the β-asymmetry parameter A with ^{60}Co [5]. Measurement of the β-ν correlation coefficient *a* and Fierz interference term *b* provide ways to search for the V-A forbidden exotic interactions S, and T. The expressions for *a* and *b* are [17]:

$$\xi = |M_F|^2 \left(|C_S|^2 + |C_V|^2 + |C_S'|^2 + |C_V'|^2 \right) + |M_{GT}|^2 \left(|C_T|^2 + |C_A|^2 + |C_T'|^2 + |C_A'|^2 \right) \quad (1.16)$$

$$a\xi = |M_F|^2 \left[-|C_S|^2 + |C_V|^2 - |C_S'|^2 + |C_V'|^2 \right] + \frac{|M_{GT}|^2}{3} \left[|C_T|^2 - |C_A|^2 + |C_T'|^2 - |C_A'|^2 \right] \quad (1.17)$$

$$b\xi = \pm 2\sqrt{1-\alpha^2 Z^2}\ \mathrm{Re}\left[|M_F|^2 (C_S C_V^* + C_S' C_V'^*) + |M_{GT}|^2 (C_T C_A^* + C_T' C_A'^*) \right] \quad (1.18)$$

in which M_F is the Fermi matrix element, M_{GT} is the Gamow-Teller matrix element.

The Fierz interference term *b* is present in the β-ν angular correlation measurements as the way that the measured β-ν correlation coefficient $\tilde{a}$ is:

$$\tilde{a} = \frac{a}{1 + \frac{m_e}{E_\beta} b} \quad (1.19)$$

The Fierz interference term *b* was originally introduced by Markus Fierz [18]. He showed that if both the S and V terms, or both the A and T terms were present in the allowed β-decay, there would be an interference term in the energy spectrum. In the Standard Model the Fierz interference is zero and the recent experimental limit is $b = -0.0022 \pm 0.0026$ [19]. Although the constraint on exotic interactions from *b* may be stringent, *b* will be identically zero if the exotic couplings are purely right handed ($C_i = -C_i'$), while the β–ν correlation is independent of parity, charge conjugation or time reversal violation effects.

Note that if the transition is an allowed β decay that is pure Fermi or pure Gamow-Teller, the β-ν correlation coefficient *a* is independent of the nuclear matrix elements and thus allows a determination of the relative coupling constants independent of any nuclear structure effects. For the unpolarized nuclei undergoing a pure Fermi transition, the correlation is reduced to:

$$a = 1 \quad (1.20)$$

and for pure Gamow-Teller transition:

$$a = -\frac{1}{3} \tag{1.21}$$

Measurements of the β–ν angular correlation [20] [21] [22] provided critical experimental support during the development of V-A theory, and is still an important experimental test of the Standard Model. Until now all these measurements are consistent with the V-A description, as summarized in Figure 1.2.

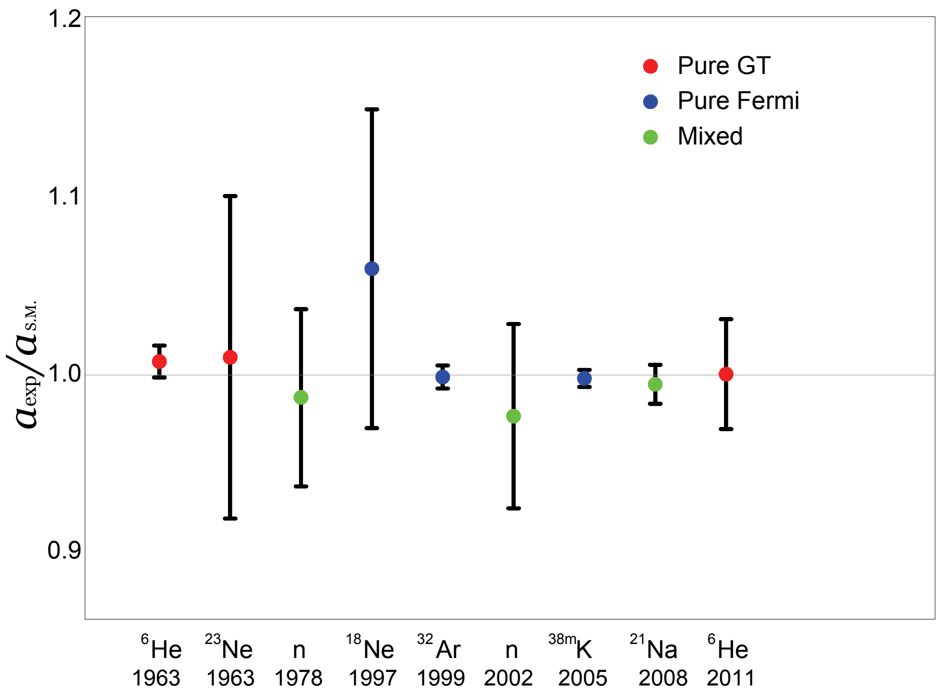

Figure 1.2: Published β-ν angular correlation coefficient $a_{\beta\nu}$ measurements. Only results with better than 10% precision are included. The values are the ratios of measured $a_{\beta\nu}$ and S.M. predicted $a_{\beta\nu}$. The results are sorted by the year when the experiment was performed. The error bars are the quadratic sums of the statistical and systematic uncertainties. The values are from ^{6}He [23], ^{23}Ne [24], n [25], ^{18}Ne [26], ^{32}Ar [27], n [28], ^{38m}K [29], ^{21}Na [30], ^{6}He [31].

1.6 Beyond the allowed approximation

In nuclear β-decay the lepton de broglie wavelength ($\sim 4 \times 10^{2}$ fm at 1 MeV) is much larger than the nuclear radius R($\sim 1.2 \times A^{1/3}$ fm). The lepton wave functions are almost constant over the size of the nuclear. Allowed approximation ignores the change of lepton wave functions over R [16]. This is equivalent to assume that the leptons carry off no orbital angular momentum.

The expressions of (1.16) — (1.18) are under the allowed approximation. Corrections beyond the allowed approximation need to be considered when the precision of the angular correlation measurements reach the ~1% level [32]. The most important corrections are the recoil order terms of order $E_\beta / M_{nuclear}$ arising from the induced weak currents [33], characterized by the weak magnetism form factor b_M and the induced tensor form factor g_{II}. The induced tensor term is expected to be zero due to the absence of second-class currents [33]. How the recoil order corrections affect the β-ν angular correlation coefficient is described by Holstein in Ref. [34].

The order-α (α is the fine structure constant) radiative corrections [35,36] should also be considered in precision angular correlation measurements. The bremsstrahlung photons slightly change the β-decay kinematics and these effects are considerable when the when the end-point energy of the electron is large in comparison with the electron mass. They usually give corrections on the angular correlation parameters on the order of 0.1%.

1.7 ^{8}Li β decay

1.7.1 ^{8}Li decay schematic

As illustrated in Figure 1.3, the $J^\pi = 2^+$ ^{8}Li ground states decay to a 2^+ continuum in ^{8}Be that very rapidly breaks up into 2 α particles: $^8\text{Li} \rightarrow \text{e}^- + \overline{\nu}_e + 2\alpha$ +16.09 MeV. The only other energetically allowed β decays are second forbidden transitions to 0^+ or 4^+ states that can be neglected. The 2^+ continuum is dominated by a ^{8}Be state at about 3 MeV with a width of 1.5 MeV.

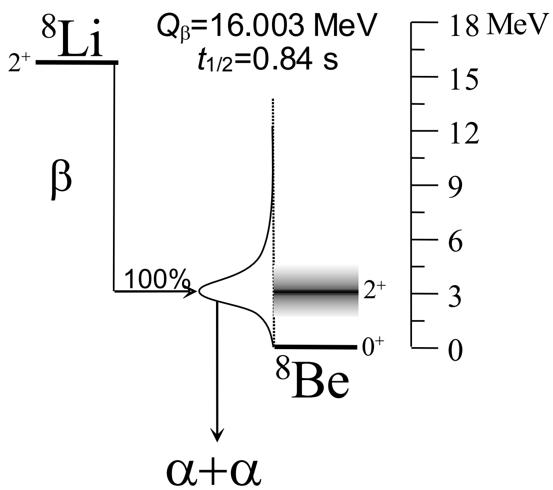

Figure 1.3: ^{8}Li decay schematic. $^8\mathrm{Li} \rightarrow {}^8\mathrm{Be}^* + e^- + \bar{\nu}_e$, $^8\mathrm{Be}^* \rightarrow \alpha + \alpha$

1.7.2 Almost pure Gamow-Teller transition

Conservation of angular momentum and parity permits a mixture at any ratio of an allowed Fermi transition and an allowed Gamow-Teller transition, between the two 2^+ states (Figure 1.3). However, a Fermi transition does not permit a change in isospin and the ^{8}Li ground state is T = 1 while the ^{8}Be 2^+ state is T = 0. The fact that ^{8}Li is $T_z = 1$ prevents its states from having any T = 0 component while in ^{8}Be the nearest 2^+ T = 1 strength is in the 16.6 – 16.9 MeV 2+ doublet and thus isospin mixing is expected to be very small. It has been shown that the transition is predominantly Gamow-Teller [37] [38] and recent *ab initio* calculations have found that the T = 1 component in the ^{8}Be 3.04 MeV state is less than 10^{-3} [39]. As an essentially pure Gamow-Geller transition, the β-decay of ^{8}Li is exclusively sensitive to any tensor contribution.

1.7.3 Large kinematic shifts

^{8}Li is a particularly promising candidate for studying the transformation properties of the weak interaction both because the decay energy is relatively high and because the kinematics of the α-particle decay of the daughter nucleus, ^{8}Be*, permits extraction of the necessary information from the relatively high-energy, easily-detectable α particles, rather than having to detect the recoiling nucleus directly. The large *Q* value and small nuclear mass leads to recoil energies up to 12.2 keV, which is nearly an order of magnitude larger than any of the other decays for which precise β-ν correlation measurements have been made (^{6}He β-decay recoil was the largest at 1.4 keV; the largest recoils in laser trap experiments were 0.43 keV for ^{38m}K [29] and 0.23 keV for ^{21}Na [30]). In the ^{8}Be* rest frame, the α particles are emitted back-to-back with equal energies. However, in the lab frame, the nuclear recoil causes large energy and angular deviation between two alphas. The Doppler shifts as a function of β-ν angle under a variety of kinematic conditions are shown in Figure 1.4. As we can see from Figure 1.4, the angle deviates by as much as 7° from 180° and the energy difference is up to 366 keV. Note that the two decay products of ^{8}Be have equal masses, which maximizes the effect of transferring the ^{8}Be recoil energy to the energy difference between the 2 α's. This effect in ^{8}Li is much larger than in any other species [26,27,40,41] in which the delayed particle (α, photon, or proton) is measured to infer the energy of recoil daughter nucleus.

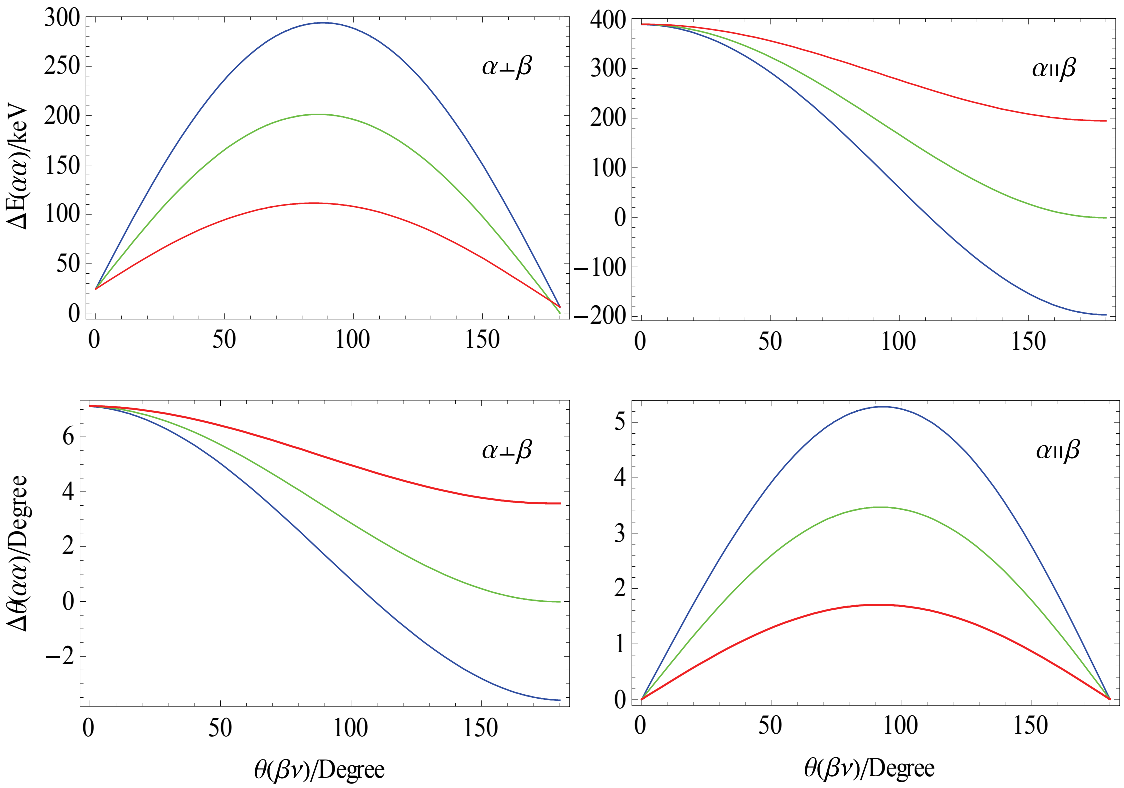

Figure 1.4: Energy difference between the two α particles[top pictures] and difference from 180 degrees in the angle between the two α particles[bottom pictures], for one α exactly perpendicular to the electron momentum[left pictures] and parallel to the electron momentum[right pictures] in coincidence with electrons that have 1/4 (blue) 1/2 (green) and 3/4(red) of the total decay energy.

1.7.4 β-α-α correlation

The β, ν, and daughter nuclei distribution takes the form of (1.15). However, when β's and the α's are detected in coincidence, because the leptons carry away angular momentum, the ^{8}Be nucleus is oriented [42], resulting an additional correlation between the α particles and the leptons, that is described in detail by Morita [43] and Holstein [34]. With the addition of the α-β-$\bar{\nu}$ triple correlation, the decay rate of ^{8}Li in the allowed approximation becomes (equation (53) in Ref. [34]):

$$W \propto 1 + a_{\beta\nu} \frac{\vec{p}_e \bullet \vec{p}_\upsilon}{E_e E_\upsilon} + \frac{1}{10} \tau_{J',J''(L)} \frac{g_{12}}{g_1} \left(\frac{\vec{p}_e \bullet \hat{\alpha} \vec{p}_\upsilon \bullet \hat{\alpha}}{E_e E_\upsilon} - \frac{1}{3} \frac{\vec{p}_e \bullet \vec{p}_\upsilon}{E_e E_\upsilon} \right) \tag{1.22}$$

in which $\hat{\alpha}$ is the unit vector of one α direction, $\tau_{J',J''(L)}$ depends on the spin sequence in the ^{8}Li decay, g_1 and g_{12} are spectral functions defined in [34]. The fact that both the initial and final nuclear states have a spin-parity of 2^+ makes the leptons momenta more likely to be perpendicular to the ^{8}Be spin direction. Because the α's also tend to be emitted perpendicular to the ^{8}Be spin direction, the angular correlation between the β and $\bar{\nu}$ is increased when the β's and the α's are detected along the same axis, as they are in this experiment. In that case the β-ν angular distribution is nearly $W(\theta_{\beta\nu}) \propto 1 + (\vec{p}_e \cdot \vec{p}_\nu)/(E_e E_\nu)$ for a pure tensor interaction and $W(\theta_{\beta\nu}) \propto 1 - (\vec{p}_e \cdot \vec{p}_\nu)/(E_e E_\nu)$ for an axial-vector interaction [44], resulting in a correlation which is a factor of 3 larger than the β-ν correlation coefficient $a_{\beta\nu}$ along. In the other case if the β's and the α's are detected perpendicular with each other, the β-ν angular correlation will not be separated from A or T interactions.

1.7.5 Previous ^{8}Li decay measurements

Before the formulation of the V-A theory in 1957, it had been pointed out that the decay of ^{8}Li is particularly attractive for studying the weak interaction [45]. In 1958, three experiments were performed to identify the vector, tensor, axial vector and scalar contributions in the beta decay. Lauterjung, Schimmer and Maier-Leibnitz measured the β-α-α coincidence rate for the geometry indicated in Figure 1.5 [46] [43], for which the decay rate is represented by:

$$W(\vec{p},\vec{q},\vec{k},E) = F(Z,E)pq^2E[1+\alpha X(\vec{p}\bullet\vec{k}\,/\,E)(\vec{q}\bullet\vec{k}\,/\,q)] \quad (1.23)$$

with $\alpha = 1$ for $2_+ \rightarrow 2_+ \rightarrow 0_+$, and $X=(|C_T|^2-|C_A|^2)/(|C_T|^2+|C_A|^2)$. They concluded that the axial vector is predominant.

Lauritsen, Barnes, *et al*. measured the angular deviation of two α particles from 180° (Figure 1.6) [47]. This measurement could detect the existence of a vector (V) or scalar (S) interaction, but could not distinguish between axial vector (A) and tensor (T) interactions. These authors also concluded that the ground state of ^{8}Li is 2^+ which, at that time, had not been established with certainty. C.A.Barnes *et al*. then measured the α particles momentum spectra in coincidence with the β particles (Figure 1.7) [47]. The distinction between A and T can be made from the α spectra when the β is antiparallel with one of the α's. These two experiments established the ^{8}Li decay to be at least 90% Gamow-Teller and the Gamow-Teller portion is at least 90% axial vector.

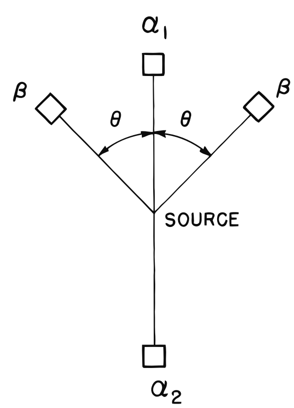

Figure 1.5: Geometry for β-α-α directional correlation adopted by Lauterjung *et al*. All counters are in a plane. The α_1, α_2 and β coincidence rate was measured.

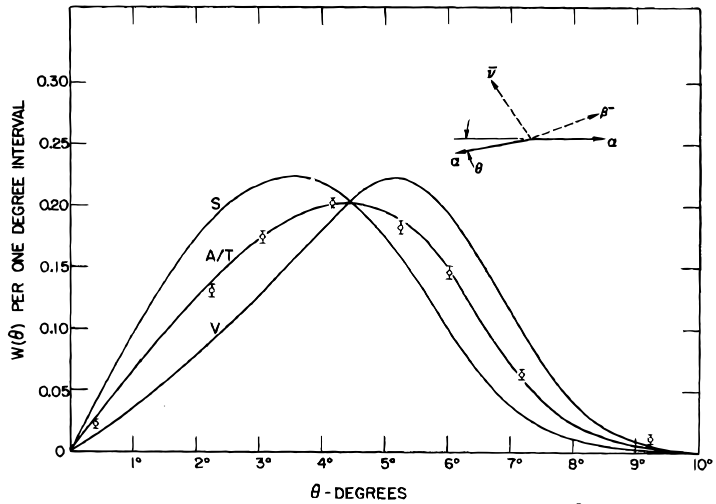

Figure 1.6: Distribution of the two alphas angular deviation θ in ^{8}Li decay. θ is the angular deviation of two α's from 180° in lab frame. The curves labeled with S, V, A/T represent calculations assuming pure scalar interaction, pure vector interaction, and pure axial-vector/tensor interaction respectively. The distributions for A and T interaction are not distinguishable because the angular deviation of two α's are mainly due to recoil effect from leptons momenta perpendicular with α momentum. As discussed in section 1.6.4, this configuration will not separate A and T interactions. Figure is from Lauritsen, Barnes, *et al.* [47]

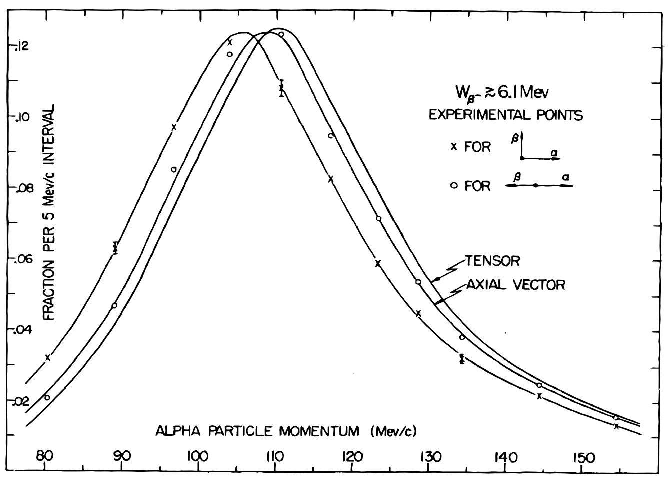

Figure 1.7: α momentum spectrum obtained in the β-α coincidence measurement in [47].

Before the development of trap technology, the β-ν angular correlation measurements were very difficult to perform precisely. In the case of solid sources, the energy loss and scattering make it difficult to measure the recoil nucleus momentum. If the radioactive nucleus is contained in a gaseous media, the gas tends to fill the whole volume, causing difficulties in reconstructing the angles of the emitted particles. With present atom and ion trap technology, the decay products can be detected at rest and at known position with minimal disturbance and scattering, allowing the determination of the full decay kinematics. Ion traps and their working principles will be discussed in the following chapter.

Chapter 2 Ion traps

In β-ν angular correlation measurements the neutrino cannot be directly observed. However, detecting the emitted electron and recoiling nucleus makes it possible to reconstruct the neutrino direction and energy based on energy and momentum conservation. This requires that both the electron and the recoil be detected without any perturbation, and the parent nucleus be at rest at a known position. All of these requirements can be met by performing the measurement in a Linear RFQ (Radio Frequency Quadrupole) ion trap (also called a Linear Paul trap). To collect, transfer the radioactive ions of interest after they are created and separate them from other ions, the RFQ ion guide and Penning trap are used in our system. This chapter will discuss the principles of these devices.

2.1 Basic principles of ion trapping

The confinement of a charged particle requires an electric field that has a potential minimum (or maximum for negative ions) in all three dimensions. The only static field that has a potential minimum in all direction from a point is that produced by a localized electric charge. This is the 'trap' produced by an atom for its surrounding electrons and the gravity potential has the same form. In an atom the electrons have sufficient kinetic energy to maintain their orbits, but our measurement requires that ions have minimum kinetic energy at the trap center. Furthermore, the trap center must be a vacuum so that the decay particles do not lose energy or change direction.

In electrostatic fields, we know from Maxwell's equations or Gauss's law:

$$\nabla \bullet E = 0 \tag{2.1}$$

Therefore there is no local minimum (or maximum) in the potential of a static field:

$$\nabla^2 \Phi = 0 \tag{2.2}$$

This result is often referred as Earnshaw's theorem. If a potential minimum is created at a particular point in one direction, it must have a potential maximum at the same point in some other direction.

There are several methods to overcome the impossibility of making a trap by static electric fields. One way is to use an oscillating electric field, rather than a static one. Such a trap is called an RF (radio frequency) Paul trap. Another way is to use a combination of static electric fields and static magnetic fields, in a structure called a Penning trap. Both types of trap are used in our system and their principles are discussed in this chapter.

2.2 The RFQ ion Guide

2.2.1 The quadrupole field

In principle, any oscillating field with a local minimum potential can be used to confine ions. The simplest form of such fields is the quadrupole field which provides simple harmonic motion with angular frequency ω_{rf}:

$$\Phi_{rf} = \Phi \cdot \cos(\omega_{rf} t) = \Phi_0 (\lambda x^2 + \sigma y^2 + \gamma z^2) \cdot \cos(\omega_{rf} t) \qquad (2.3)$$

in which λ, σ, and γ are weighting constants and Φ_0 is a position independent coefficient. In a charge-free vacuum, the Laplace condition $\nabla^2 \Phi = 0$ restricts the constants:

$$\lambda + \sigma + \gamma = 0 \qquad (2.4)$$

Here the simplest non-trivial solution is:

$$\lambda = -\sigma; \; \gamma = 0 \qquad (2.5)$$

which is the condition used in the RFQ ion Guide. Then the potential can be expressed as:

$$\Phi = \Phi_0 (\lambda x^2 - \sigma y^2) \qquad (2.6)$$

A boundary condition of the same form as equation (2.6) will produce the potential over a region in space. This can be achieved by four hyperbolic cylindrical electrodes as shown in Figure 2.1.a. If the distance between opposite electrodes is selected to be $2r_0$ and the potential difference between neighboring electrodes is Φ_0, the potential can be rewritten as:

$$\Phi = \frac{\Phi_0}{2r_0^{\,2}} (x^2 - y^2) \qquad (2.7)$$

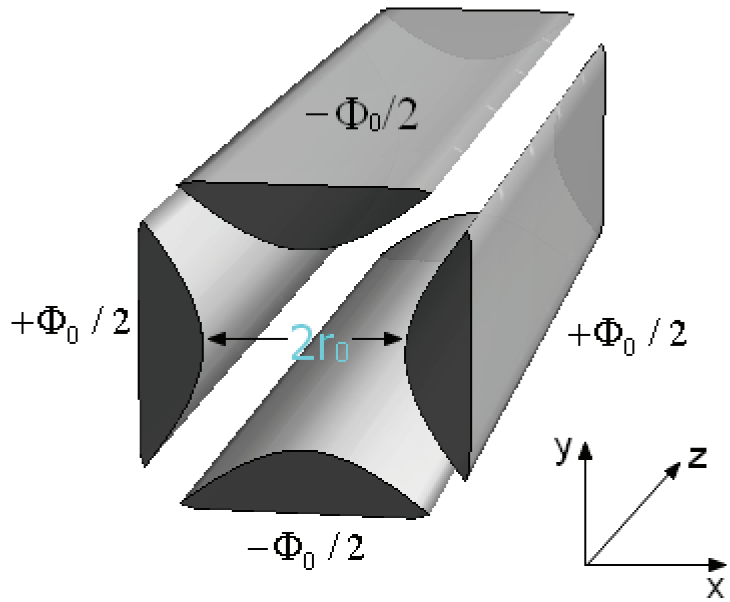

Figure 2.1: (a) electrode structure used to produce a quadrupole field.

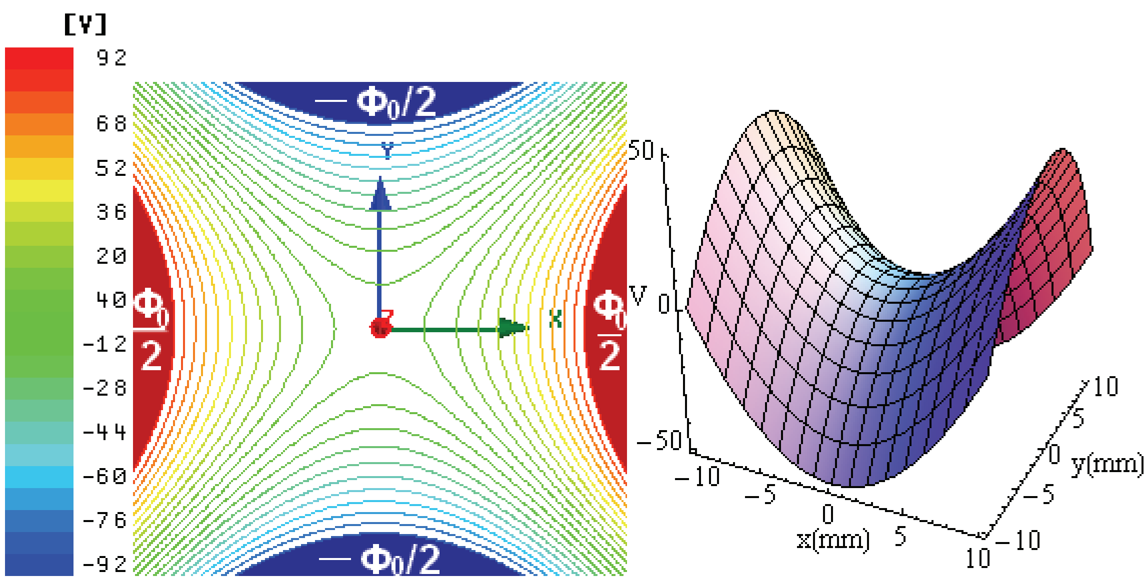

2.1(b) 2.1(c)

Figure 2.1(b) Cross section view of the isopotential lines of the field produced by the electrodes of (a) with r_0=10mm, and Φ_0=100V. (c) Hyperbolic potential 3d plot of the field in (b).

The ions are confined in two dimensions in such a device, while in the axial direction the motion remains free. Therefore, this device is usually referred to as an RFQ ion guide. If the correct value DC voltage is added to the RF voltage on the electrodes, the ion confinement can be mass-dependent. In this case, this device is usually called an RFQ mass filter.

For technical reasons, usually the hyperbolic cylinder electrodes are replaced with circular rods with radius r = 1.148r_0 [48] where r_0 is the distance from the rod edge to the trap axis. The potential in the central region agrees well with that of an ideal quadrupole field [49].

2.2.2 Ion motion

The voltage applied to an RFQ mass filter is the combination of DC voltage U and RF voltage V with angular frequency Ω:

$$\Phi_0 = U - V\cos\Omega t \tag{2.8}$$

In Cartesian coordinates, an ion with positive charge e and mass m has independent motions in the two directions:

$$\begin{aligned} &\ddot{x} + \frac{e}{mr_0^2}(U - V\cos\Omega t)x = 0 \\ &\ddot{y} - \frac{e}{mr_0^2}(U - V\cos\Omega t)y = 0 \\ &\ddot{z} = 0 \end{aligned} \tag{2.9}$$

We can define two dimensionless parameters:

$$\begin{aligned} a = a_x = -a_y = \frac{4eU}{m\Omega^2 r_0^{\,2}} \\ q = q_x = -q_y = \frac{2eV}{m\Omega^2 r_0^{\,2}} \end{aligned} \tag{2.10}$$

and with the substitution t=2ξ/Ω, equations (2.9) are transformed into:

$$\frac{d^2u}{d\xi^2} + (a - 2q\cos 2\xi)u = 0 \tag{2.11}$$

where u represents either x or y. This is the Mathieu equation and its solutions can be expressed as the following form:

$$u(\xi) = Ae^{\mu\xi}\sum_{n=-\infty}^{\infty} C_{2n}e^{2in\xi} + Be^{-\mu\xi}\sum_{n=-\infty}^{\infty} C_{2n}e^{-2in\xi} \tag{2.12}$$

where A and B are constants that depend on the initial conditions, while the real constant C_{2n} and the complex constant μ=α+iβ depend only on the parameters a and q.

Ion confinement requires a stable solution which means that u(ξ) remains finite as

$\xi \to \infty$. The requirement is satisfied when μ is a purely imaginary μ=iβ and β is not an integer. The condition of β being an integer in μ=iβ forms the boundary between the stable and the unstable region and generally it is unstable. β can be simply approximated as [50]:

$$\beta = \sqrt{a + (q^2 / 2)} \tag{2.13}$$

Since μ only depends on *a* and *q*, the stability region can be represented by a and q, shown as shaded regions in the a-q diagram in Figure 2.2.

RFQ devices usually operate in the lowest stability region, which is the region between $0<\beta_x<1$ and $0<\beta_y<1$ (as shown in Figure 2.3). Equation (2.10) implies:

$$\frac{a}{q} = \frac{2U}{V} \tag{2.14}$$

which is shown with an operating line in the a-q diagram (Figure 2.3). Only when the q value is between q_{min} and q_{max}, is the trap stable. For a specific operation condition, the trap geometry, DC and RF are fixed, so the only parameters that affect the q value are the mass and charge state, as can be seen in equation(2.10). By applying the correct U and V the range of masses which have stable trajectories can be selected.

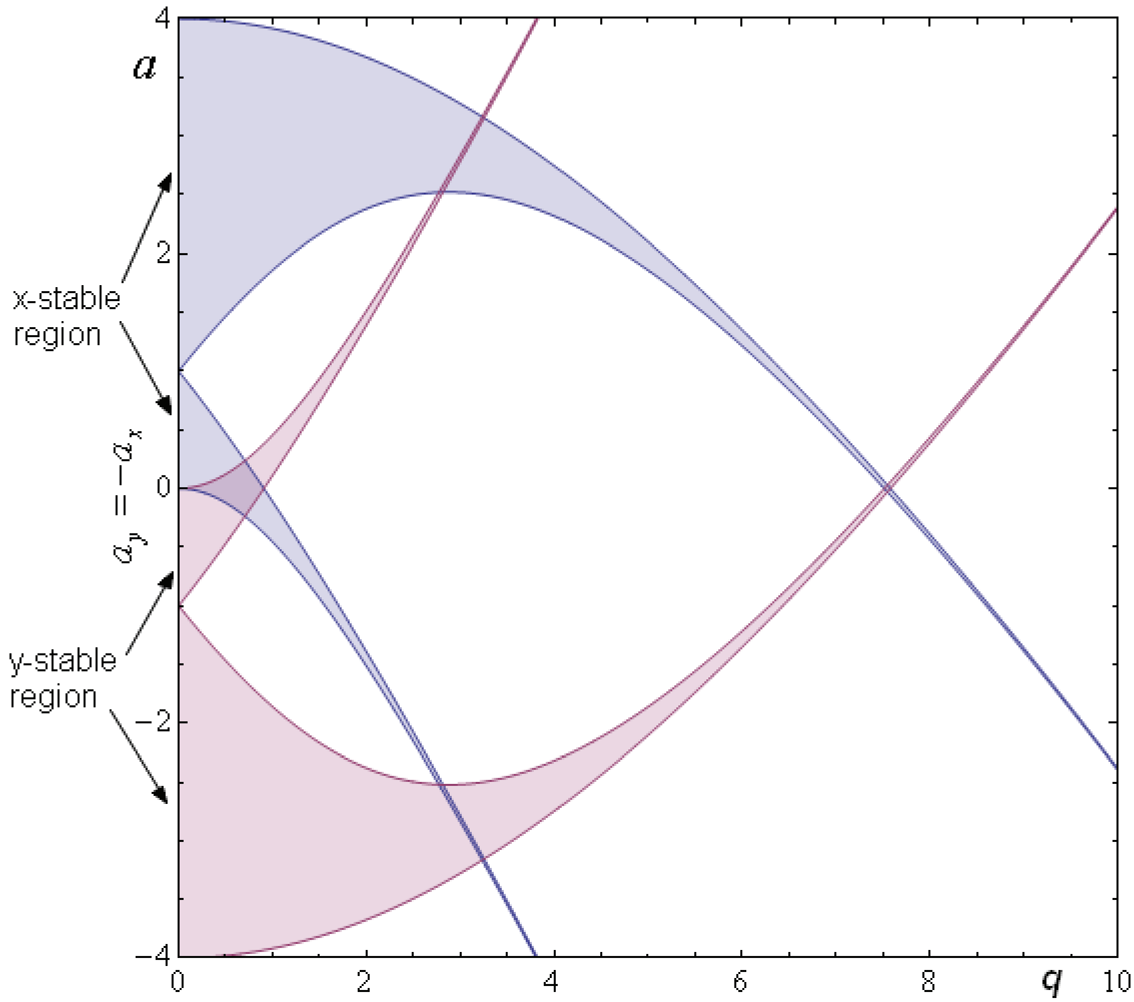

Figure 2.2: The stability regions for the RFQ ion guide. Confinement requires that motion is stable in both x and y directions which is indicated by the overlapped shaded regions. The first overlap region around a=0 and 0<q<0.908 is called the lowest stability region.

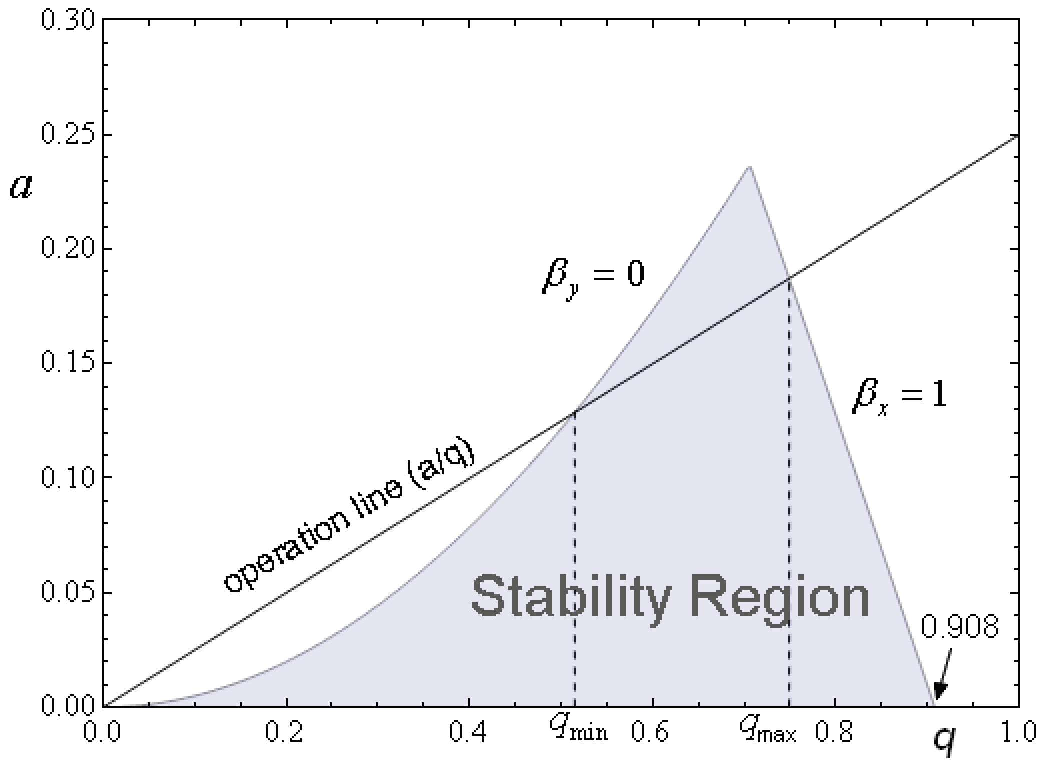

Figure 2.3: Lowest stability region of Mathieu equation and showing an RFQ ion guide operation line. Between q_{min} and q_{max} ions are stably confined.

In the stable region, by substituting μ with μ=iβ, the general form of solutions of (2.12) becomes:

$$u(\xi) = A\sum_{n=-\infty}^{\infty} C_{2n}e^{(2n+\beta)i\xi} + B\sum_{n=-\infty}^{\infty} C_{2n}e^{-(2n+\beta)i\xi} \tag{2.15}$$

The real part of equation (2.15) represents the ion trajectory:

$$u(\xi) = (A+B)\sum_{n=-\infty}^{\infty} C_{2n}\cos(2n+\beta)\xi \tag{2.16}$$

This shows that the ion trajectory is a superposition of oscillations with frequencies ω_n at:

$$\omega_n = (2n+\beta)\frac{\Omega}{2}\text{, n = 0, 1, 2 . . .} \tag{2.17}$$

For a low β value, the lowest two frequencies are dominant in the solution, as illustrated in Figure 2.4(a). The lowest frequency component ω_0 is called the macro oscillation, or secular oscillation with frequency:

$$\omega_0 = \beta \frac{\Omega}{2} \approx \sqrt{a + \frac{q^2}{2}} \frac{\Omega}{2} \tag{2.18}$$

Some typical schematically calculated ion trajectories are shown in Figure 2.4.

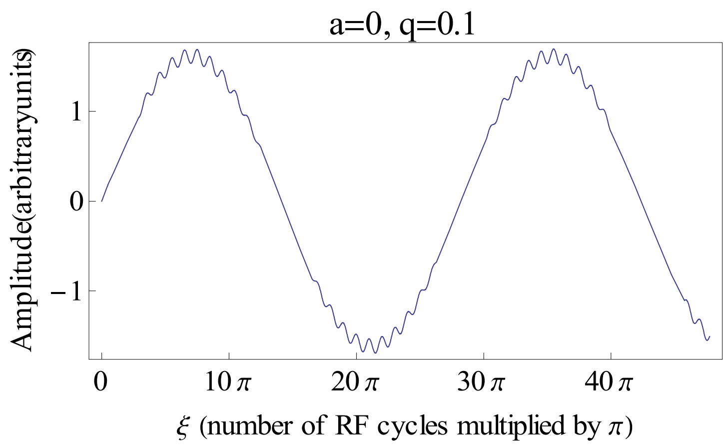

(a)

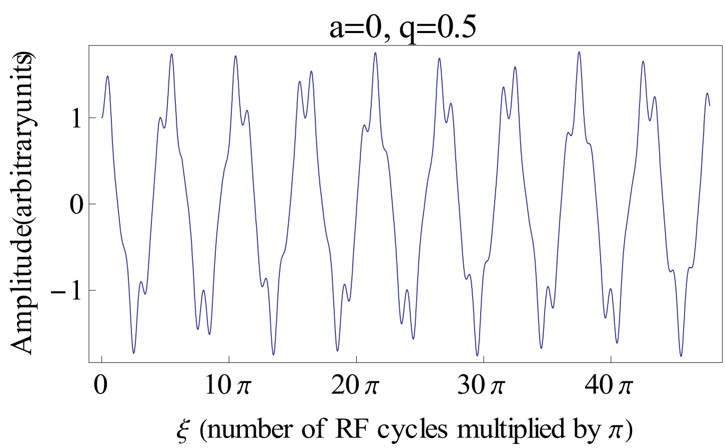

(b)

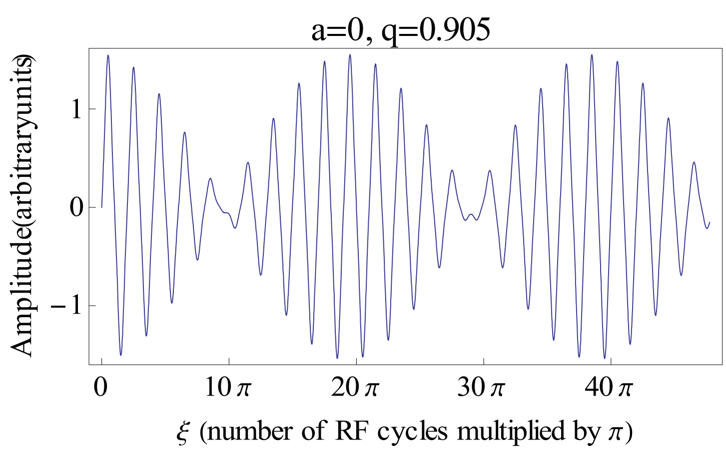

(c)

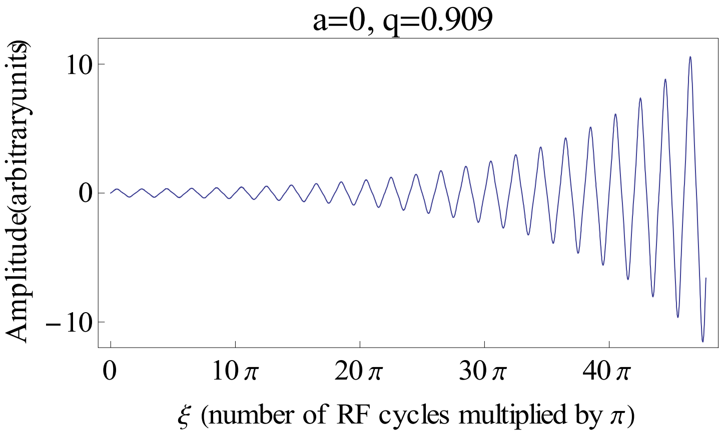

(d)

Figure 2.4: Typical calculated ion trajectories for several points in the stability diagram. (a)With low q value, the lowest two frequencies play the major role. (b) Micro-motion is large and other higher frequencies visually show up. (c) q is close to the boundary of the stability region. (d) an unstable trajectory.

2.2.3 Pseudo-potential model

Where the first two lowest frequencies play the leading role in ion motion, (as in Figure 2.4(a)), the macro oscillation can be approximated with the pseudo-potential model (as shown in Figure 2.5), which suggests that the ion motion can be considered as a harmonic oscillation in a parabolic potential well [51]. This approximation is valid when $a, q \ll 1$.

We can consider the ion motion u to be composed of two components:

$$u = \Gamma + \delta \tag{2.19}$$

where Γ represents the macro motion, and δ represents ripple on the macro motion resulting from the RF field oscillations. In the following calculation, assume:

$$\delta \ll \Gamma \qquad \text{(as Figure 2.4a)} \tag{2.20}$$

$$\frac{d\delta}{dt} \gg \frac{d\Gamma}{dt} \qquad \text{(as Figure 2.4a)} \tag{2.21}$$

$$a \ll q \qquad \text{(as Figure 2.3, when q<<1)} \tag{2.22}$$

and

$$\int_0^{2\pi} \frac{d^2\delta}{dt^2} = 0 \tag{2.23}$$

Equation (2.23) means that over an RF period the acceleration of micro-motion is zero relative to the secular trajectory.

Equation (2.11) can be approximated as:

$$\frac{d^2\delta}{d\xi^2} = -(a - 2q\cos 2\xi)\Gamma \tag{2.24}$$

Assuming a<<q and assuming Γ is constant compared with δ, (2.24) can be integrated to obtain:

$$\delta_{(\xi)} = -\frac{q_u\Gamma}{2}\cos 2\xi \tag{2.25}$$

This indicates that the displacement of the micro motion is out of phase with the RF potential by half a cycle, so the RF potential is always trying to drag the ion back. This indicates why the ion can be confined. Substituting (2.21) and (2.19) into the Mathieu equation (2.11):

$$\frac{d^2u}{d\xi^2} = \frac{d^2\Gamma}{d\xi^2} + \frac{d^2\delta}{d\xi^2} = -a_u\Gamma + \tfrac{1}{2}a_u q_u\Gamma\cos 2\xi + 2q_u\Gamma\cos 2\xi - q_u{}^2\Gamma\cos^2 2\xi \tag{2.26}$$

Averaging over a period of RF, only terms containing Γ and $\cos^2$ survive:

$$\frac{1}{2\pi}\int_0^{2\pi}\left(\frac{d^2\Gamma}{d\xi^2} + \frac{d^2\delta}{d\xi^2}\right) = \frac{1}{2\pi}\int_0^{2\pi}\left(-a_u\Gamma + \tfrac{1}{2}a_u q_u\Gamma\cos 2\xi + 2q_u\Gamma\cos 2\xi - q_u{}^2\Gamma\cos^2 2\xi\right)$$

$$\Rightarrow \frac{d^2\Gamma}{d\xi^2} = -\left(a + \frac{q^2}{2}\right)\Gamma \qquad \text{(with the assumption (2.23) } \int_0^{2\pi}\frac{d^2\delta}{dt^2} = 0\text{)} \tag{2.27}$$

$$\Rightarrow \frac{d^2\Gamma}{dt^2} = -\left(a + \frac{q^2}{2}\right)\frac{\Omega^2}{4}\Gamma \qquad \text{(with the substitution of t=}\frac{2\xi}{\Omega}\text{)} \tag{2.28}$$

$$\Rightarrow \frac{d^2\Gamma}{dt^2} = -\omega_0{}^2\Gamma \qquad \text{(from equation (2.18) } \omega_0 = \sqrt{a + \tfrac{1}{2}q^2}\,\frac{\Omega}{2}\text{)} \tag{2.29}$$

where ω_0 is the macro oscillation frequency and is also the lowest frequency component in the solution of the Mathieu equation.

The basic equation of motion of an ion with mass m and charge e in an electric field $\overline{D}_u$ is:

$$\frac{d^2\Gamma}{dt^2} = -e\frac{d\overline{D}_u}{d\Gamma} \tag{2.30}$$

In the case of *a*=0, comparing (2.27) and (2.30), we get:

$$\frac{d\overline{D}_u}{d\Gamma} = \frac{q^2\Omega^2\Gamma m}{8e} \tag{2.31}$$

Substituting q from (2.10) and integrating Γ from 0 to r gives:

$$\overline{D}_{u(r)} = \frac{eV^2}{4mr^2\omega^2} \tag{2.32}$$

where $\overline{D}_u$ is called the pseudo-potential. When r = r_0, $\overline{D}_{u(r_0)}$ is the maximum potential that an ion can reach without hitting the trap electrodes. In the pseudo-potential model, the ion macro motion is equivalent to that in a static parabolic potential well. Since the static field is more intuitive than the RF field (as seen in Figure 2.5), this model is usually used for a simple estimate of the trap depth for an RF field. It also provides an estimate of the maximum allowed kinetic energy $E_{K(max)}$ of the trapped ions [52]:

$$E_{k(\max)} = e\overline{D}_{u(r_0)} \tag{2.33}$$

On the other hand, if the ions kinetic energy E_{kin} is roughly known, for example after the ions reach thermal equilibrium with a buffer gas, the ion cloud dimension can be estimated

$$\overline{D}_{u(r=x)} = E_{kin} / e \tag{2.34}$$

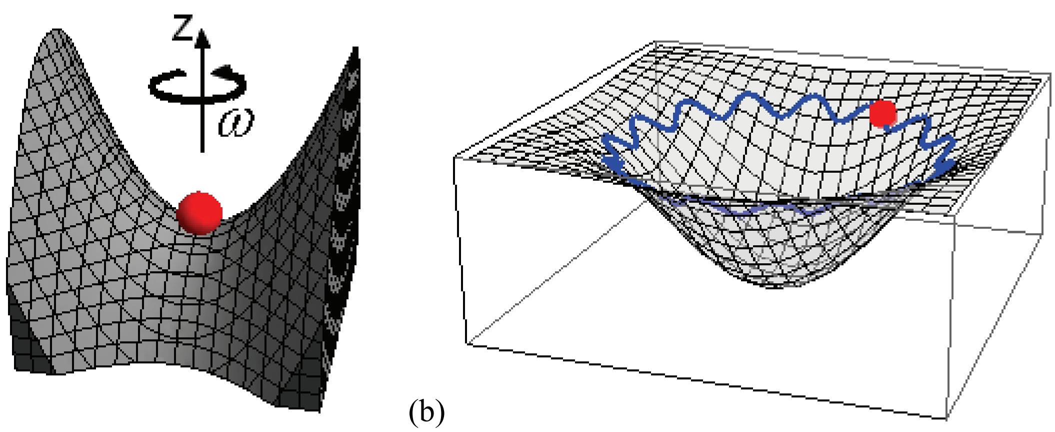

(a) (b)

Figure 2.5: (a) Oscillating hyperbolic potential confining ions. (b) The effect of confinement is approximated by a pseudo-potential well. The ion trajectory is indicated by the blue curve. The secular motion can be explained using the pseudo-potential plotted in (b). The micro motion is due to the RF oscillation.

2.2.4 Buffer gas cooling

All the ion guides and traps in our system are operated with helium buffer gas. Ions lose kinetic energy through collisions with this gas. When heavy ions move in low mass buffer gas, the average effect on the motion of a low velocity ion is a drag force F_d which is proportional to the velocity v:

$$F_d = \frac{e}{K} v \tag{2.35}$$

where e is the ion charge and K is referred to as the "ion mobility", which describes how easily an ion can drift in the gas. When an ion drifts in a gas under a uniform electric field E it will reach a final drift velocity v_d; then the ion mobility is defined as $K = v_d/E$. Standard values of ion mobility for various ions in different gases are available from a large amount of experimental data. These values are usually measured under standard pressure and temperature (i.e. at the density of 2.69×10^{19} cm^{-3}) and they are referred as "reduced mobility" K_0. The actual mobility K at an experimental condition is related to the reduced mobility as:

$$K = \frac{p_{std}}{p} \frac{T}{T_{std}} K_0 \tag{2.36}$$

In a buffer gas, the average motion under the quadrupole electric field can be approximated by $m\ddot{x} = -\frac{e}{K}\dot{x} + eE$, so equation (2.11) becomes:

$$\frac{d^2u}{d\xi^2} + 2k\frac{du}{d\xi} + (a - 2q\cos 2\xi)u = 0 \tag{2.37}$$

in which $k = e/(mK)$.

With the substitution $u_1 = ue^{k\xi}$ and $a_1 = a - k^2$, the above equation remains a Mathieu equation:

$$\frac{d^2u_1}{d\xi^2} + (a_1 - 2q\cos 2\xi)u_1 = 0 \tag{2.38}$$

Here, stability depends on a_1 and q, which means that the buffer gas contributes to the stability of the ion motion. The full solution is $u = u_1 e^{-k\xi}$, including an exponential damping. The ion trajectories collapse into the trap center.

The use of buffer gas has multiple benefits in our system, for example: (a) In the RFQ ion guide, because the ions are centered, the transfer efficiency is increased, especially when there is a small aperture at the exit of the ion guide as is the case in our ion guide. (b) In the 3-dimensional ion trap, which will be discussed next, the trap lifetime is enhanced by reducing the ion kinetic energy, which has been recognized since the earliest experiments with Paul traps [53]. There are two reasons for the increased lifetime: first, the reduced ion trajectory prevents the ion from escaping the trap, and second, at the trap center the field is closer to the ideal hyperbolic field. (c) In the process of capturing the injected ions the excess energy of the injected ions is reduced via buffer gas cooling. This was first described by March and co-workers [54].

2.3 The linear Paul trap

The RFQ ion guide confines ions in two dimensions, while in the axial direction the ions remain free to move. To trap the ions, three-dimensional confinement is required, which can be achieved by the linear Paul Trap. Generally a linear Paul trap is just a RFQ ion guide with dc voltage confinement along the axial axis, as sketched in Figure 2.6. The linear Paul Trap can be used as a mass filter, or as an actual three-dimensional trap.

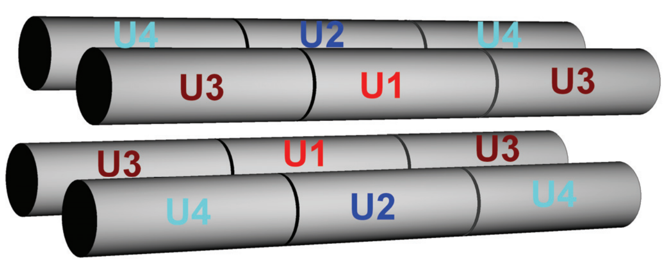

Figure 2.6: Linear Paul trap. Each rod is segmented into three parts, allowing DC voltage to be applied along the axial direction. The voltages applied on the electrodes are: $U_1=-1/2V\cos\Omega t$, $U_2= 1/2V\cos\Omega t$; $U_3=U_1+U_{dc}$, $U_4=U_2+U_{dc}$, where U_{dc} is the DC voltage.

In the axial direction the ions are confined by the DC field produced by the U_{dc}. The motion is much simpler than in the RF field. Around the trap center the DC potential is close to a quadratic shape and the ions move in harmonic motion.

As a result of Laplace's equation the DC field along the axial direction will inevitably defocus trapping in the radial direction. Therefore the balance between the DC and the RF voltages needs to be carefully tuned to effectively trap ions in all three dimensions. In the trap center along the radial direction the effect of the DC voltage applied on the end electrodes can be approximated as an effective DC voltage U_{eff} applied on all central electrodes [55]. U_{eff} is a voltage proportional to the applied DC voltage on the end-electrodes, and the constant of proportionality depends on the specific trap geometry. The ion motion equation (2.9) becomes:

$$\begin{aligned} \ddot{x} + \frac{e}{mr^2}(U_{eff} - V\cos\Omega t)x = 0 \\ \ddot{y} + \frac{e}{mr^2}(U_{eff} + V\cos\Omega t)y = 0 \end{aligned} \tag{2.39}$$

with a, q parameters similar to (2.10):

$$\begin{aligned} a = a_x = a_y = \frac{4eU_{eff}}{m\Omega^2 r_0^2} \\ q = q_x = -q_y = \frac{2eV}{m\Omega^2 r_0^2} \end{aligned} \tag{2.40}$$

This produces the same Mathieu equation as equation (2.11):

$$\frac{d^2u}{d\xi^2} + (a - 2q\cos 2\xi)u = 0 \tag{2.41}$$

However, the parameter a has the same sign in both the x and y directions, which is different from the normal operating condition in the RFQ trap. This difference changes the stability region, as shown in Figure 2.7, where the shaded area indicates stability. Apparently, U_{eff} or a needs to be negative to trap positively charged ions in the axial direction.

The linear Paul trap can also generate a pseudo-potential DC well if RF voltage is applied to the end-electrodes instead of DC voltages [56]. One advantage of this operation mode is that it can trap both positive and negative ions simultaneously. In our system all the linear Paul traps use static DC potential in the axial direction. The big advantage here is significantly increased trapping efficiency of the injected ions, because the ions are not subject to a RF retarding and accelerating field. This capture efficiency is usually >90% for a linear ion trap compared with 5% for 3D RF confined traps [57]. Another advantage is larger trapping capacity because of trapping along a line versus at a point [58].

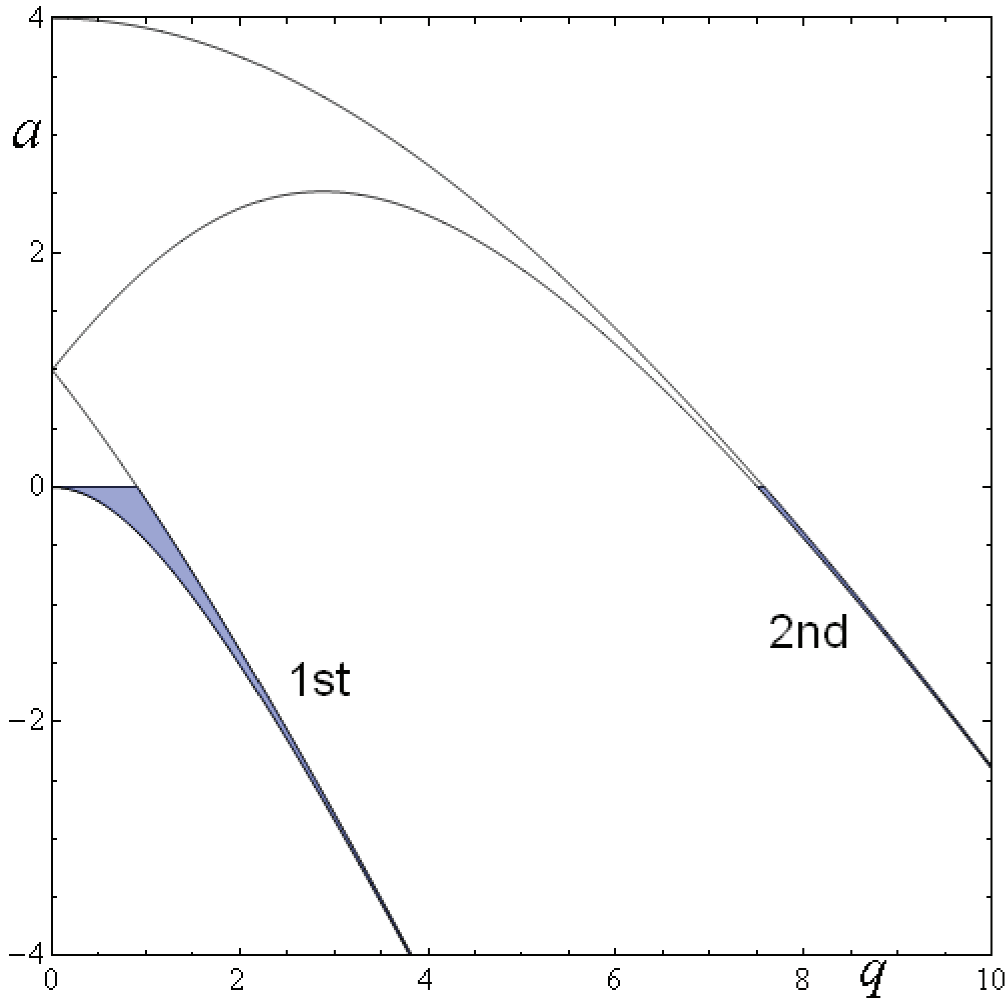

Figure 2.7: Stability diagram for a Linear Paul trap. The blue shaded areas show the stability regions. Only the first two stability regions are shown.

2.4 The Penning trap

A Penning trap confines ions with a superposition of a static electric field and a strong magnetic field. The ion confinement in the direction perpendicular to the magnetic field (radial direction) is from the magnetic force. In a pure magnetic field, the ion motion is called the cyclotron motion with frequency:

$$\omega_c = \frac{qB}{m} \tag{2.42}$$

where q is the charge, B is the magnetic field strength and m is the ion mass.

To get additional confinement along the direction of the magnetic field (axial direction), a static quadrupole electric field is applied by the end-cap electrodes and ring electrode as shown in Figure 2.8. In an ideal Penning trap as shown in Figure 2.8(a), the electrodes are hyperboloids of revolution with $r_0 = \sqrt{2}z_0$, in which r_0 is the radial distance between the trap center and the ring electrode and z_0 is the axial distance between the trap center and the end-cap electrodes.

If $\pm\Phi_0$ is applied on the end-cap and ring electrodes, the ion motion is affected by both of the electric and magnetic field:

$$\begin{bmatrix} \ddot{x} \\ \ddot{y} \\ \ddot{z} \end{bmatrix} = \frac{q\Phi_0}{2md^2}\begin{bmatrix} x \\ y \\ -2z \end{bmatrix} + \frac{qB}{m}\begin{bmatrix} \dot{y} \\ -\dot{x} \\ 0 \end{bmatrix} \tag{2.43}$$

where

$$d^2 = \frac{1}{2}\left(z_0^{\ 2} + \frac{r_0^{\ 2}}{2} \right) \tag{2.44}$$

In the axial direction, the solution is simple harmonic motion with a frequency:

$$\omega_z = \sqrt{\frac{q\Phi_0}{md^2}} \tag{2.45}$$

In the radial direction, the solution is a superposition of two frequencies ω_+ and ω_-:

$$u(t) = R_+e^{-i\omega_+t} + R_-e^{-i\omega_-t} \tag{2.46}$$

in which u represents either x or y, R_+ and R_- are constants, ω_+ and ω_- are called reduced cyclotron frequency and magnetron frequency respectively, and their values are:

$$\omega_\pm = \frac{\omega_c \pm \sqrt{\omega_c^{\ 2} - 2\omega_z^{\ 2}}}{2} \tag{2.47}$$

The ion motion in a penning trap is illustrated in Figure 2.9.

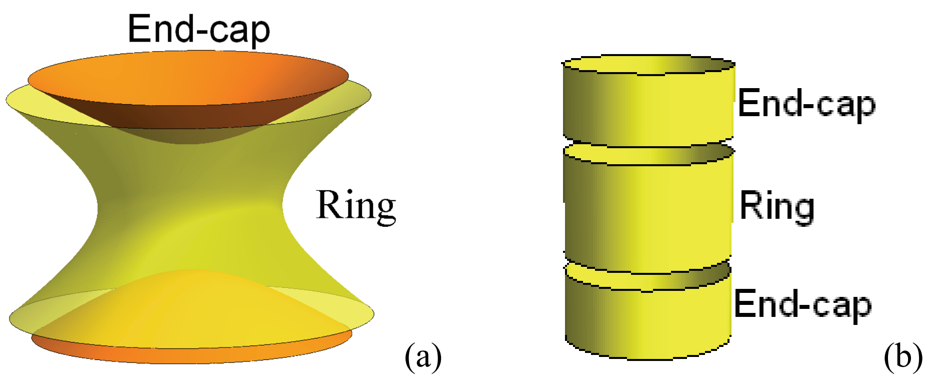

Figure 2.8: Penning trap structure. (a) Electrode surface of an ideal penning trap. (b) Simplified cylindrical Penning trap. This is the structure of the gas filled isobar separator used in our system which will be discussed in the next chapter.

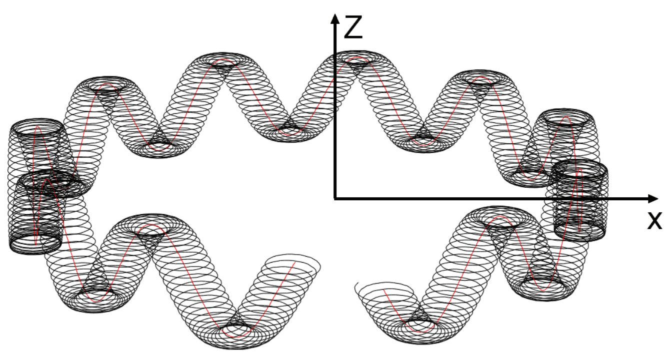

Figure 2.9: Ion motion in a Penning trap. The red trajectory is the magnetron motion and axial motion. The small black circle is the reduced cyclotron motion, with a frequency very close to that of cyclotron motion.

Chapter 3 Experimental setup

The β-ν angular correlation measurement utilizes cooled, pure samples of ions. With its 840 ms half-life, ^{8}Li has to be created by an accelerator-induced nuclear reaction, then purified and transferred to the measurement trap. The ion injection system for the Canadian Penning Trap (CPT) Mass Spectrometer(from the large bore magnet to the isobar separator in Figure 3.1) [59] at Argonne National Laboratory (ANL) is used to acquire and transport ^{8}Li ions to the Beta-decay Paul Trap (BPT) [60], where the ^{8}Li decay is measured. The system is shown in Figure 3.1.

3.1 Production

^{8}Li is produced through the $^{7}Li(d,p)^{8}Li$ stripping reaction. The ^{7}Li beam is produced by the Argonne Tandem Linac Accelerator System(ATLAS) [61,62], which is a superconducting low energy heavy-ion accelerator, providing beams ranging from protons to uranium with energy as high as 17 MeV per nucleon for lithium. $^{7}Li^{-}$ is produced in the negative-ion source system based on a commercial NEC SNICS II negative-ion source [62]. The DC $^{7}Li^{-}$ beam from the negative ion source is stripped by a thin (~ 2μg/cm^2) carbon foil to form the $^{7}Li^{3+}$ charge state. The ions are then accelerated by the superconducting linac to deliver a beam of 6 nA at 24 MeV. The layout of the ATLAS facility is shown in Figure 3.2.

The target is a D_2 gas target with thickness 4.5 cm maintained at 550 torr and cooled by circulating liquid nitrogen. The target windows are made of 1.3 mg/cm^2 thick titanium.

The total cross section is estimated from a Distorted-Wave Born Approximation calculation and previous experimental data [63]. The angular distribution of the cross section is inferred from an experiment at E_d=12 MeV(where E_d is the energy of deuterons beam) reported by J.P. Schiffer *et al.* [64]. The Coulomb scattering of the ^{7}Li beam could affect the collection of produced ^{8}Li. The Coulomb scattering cross section is estimated by the Rutherford scattering formula:

$$\sigma_c(\theta) = \left(\frac{1}{4\pi\varepsilon_0}\frac{Z_1 Z_2 e^2}{4E}\right)^2 \frac{1}{\sin^4\frac{\theta}{2}} \tag{3.1}$$

The comparison between the cross section of ^{7}Li(d,p)^{8}Li reaction and the Coulomb scattering is shown in Figure 3.3.

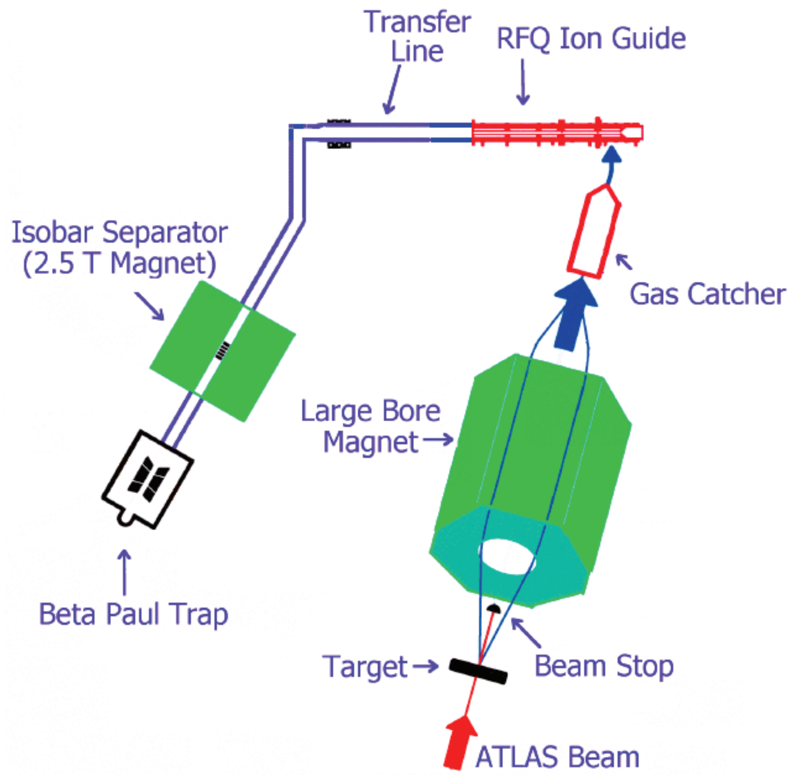

Figure 3.1: An overview of the CPT injection system and BPT apparatus. The beam is provided by the Argonne Tandem Linear Accelerator System (ATLAS).

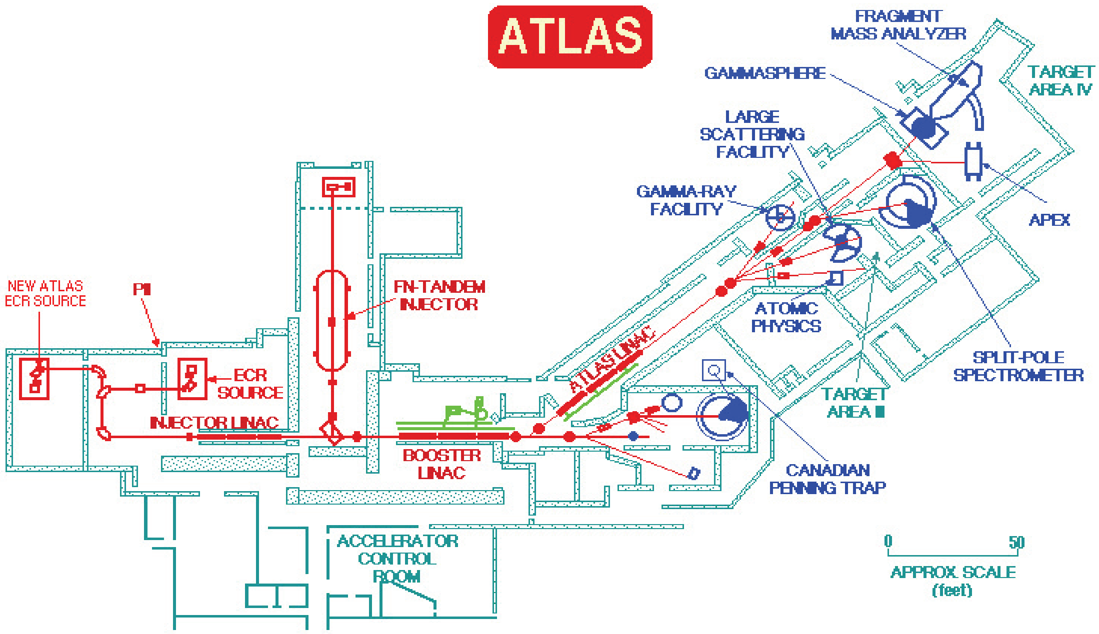

Figure 3.2: The ATLAS facility at ANL

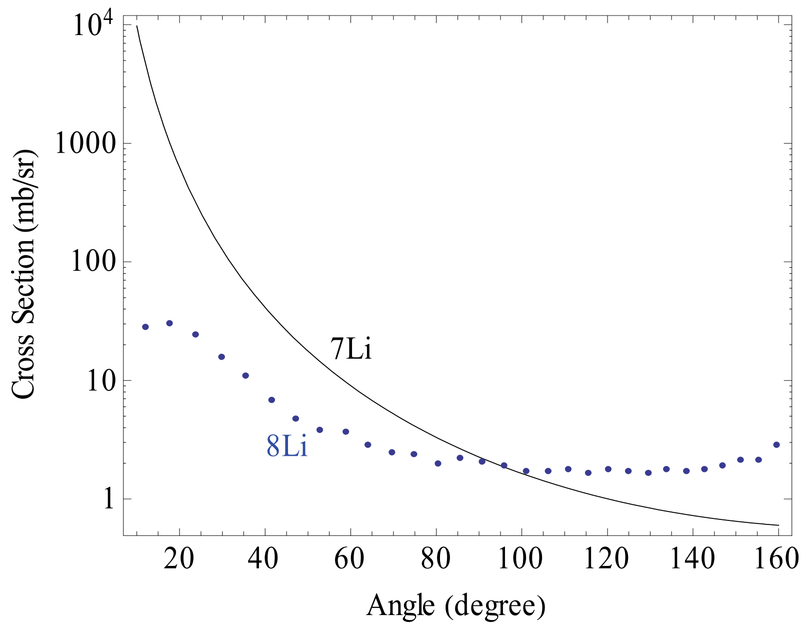

Figure 3.3: Cross section of ^{7}Li(d,p)^{8}Li reaction and the coulomb scattering of ^{7}Li in the center of mass frame. The blue dots are the measured data at E_d=12 MeV [64]. The data points are the total cross section including the ground state and the 0.98 MeV excited state of ^{8}Li. The black line is the Coulomb scattering cross section of ^{7}Li scattered on D_2, calculated from the Rutherford scattering formula, at the same center of mass energy as the data points.

Because of the scattering some of the primary ^{7}Li beam comes along with the produced ^{8}Li, seriously limiting the capacity of an important device, the gas catcher, as is discussed below. Because of this problem ^{8}Li are mainly collected at a large angle, where the Coulomb scattering is greatly reduced.

A beam stop made up of an aluminum cylinder 8 cm long and 3.8 cm diameter covered with a tantalum disk is located in the center of the beam line behind the gas target to block the primary beam. The beam stop is mounted on a movable track to be able to cover the angle from 0-3.2º to 0-7.0º. The beam stop position needs to be tuned to maximize the ^{8}Li collection while preventing too much ^{7}Li from entering the following system.

A 1 T superconducting solenoid magnet with a 0.6 m bore and about 2 m length is located behind the gas target, focusing the recoils into a gas catcher. It works as a standard solenoid magnetic lens. The focal length f depends on the charge state q, recoil axial momentum p_z, and magnetic field B [65]:

$$f = \left(\frac{2p_z}{q}\right)^2 \int B_z^{\,2} dz \tag{3.2}$$

From(3.2), if two ions have quite different rigidity (p/q), they could be well separated by the magnetic lens.

As Figure 3.4 shows, the low momentum branches of ^{8}Li and ^{7}Li angular distribution are much more separated than the high momentum branches, therefore they could be better separated by the magnet. The low momentum branch of ^{8}Li corresponds to angles larger than 50° in the center-of-mass (C.M.) frame. Combined with the fact that at large angles in the C.M. frame the Coulomb scattering cross section is relatively small (as in Figure 3.3), the ^{8}Li nucleus emitted backwards in the C.M. frame are selected even though the cross section is lower, while the ^{8}Li at small angles is blocked by the beam stop.

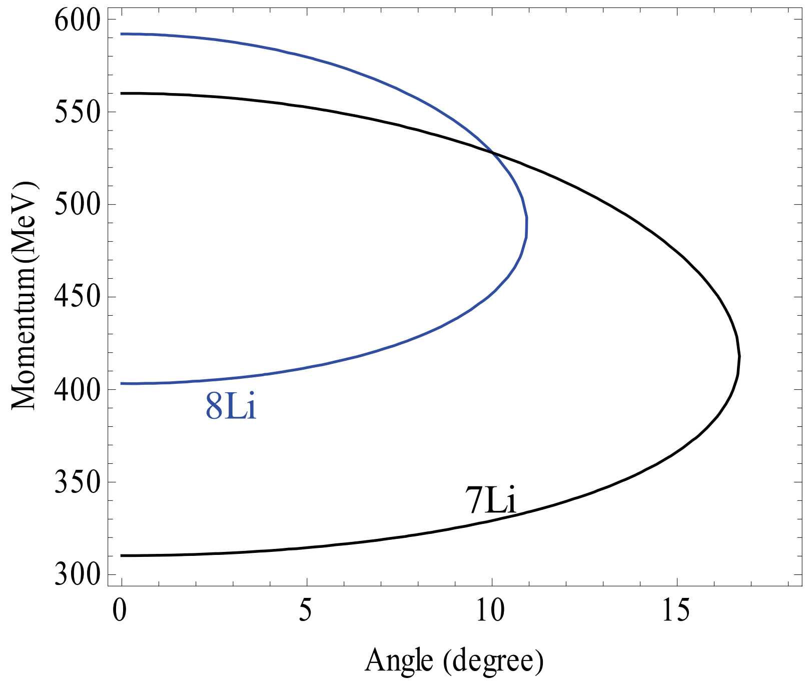

Figure 3.4: Momentum angular distribution of ^{8}Li and Coulomb scattered ^{7}Li in the Lab frame. The x-axis is the angle between the ions momenta direction and the beam direction. ^{7}Li beam has 24 MeV energy. The blue curve is the ^{8}Li angular distribution and the black curve is the ^{7}Li angular distribution. There are a low momentum branch and a high momentum branch for each distribution. The low momentum branch corresponds to backward momentum in the center-of-mass frame.

3.2 Transfer and separation

The gas catcher [66] (as shown in Figure 3.5) is a device designed to thermalize and extract the incident ions. It is a 25 cm diameter cylinder, 1.2 m long, filled with high purity helium gas at pressures ranging from 50-150 torr. A thin window at the front end of the gas catcher separates the helium buffer gas from the high vacuum in the beam-line. The window also works as a degrader, reducing the ^{8}Li energy so the ^{8}Li will be thermalized by the helium gas through collision and ionization. After thermalization, ions are extracted from the gas catcher by a combination of a static electric field and radiofrequency electric field. A DC voltage is applied along the electrodes of the gas catcher, forming the DC gradient to guide ions to the 1.3 mm diameter nozzle. The continuous helium gas flow also helps to extract the ions. The RF field is applied along the body and the cone of the gas catcher, preventing ions from hitting the wall.

Although the helium gas supplied is 99.995% pure and further purified by cold traps and a commercial purifier before flowing into the gas catcher, some water and other elements still exist in the catcher. Usually these contaminations are totally undesirable but for ^{8}Li, water is found to be useful or even essential to transfer ^{8}Li in our current system. As an alkali metal, lithium reacts intensely with water, forming lithium hydroxide ($2\ Li + 2\ H_2O \rightarrow 2\ LiOH + H_2$) and lithium hydroxide monohydrate ($LiOH \bullet H_2O$).

The gas catcher was originally designed to provide ions for mass measurements, mainly on heavy nuclei. The frequency of the applied RF voltage can repel heavy ions away from the inner wall, but is not high enough for ions as light as ^{8}Li. The frequency, which depends on the impedance of the whole system, cannot be changed easily. Instead, when small amounts of ^{8}Li ions are extracted through the nozzle, much more LiOH and $LiOH \bullet H_2O$ are also extracted. A new gas catcher cone that has been constructed will be installed in the future; this will work at higher frequency so that the ^{8}Li can be extracted effectively.

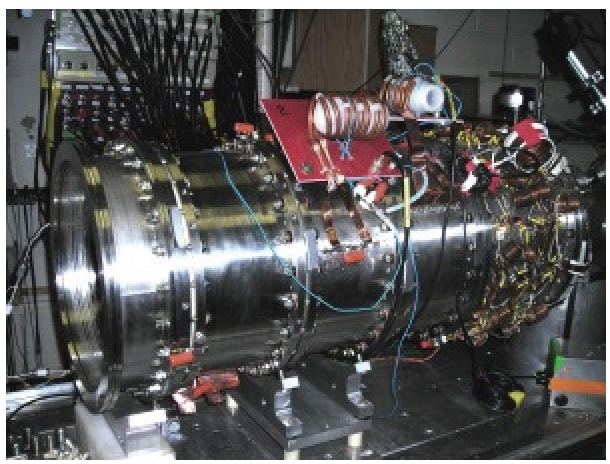

Figure 3.5: Gas catcher

3.3 RFQ ion guide

After the ions are extracted from the gas catcher, they enter the RFQ ion cooler section. Its purpose is to remove residual helium gas from the gas catcher, remove some contaminants, bunch the ions of interest, and prepare to send them to the isobar separator. The ion cooler is an RFQ ion guide described in section 2.2.

The whole ion guide section is comprised of 3 smaller sections separated into three chambers, with each chamber connected by small conical nozzles of 2-6 mm diameter.

The nozzles limit the gas flow so that the residual helium gas from the catcher can be removed by pumps connected to each section. The electrodes in all three sections are made of 0.75" diameter stainless steel rods, separated by 1.40" between each diagonal pair. Each electrode is segmented into 0.78" length rods separated by ceramic insulators and connected by resistors, providing a DC gradient along the beam transfer direction.

The second section has a 90° bend, collecting ions from the gas catcher and transferring them to section 3. Section 2 is operated in a mass selection mode by applying a static DC offset between the two pairs of the electrodes. Section 2 is the first one with mass selective ability after the gas catcher. In the ^{8}Li experiment, section 2 is set to allow LiOH•H_2O to pass through, while other ions are expelled. This helps to prevent saturation in the end of section 3, where the last three segments of the electrodes form a linear Paul trap, accumulating and cooling the ions. If too many ions are present, the space charge disturbs the trap field so the ions cannot be efficiently trapped. At the end of the RFQ cooler section, the continuous high energy ^{8}Li generated by ATLAS has been converted to bunched, cooled LiOH•H_2O clouds, which will be ejected toward the isobar separator at 10 Hz.

3.4 Isobar separators

The isobar separator is a gas filled cylindrical Penning trap [67] (as seen in Figure 3.6) surrounded by a 2.25 T superconducting solenoid. The function of the isobar separator is to break up LiOH•H_2O and LiOH into ^{8}Li and to remove all other possible contaminants.

The DC voltages are applied to the 9 electrodes, forming a harmonic potential along the axial direction. The central electrode is split into four segments to apply dipole and quadrupole excitation. The settings of the DC voltage and the pulses are listed in table 3.1. When the capture pulse is applied, the voltages on the front side electrodes are reduced to allow the ions to fly into the trap.

After the ions were captured in this isobar separator they were allowed to cool for ~ 6 ms. This RF quadrupole excitation at ω_c = 4309005 Hz was set for 25 ms. A good fraction of the LiOH and LiOH•H_2O ions break up during this process through the collisions with the buffer gas. The Li^+ ions are centered while other ions are removed.

After the ω_c excitation the ions are cooled for 2.5 ms before they are ejected from the trap. In principle the addition of ω_+ dipole excitation at the LiOH frequency could increase the energy of the collisions between LiOH and helium gas, which could help break up LiOH. This technique has been used in subsequent experiments but during this experiment, ω_+ excitation did not make an obvious difference.

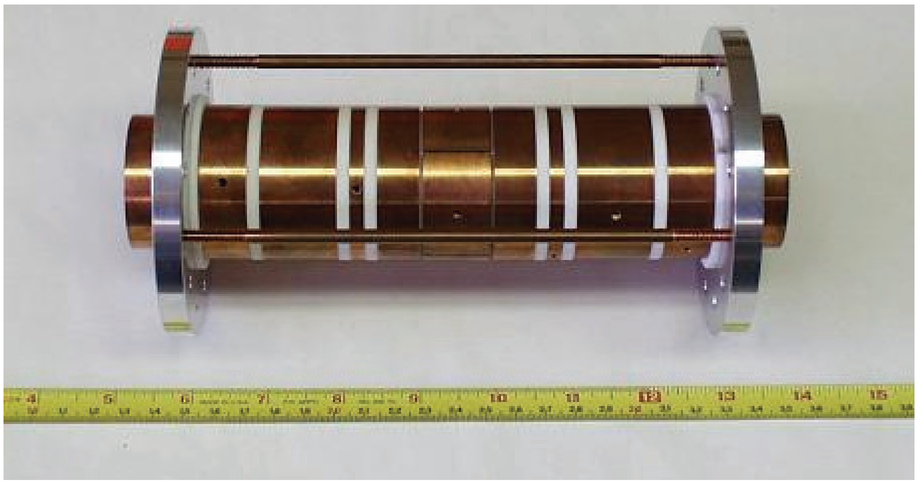

Figure 3.6: Isobar separator

Electrode	1&2	3	4	5	6	7	8&9
Capture Pulse (V)	-119	-25					
DC Voltages (V)	45	29	4	-4	4	29	45
Ejection Pulse (V)			60		-60	-60	-119

Table 3.1. DC voltages, capture and ejection pulse amplitudes used for the isobar separator in the present ^{8}Li experiment.

3.5 Beam transport

Ions are guided through the beam line by standard ion optics, such as Einzel Lenses, and quadrupole deflectors. The bending of the beam line is necessitated by the space limitation of the laboratory room; therefore a set of steerers are used to bend the ions trajectory. The potentials of the traps including the coolers, isobar separator and the BPT are kept around 0 V. An accelerating voltage of -1490 V is used to transfer the ions quickly between traps, and the ions are decelerated before entering these traps. During the transfer, steerers are used to guide the ions and lenses are used to keep the beam from dispersing. A schematic of the beam-line from the cooler section to the BPT is shown in Figure 3.7.

To optimize the steering and transmission of the beam, various diagnostic elements such as microchannel plate (MCP) detectors and silicon surface barrier detectors are included in the beam-line. Shown in Figure 3.7 are the diagnostic detectors that are located in the three crosses mounted on feedthroughs which allows either drift tube, MCP detector or silicon detector to be placed in the beam.

The MCP detector is sensitive to all ions and has very good timing resolution. When different ion masses are ejected from a trap, their velocities will vary, so they will arrive at the MCP detector at different times. The time of flight and the counting information on the MCP detectors help to determine the relative number of ions of different species and allows us to roughly tune the system for the ion of interest. The MCP detector cannot distinguish stable atoms from radioactive ions. At low counting rates the MCP detector cannot separate the ions from the background and a silicon detector is used to count the beta decay electrons. A 4.6 mg/cm^2 thick aluminium foil is located 1-2 mm in front of the Si detector to stop the incoming ions and prevent them from hitting the detector. Beta particles pass through the foil and are recorded by the silicon detector. In this way, only radioactive ions are detected.

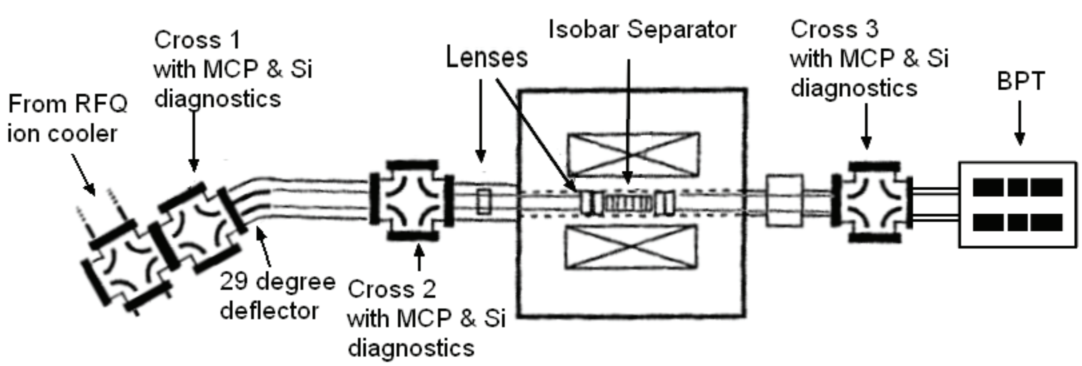

Figure 3.7: A schematic of the transfer line from the ion cooler section to BPT.

3.6 Beta-decay Paul Trap (BPT)

The BPT is the final trap where the ^{8}Li ions are trapped and where the measurement is made. This is a radiofrequency linear Paul trap consisting of four sets of segmented planar electrodes. The standard hyperbolic electrode structure is replaced by flat plates to enable the Si detectors to subtend a large solid angle. The structure of the trap is shown in Figure 3.8. I was involved in the design of the electrodes and the simulation of the electric field.

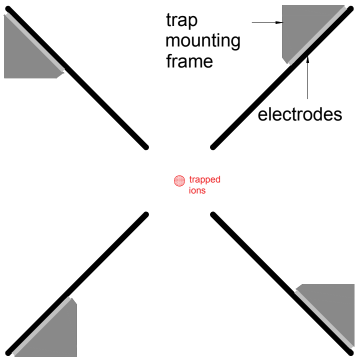

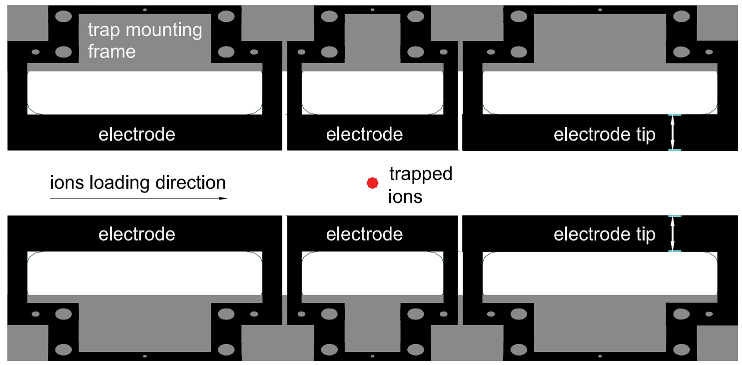

(a) (b)

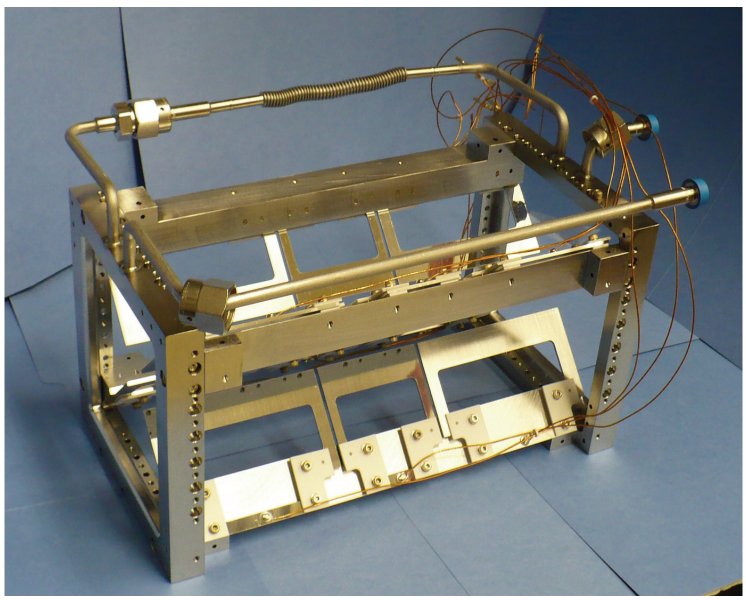

(c)

Figure 3.8: Structure of the Beta-decay Paul Trap. (a) A cross-sectional end view showing the trap electrodes, and trap mounting frame. The electrodes are made of 1.9 mm stainless steel plates. The distance from the trap center to the edge of the electrode is 17 mm. Ions are loaded along the axis of the trap, which is referred to as the axial direction while the other two directions are referred to as radial directions. The ions are confined by the RF in the radial directions. (b) A cross-section top view of the BPT. The electrodes are 45° relative to the figure plane. Ions are confined in the beam direction by DC potentials applied to the three segments of electrodes. The width (along the axial direction) of the end electrodes is 100.0 mm and that of the center electrodes are 62.0 mm. The hole in the electrode plates is to reduce the RF pickup by the silicon detectors, which will be discussed in section 3.10.1. (c) Picture of the BPT.

3.6.1 Ion confinement

The BPT is operated as a conventional quadrupole linear ion trap as described in section 2.3. A DC voltage is applied to the three segments to form a static DC potential well along the beam direction, confining the ions axially. RF voltages with opposite phases are applied on the two pairs of electrodes to confine the ions radially. As discussed in section 2.2.1, an infinite hyperbolic electrode will give a potential in the form of $\Phi = \lambda(x^2 - y^2)$ which is perfect for ion confinement. Although the theoretical electrodes are replaced by planar electrodes the potential very near the trap center will always be very close to the one provided by electrodes of hyperbolic shape, which is determined by the solution of Laplace's equation. However this field region needs to be large enough for efficient ion confinement.

The potential field is simulated by ANSYS Maxell software, which uses a finite element method. The potential field around the electrodes is shown in Figure 3.9.

Around the trap center the field is very close to quadrupole. To quantify the field, we take the sample values along the x axis in the range of [-2mm, 2mm] from Figure 3.9, and fit it to a quadratic function with the result

$$\Phi = 1.269x^2 \tag{3.3}$$

as shown in Figure 3.10.

By comparing the equation (3.3) and (2.7), to generate the same field with ideal hyperbolic electrodes operated at the same voltage of Φ=500 V, the distance R from the electrode inner surface to the trap center needs to be:

$$R = \sqrt{500/1.269}(mm) = 19.85(mm) = 1.17R_0 \tag{3.4}$$

where R_0 = 17.0 mm is the distance from the actual electrode. This means that when we calculate the trap properties, the only difference introduced by the non-standard electrode shape is to replace the actual distance R_0 with an effective distance R_{eff}.

$$R_{eff} = 1.17\ R_0. \tag{3.5}$$

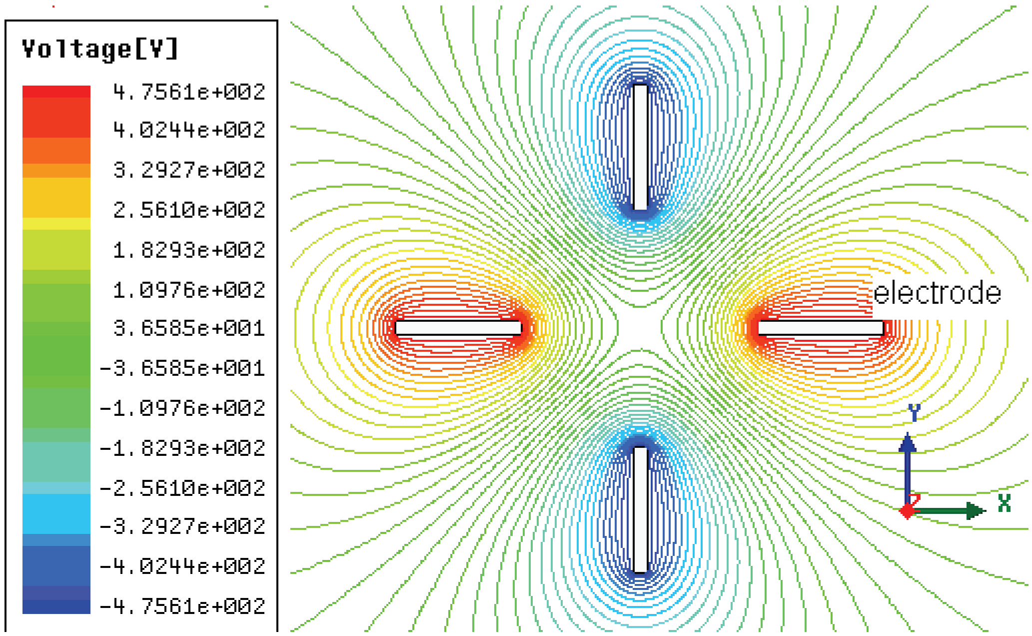

Figure 3.9: Simulated electric equipotential lines around the electrodes. The plotting is a cross sectional view at the trap center (refer to Figure 3.8). The two electrodes in the y direction are at -500 V, and the other two electrodes are at +500 V. The inner edge of each electrode is 17 mm from the trap center and the electrodes are 18 mm wide.

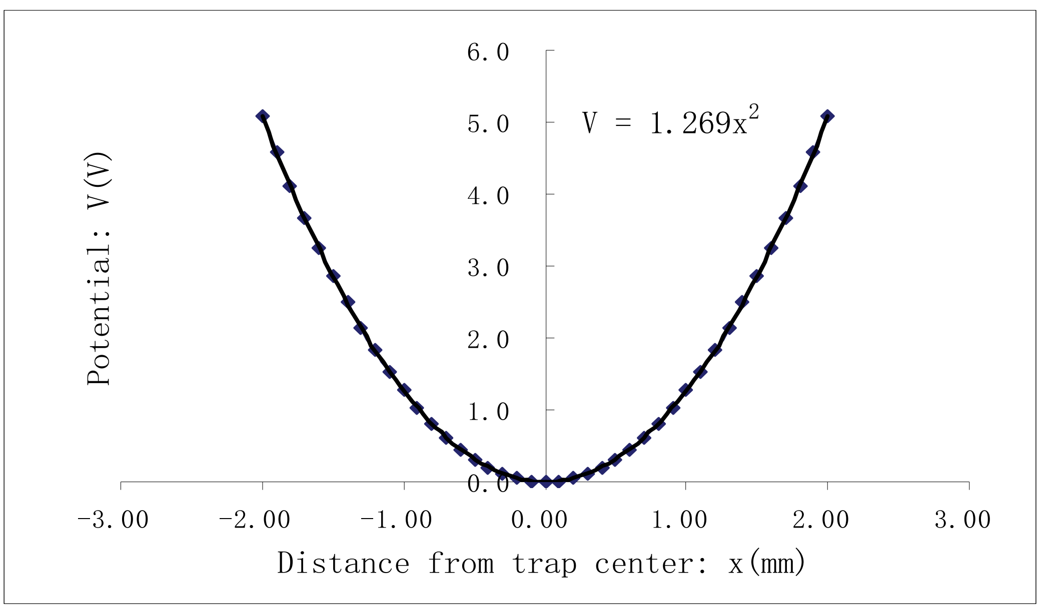

Figure 3.10: Plot of the potential along the x axis from Figure 3.9. Data points are taken every 0.1 mm, from -2 mm to 2 mm. From the data analysis in section 5.1, the majority of ions are confined within a 1mm radius of the trap center. The sample data points are well fitted by a quadratic function.

The effective distance R_{eff} is deduced from one dimension along the electrode. Proper trapping requires a two dimensional quadrupole potential. Further comparison confirms that in the radial plane within 4mm of the trap center, which is large enough for ion trapping, the maximum deviation from the ideal trap is less than 1%. Figure 3.11 indicates that in the region as large as 10 mm from the trap center the deviation is significant, while near the trap center the deviation is very slight.

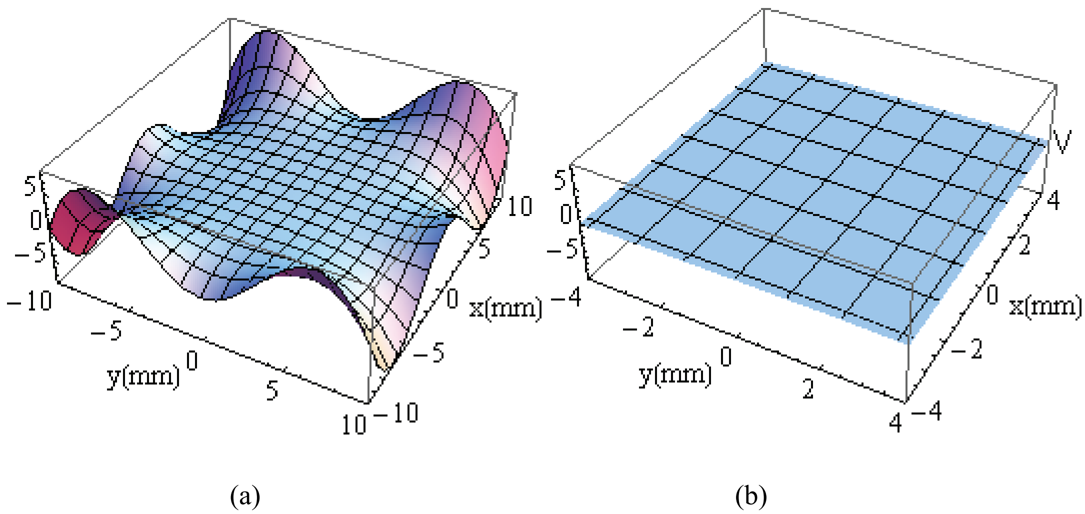

Figure 3.11: The deviation between the simulated potential with actual electrodes and the theoretical potential with ideal electrodes, both operated at ±500 V (a) Over ±10 mm from trap center. (b) Zoomed view over ±4 mm from trap center.

Along the axial direction a DC voltage is applied on the three segments. The typical values used for trapping ^{8}Li is -50 V on the center electrodes and +60 V on the end electrodes. The simulation of the DC field in the plane of two opposite electrodes is shown in Figure 3.12. Along the axial direction around the trap center the potential is shown in Figure 3.13. The simulation shows that along the axial direction near the trap center, the DC potential is well approximated by a quadratic function

$$V = 0.033z^2 - 42.4 \tag{3.6}$$

as shown in Figure 3.13, where V is the potential in volts and z is in mm.

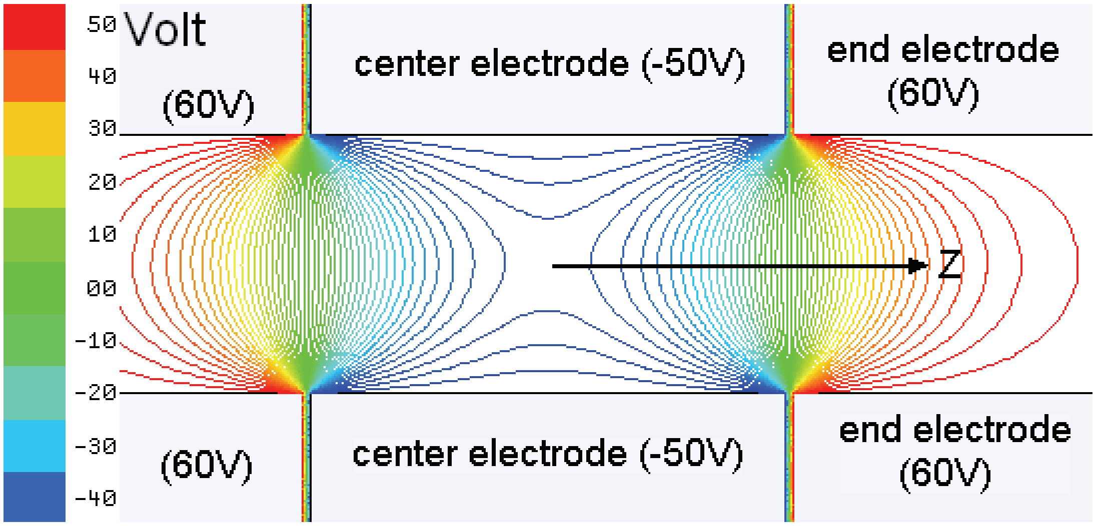

Figure 3.12: Simulation of the DC field between the three segments of electrodes in experimental conditions. The distance between the top and bottom electrodes is 34 mm and the width of the central electrodes is 62 mm.

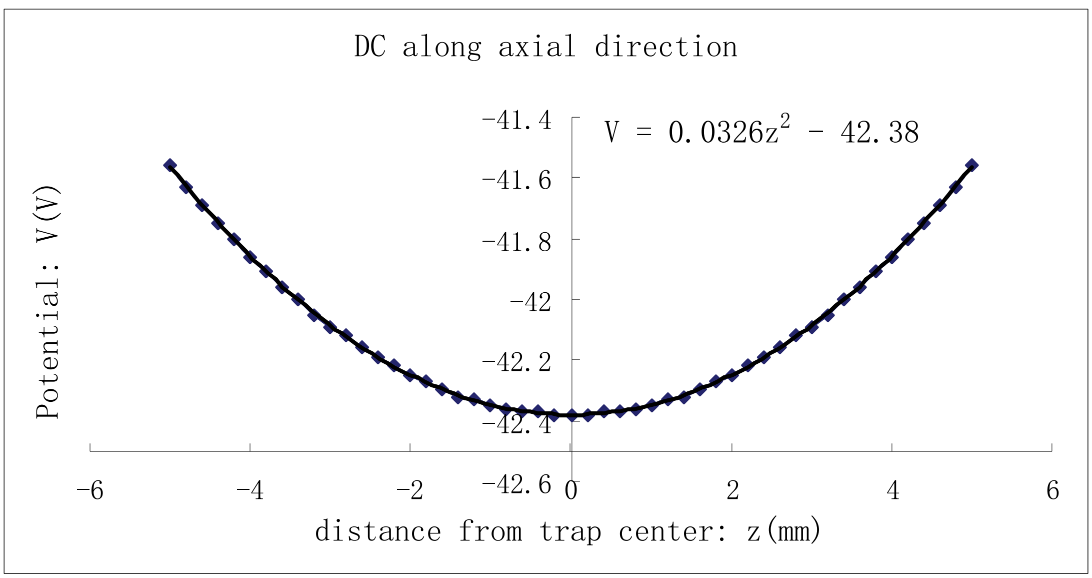

Figure 3.13: Simulation of the DC potential along the axial direction around the trap center.

3.6.2 Ion capture and ejection

A short capture pulse is applied to the front end segments to accept the ions ejected from the isobar separator. An eject pulse is periodically applied on the end electrodes to empty the trap for background measurements. The capture pulse is carefully tuned to open the trap right before ions arrive and close the trap immediately after the ions enter. Opening the trap too soon will unnecessarily disturb the trapping field, while opening the trap too late will block the incoming ions. Closing the trap too soon will not allow all of the ions to enter the trap, and closing the trap too late will allow captured ions to bounce back.

3.6.3 Storage time

High precision measurements require high statistics and low background. In order to get good statistics the ions need to be trapped for a time that is at least comparable to the decay half-life. The decay from ions that are not trapped can contribute backgrounds that could be very difficult to distinguish from signals, but that was not a problem in the present experiment because the two alpha particles are emitted back-to-back within a few degrees and therefore only decays that took place near to the center of the trap were registered. The storage time is strongly dependent on the vacuum so all the materials in the trap have to be compatible with ultra-high vacuum. The vacuum chamber is evacuated by two turbopumps backed by a lubricant-free scroll pump. The helium gas is purified by a liquid nitrogen cold trap before injection into the trap. Before an experiment, the system is usually pumped down for two weeks and baked at around 50℃ for several days to drive off moisture. The trap storage lifetime can be measured by the decay rate of trapped radioactive ions. The measured decay rate is a combination of the radioactive half-life and trap half-life. The trap lifetime is determined to be longer than 10 sec from the ^{8}Li decay rate. This will be discussed in detail in the data analysis section.

3.7 Detector system

The BPT trap is surrounded by four sets of silicon detectors. In each set, there is a Double-sided Silicon Strip Detector (DSSD) that is backed by one or two single-element silicon detectors (SD). The DSSDs are used to detect the alpha particle energy and direction and the single silicon wafer is used to detect the electron direction. In a ^{8}Li decay the two alpha particles are emitted almost back-to-back and therefore alphas from decays at or near the center of the trap hit two opposite DSSDs. Knowing the two alpha's momenta and the β direction, the whole ^{8}Li decay kinematics is complete. I was responsible for the setup of the detector system, electronics system, performed the detector calibration and constructed the data acquisition software.

The DSSDs were made by Micron Semiconductor [68] as Model W(2M)-300μm. They consist of 16 strips on the junction (front) side and 16 strips on the ohmic (back) side each of width 3.0 mm. Adjacent strips are separated by a 100 μm gap. The detectors have a 50×50 mm^2 active area and 300 μm thickness. The junction side has 0.7-1.0 μm thick aluminium windows as specified, usually known as dead layers. The typical full depletion voltage is 30 V. In order to maintain high vacuum in the trap, the silicon mounting board is made of ceramic instead of standard printed circuit board. The single element silicon detectors are also made by Micro Semiconductor and are 1.00 mm thick, have 50×50 mm^2 active area, and are also mounted on ceramic board. A set of the silicon detectors mounted on a plate is shown in Figure 3.14.

Each DSSD is mounted 52 mm from the trap center and the SD is about 3 mm behind the DSSD. To shield detectors from electrical pick-up from the nearby RF electric fields used to trap ions, each detector set is surrounded by two layers of independently-grounded aluminum casing. Both layers of shielding have an open window to allow particles emitted from trap center to reach the detector active area without any energy loss. To further shield the RF interface, the window on the shielding layer closer to the detector is covered with a >95% transmission nickel mesh (wire diameter 32 μm, 20 wires per inch). The geometry of the trap electrodes, detector array, and shielding is shown in the Figure 3.15.

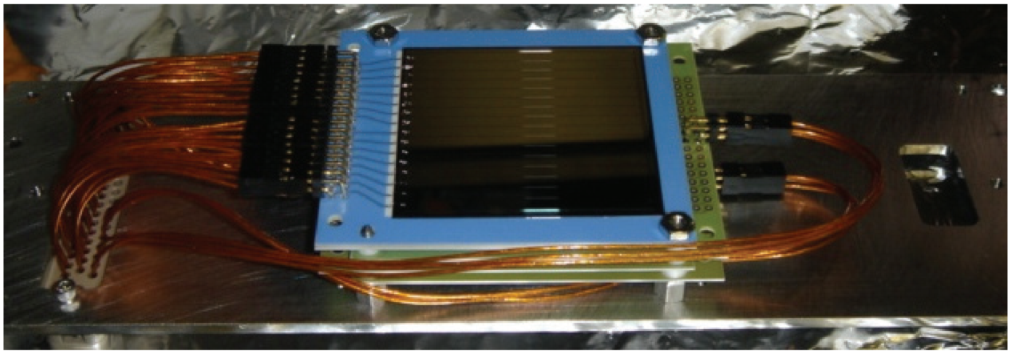

Figure 3.14: One set of silicon detectors mounted on a stainless steel plate. The top blue detector is a DSSD. The 34 pin header on the DSSD is connected to the polyetheretherketone thermoplastic connector mounted on the stainless steel plate via UHV-compatible cables.

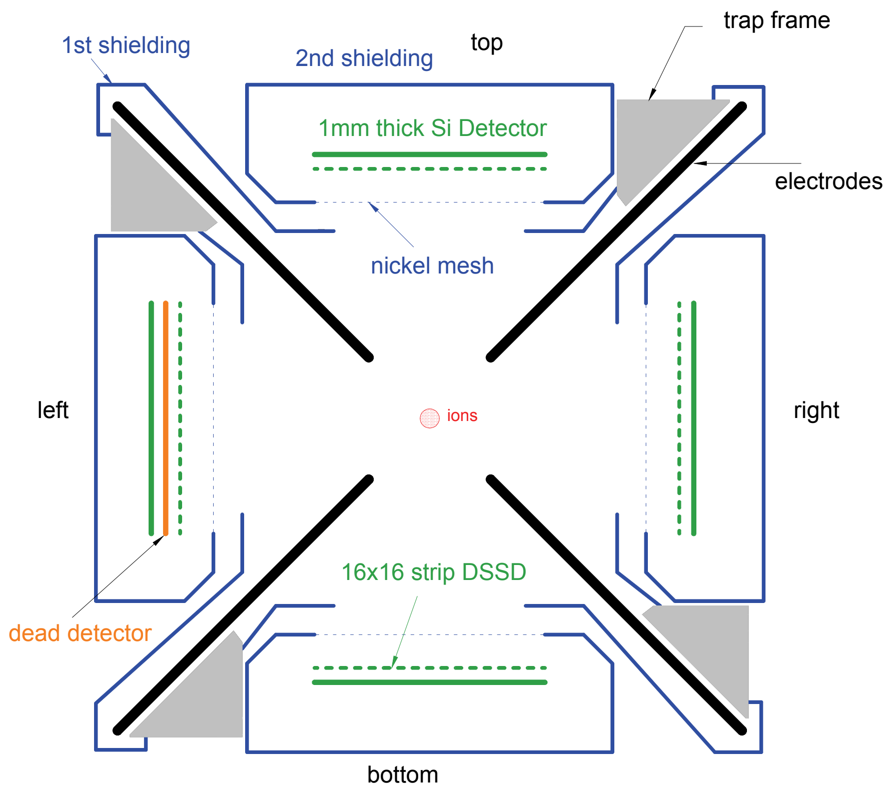

Figure 3.15: A cross section view of the trap and the detector system.

3.8 Signal processing

The total of 136 signals from all silicon detectors, including 128 signals from the strips of the DSSD and 8 signals from SDs, are initially processed through RAL 108 preamps that have a sensitivity of 44 mV/MeV and are manufactured by the Rutherford Appleton Laboratory [69]. The amplified signals are sent to shaping amplifiers originally designed and built at Argonne for the ATLAS Positron Experiment (APEX) [70]. The shaper is an octal unit which has unipolar outputs and a fixed shaping time of approximately 2.5 μs. Each shaper has a common leading edge discriminator to give one timing output and this logic output is used to trigger the data acquisition. In order to suppress the RF interference a low pass filter is built into the shaper. The output signal from the shaper is sent to a Philips 7164H PEAK ADC through twisted pair cables. The data are recorded through a CAMAC crate with the SCARLET driver package [71] developed by Kenneth Teh of the ANL Physics Division.

3.9 Data acquisition

If any channel of the DSSD records a signal, that signal triggers the data acquisition, opens the gate on all the ADCs for 5 μs, and all signals from every channel will be recorded as long as they are larger than the threshold, which is typically set to 40 keV. The electron signal on the silicon wafer is not used as a trigger because the signal is much smaller than the alpha signals on the DSSD. The timing from each shaper is recorded by a TDC, which is started by the earliest signal from whichever shaper. The time interval between two opposite DSSDs helps to distinguish real events from background because for a real event the two alpha particles always reach the DSSDs within 5 ns of each other. The relative time between a ^{8}Li decay and the previous capture pulse is also recorded. This information helps to study the ion cooling process.

3.10 RF pick-up

Good energy resolution is needed for a precise measurement. To reduce the noise on the silicon detector, the grounding, shielding and power distribution have been carefully designed, and the resulting energy resolution of a typical detector is about 50 keV. The biggest technical challenge is the pick-up from the RF electric field produced by the electrodes carrying 850 V peak-to-peak which are only 1 cm away from the detector. A lot of effort has gone into minimizing the RF pick-up to the level that is below other major sources of noises and more investigations are still being performed. Suppressing the RF pick-up is one of my contributions of this thesis research. The methods used to minimize the RF pick-up are discussed in the following paragraphs:

3.10.1 Electrode design

Every electrode plate has a big hole cut out of it in order to minimize the capacitance between the electrodes and the detector shielding casing (refer to Figure 3.8(b) and 3.15). After the present experiment the electrode was further modified to only leave the tip (Figure 3.8(b)), which is mounted on ceramics, and the voltages are applied to the electrode tip by a wire. Reducing the surface area of the electrodes will reduce the RF emission, therefore reducing the pick-up, while the RF field used to trap the ions is not affected because the field in the trap center is mainly determined by the electrode tip as in Figure 3.8(b).

3.10.2 Cables arrangement

The RF cables with opposite voltage phases are twisted together as much as possible to cancel RF emission. The RF cables are located as far away as possible from the signal cables. The lengths of all cables inside of the vacuum chamber are minimized.

3.10.3 Shielding

As shown in Figure 3.15, each of the four detector sets is surrounded by two layers of independently-grounded aluminum casing. For perfect conductors, one layer of completely-surrounded grounding conductor will give very good shielding. Due to the finite impedance of the shielding material and in the grounding path, the RF field produced by the electrodes can induce RF voltage on the shielding casing. Adding another layer of shielding greatly reduces the RF penetration.

3.10.4 Filtering

For a typical 1.5 MeV alpha signal output from the preamplifier, the signal to RF noise ratio is usually less than 1. The RF pick-up is a sinusoidal wave with fixed frequency (2.137 MHz during the present experiment) which corresponds to a period that is short compared to the length of the pulse from the silicon detector. Adding a notch filter between the preamplifier and shaper as shown in Figure 3.16(a) with resonance frequency the same as that of the trapping RF has been proven to be an effective way to eliminate the RF interference. A low pass filter with one single capacitor shorted to ground is also very effective in reducing RF noise. The low pass filter will work for a large range of RF pick-up, while the notch filter can only work for a single frequency. During this experiment, only the low pass filter was built into the shaper.

3.10.5 Shaping time

When the shaping time of the shaper is comparable to the RF period, which is about 0.5 μs, the output signal is seriously affected by the RF pick up. If the shaping time is much longer, several RF cycles will be averaged so the RF effect is smaller. Figure 3.17 compares the resolution of simulated silicon detector signals equivalent to about 2 MeV, 4 MeV and 6 MeV generated by an ORTEC 419 Precision Pulse Generator, with 0.5 μs shaping time and 3 μs shaping time in an ORTEC 572 amplifier. Clearly the longer shaping time greatly improves the energy resolution. This has been confirmed with several models of commercial amplifiers. After this thesis experiment was completed long shaping times were selected when the electronics system was upgraded.

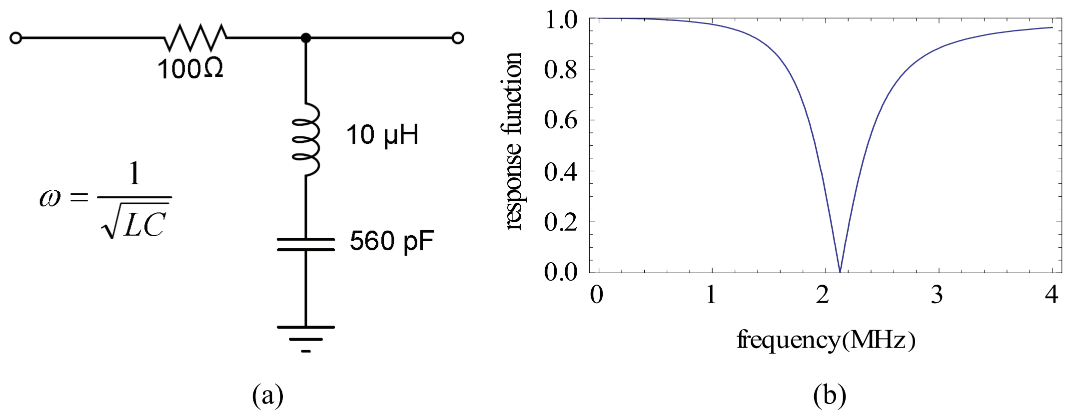

Figure 3.16: Notch filter to suppress RF pick-up. (a) Notch filter between preamplifier and shaping amplifier. (b) The response function of the notch filter.

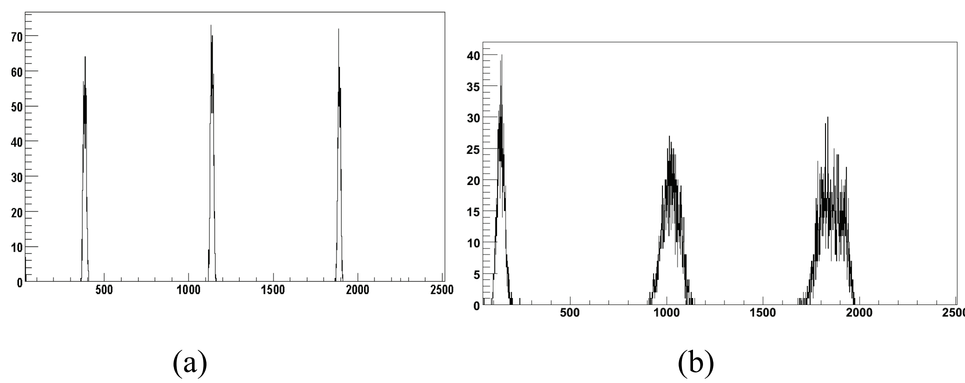

Figure 3.17: Pulse height spectra with standard pulser signals fed into the pre-amps. The RF pick up is typical of that during the experiment. (a) 3 μs shaping time (b) 0.5 μs shaping time.

3.11 Liquid nitrogen (LN_2) cooling

3.11.1 Advantages of using liquid nitrogen cooling

The BPT trap frame has an internal tube to circulate liquid nitrogen. The trap is normally operated with LN_2 cooling which has four benefits:

(1) Increasing the trap lifetime

The contaminants in the trap vacuum can charge exchange with the ions of interest, causing rapid ion loss. Before this experiment, there was no commercial purifier on the input He line. The 99.995% purity helium gas was only purified further by immersing a segment of the Helium transfer line into LN_2 cold trap. When the BPT is operated at room temperature, the trapping half-life was about 50 ms, which is short compared to the 840 ms half-life of ^{8}Li. However, with LN_2 cooling, most contaminants are frozen, which increases the trapping half-life to greater than 10 sec as seen during the experiment.

(2) Decreasing the ion cloud spread

Even with the long trapping lifetime that was achieved after the installation of the He purifier, we still operated the trap at LN_2 temperature to shrink the ion cloud size. After the ions reach thermal equilibrium with the helium buffer gas, the ion cloud size is determined by the ion kinetic energy E=3/2k•T and the trap potential depth, described by equation (2.32) and (3.6) for radial direction and axial direction, respectively. The trap temperature was monitored to be around 85 K with two thermocouples attached on the trap frame. Reducing the trap temperature from room temperature to 85 K reduces the ion cloud volume by a factor of 7.

(3) Protecting the detector from breaking down

At a high enough bias voltage, the depletion region extends over the entire volume of the silicon crystal. In this situation, the detector is said to be fully depleted. A silicon detector can be operated at even higher bias voltage to further increase the signal to noise ratio. However, a breakdown voltage exists above which the current increases dramatically due to an avalanche effect from impact ionization of electron-hole pairs. If not recovered quickly after break down, the detector can be permanently damaged. The breakdown voltage is temperature dependent. Detectors at colder temperatures can sustain a higher reverse-bias field. The current-voltage characteristics of diodes are summarized in Figure 3.18.

(4) Reducing the noise caused by leakage current of silicon detectors

In terms of a classical thermionic emission theory, the leakage current is strongly dependent on the temperature [72]:

$$I_{(T)} = T^2 \exp(-\frac{E}{2kT}) \tag{3.7}$$

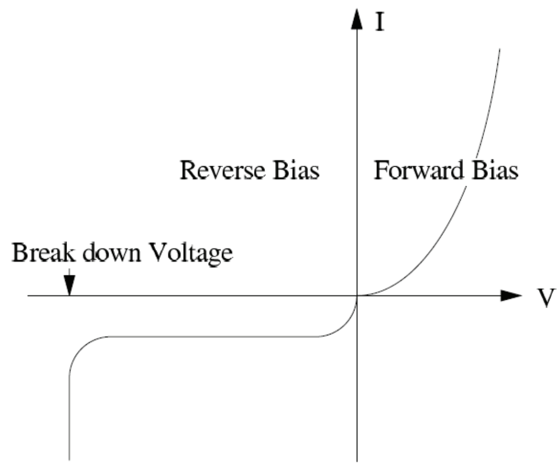

Figure 3.18: Characteristics of diodes

where I is the leakage current as a function of temperature T, k is the Boltzmann constant, and E = 1.2 eV is the ionization energy of silicon. Although this relation holds for a large temperature range, cooling the silicon detector from room temperature to -30 ℃ will visibly reduce the noise. Below -30 ℃ other noises will be dominant.

3.11.2 Concern of using liquid nitrogen cooling

The liquid nitrogen cooling causes mechanical stresses on silicon detectors. The thermal contraction coefficients of the silicon crystal, the detector ceramic board, and the detector mounting stainless steel board are all different. The detectors need to be carefully mounted in order not to be cracked by the LN_2 cooling.

3.11.3 Cryogenic pump design

The LN_2 is circulated by a centrifugal cryogenic pump designed specifically for this experiment. During this thesis research I identified and solved all critical technical challenges in the design of the cryogenic pump. The basic concept is to separate the pump housing from the motor by a long shaft so that the motor will not be frozen by the LN_2. Vibration becomes an important issue when two moving parts are connected by a long shaft. Two precision carbon-lubricated dry bearings are located on top and on bottom of the shaft and every component related to the alignment is machined with 0.1

mm precision. One difficulty of pumping liquid nitrogen is that the liquid nitrogen is operated at boiling temperature, which easily generates cavitations. Vapor bubbles form in the low pressure region directly behind the rotating impeller. This causes a great amount of noise, vibrations, and a loss of efficiency, even causing pumping failure. To prevent cavitations, an inducer (as shown in Figure 3.19c) was added below the impeller to increase the pressure inside the pump housing. The complete pump, the impeller and the inducer are shown in Figure 3.19.

After the present experiment the pump has been continuously operated for several months. The performance measured at various working conditions is shown in Figure 3.20.

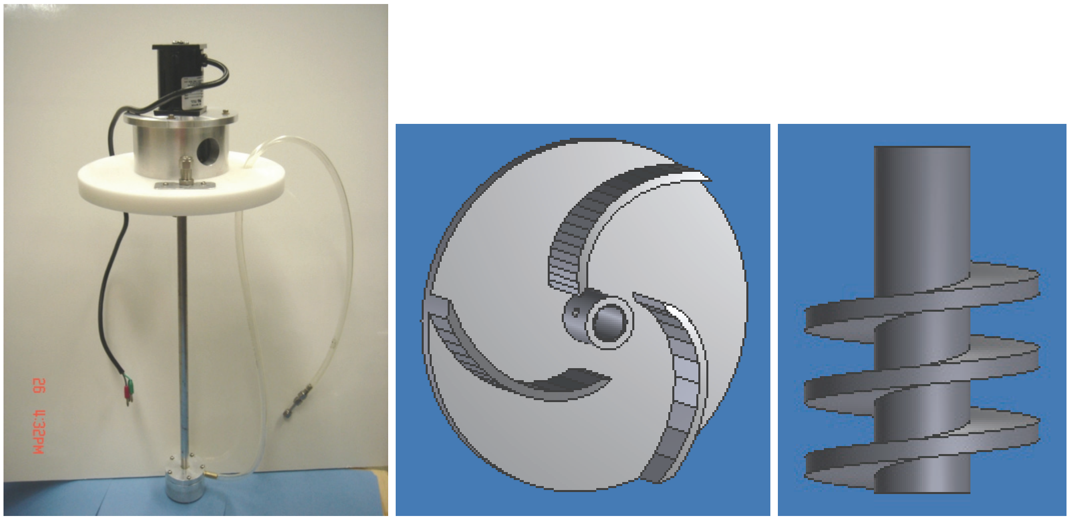

(a) (b) (c)

Figure 3.19: Centrifugal cryogenic pump (a) the complete pump (b)impeller (c) inducer

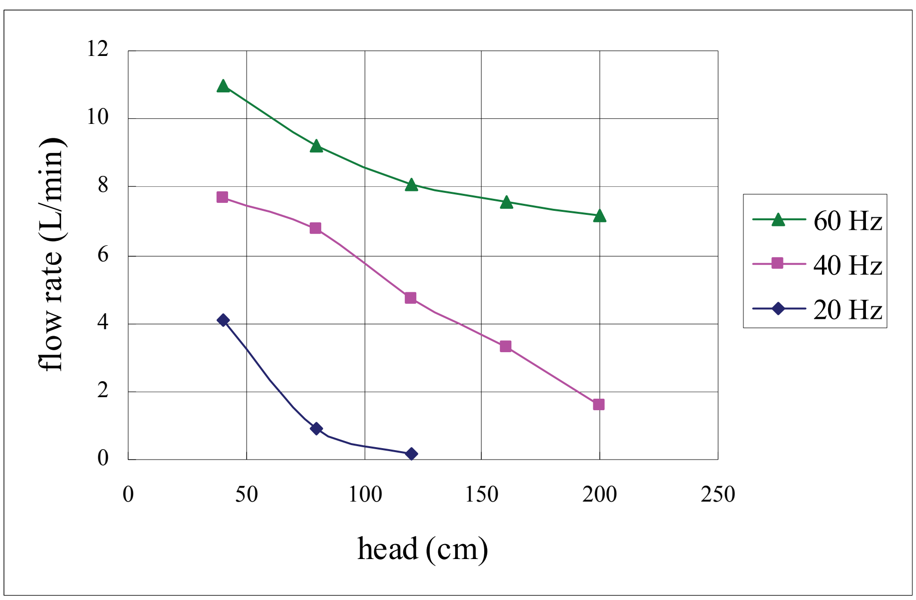

Figure 3.20: Liquid nitrogen flow rate chart tested with 3/8 diameter outlet tube, at shaft turning speed of 60 Hz, 40 Hz, and 20 Hz. The head on the x axis is the height of the outlet relative to the liquid nitrogen surface in the Dewar. During the experiment the pump is usually operated around 40 Hz, which is sufficient to keep the apparatus cool.

Chapter 4 Simulation of ^{8}Li decay and detector responses

The data analysis is based on the comparison of experimental data and Monte Carlo simulations. Sets of detailed simulations with pure axial vector coupling and pure tensor coupling are constructed. By comparing the experimental data with a linear combination of pure axial vector and tensor coupling simulations, we can observe a limit on the tensor admixture into the primary axial vector component. I was responsible for most of the simulation and the data analysis.

The propagation of generated particles and detector response are performed using the GEANT4 simulation package [73]. GEANT4 is a toolkit for simulating the passage of particles through matter. It helps us to investigate the β background and detector response to β particles.

Although it is totally feasible to do all the simulation with the GEANT4 toolkit, we actually separate the work into three stages:

(1) Decay generation: generate the ^{8}Li decay products: $^8Li \rightarrow \alpha + \alpha + e^- + \overline{\nu}_e$

(2) GEANT4 simulation of particle propagation and original detector response.

(3) Analyze the data from GEANT4, reconstruct the primary event.

The benefit of this is that we can separate the three stages and do not have to compile and run the whole simulation every time.

4.1 Decay generation

The algorithm of the decay generation is incorporated from the β-decay event generation code used in Refs. [30,74]. The code is adapted to include the ^{8}Li decay kinematics. The $J^\pi = 2^+$ ^{8}Li ground state decays to a broad 2^+ $^8Be^*$ state which immediately breaks up into two α particles, ($^8Li \rightarrow {}^8Be^* + e^- + \overline{\nu}_e \rightarrow \alpha + \alpha + e^- + \overline{\nu}_e$). Firstly, the weighted selection of ^{8}Be excitation energy is based on a cubic spline fitted to a precisely measured ^{8}Be final-state distribution [75], as shown in Figure 4.1.

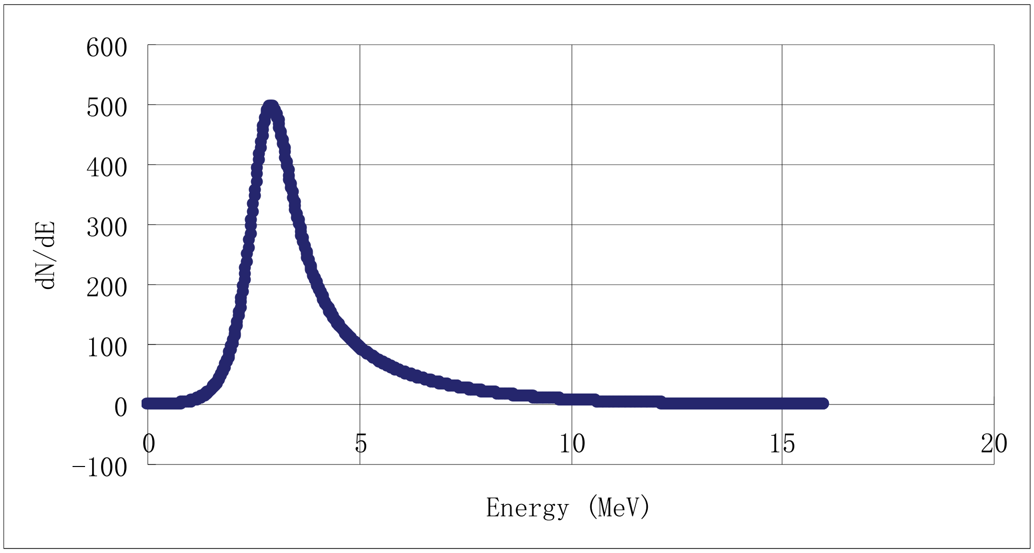

Figure 4.1: ^{8}Be 2^+ state continuum. Data points are from [75].

The next step is to randomly generate the complete decay based only on energy and momentum conservation. The weighting is considered afterward. The detailed procedure is as following: a random β energy in the allowed range by kinematics is generated, and random β and ν directions are generated. By the conservation of total energy and momentum, the neutrino energy can be calculated:

$$\begin{aligned} &M_{Li} = E_{Be} + E_e + E_v \\ &p_{Be} = \left|\vec{p}_e + \vec{p}_v\right| \qquad \Rightarrow E_v = \frac{(M_{Li} - E_e)^2 - (M_{Be} + E_{ex})^2 - p_e^{\,2}}{2(\frac{\vec{p}_e \cdot \vec{p}_v}{p_v} + M_{Li} - E_e)} \\ &E_{Be}^{\,2} = p_{Be}^{\,2} + (M_{Be} + E_{ex})^2 \end{aligned} \tag{4.1}$$

in which M_{Li}, M_{Be} denote $^8Li^+$, $^8Be^{2+}$ rest mass respectively, E_{ex} is the ^{8}Be excitation energy, and E_{Be}, E_e, E_v, p_{Be}, p_e, p_v denote the energy and momentum of ^{8}Be, β and ν_e, respectively.

Two α's directions are isotropically generated back to back in the rest frame of ^{8}Be, then the two α's momenta in lab frame are calculated according to the momentum conservation. Now a complete event has been generated. The weight to keep this event is based on Holstein's equation (53) in Ref. [34], that takes into account the α-β-$\overline{\nu}$ triple correlation and the recoil order terms of order E_e / M_{Li} :

$$
\begin{aligned}
& d\Gamma_{\pm} = F(Z,E_e)\frac{G_v^{\,2}\cos^2\theta_c}{2(2\pi)^6}(E_0-E_e)^2 p_e E_e dE_e d\Omega_e d\Omega_v \times \\
& \left[1-\frac{2}{3}\frac{M_{Li}-M_{Be}}{M_{Li}}(1+\sqrt{3}g_M)+\frac{2}{3}\frac{E_e}{M_{Li}}(5+2\sqrt{3}g_M)\right. \\
& \pm\left(-\frac{1}{3}+\frac{2}{3}\frac{M_{Li}-M_{Be}}{M_{Li}}(1+\sqrt{3}g_M)-\frac{4}{3}\frac{E_e}{M_{Li}}(1+\sqrt{3}g_M)\right)\frac{\vec{p}_e}{E_e}\cdot\frac{\vec{p}_v}{E_v} \\
& \pm\frac{E_e}{M_{Li}}\left(\frac{p_e^{\,2}}{E_e^{\,2}}(\cos^2\beta v-\frac{1}{3})\right)\pm\left(-\frac{1}{2}\frac{E_e}{M_{Li}}+(1+\sqrt{3}g_M)\right)\frac{p_e^{\,2}}{E_e^{\,2}}(\cos^2\beta v-\frac{1}{3}) \\
& \pm\left(-1+\frac{1}{2}\frac{M_{Li}-M_{Be}}{M_{Li}}(1+\sqrt{3}g_M)-\frac{E_e}{M_{Li}}(3+\sqrt{3}g_M)\right)\frac{p_e}{E_e}(\cos\alpha\beta\bullet\cos\alpha v-\frac{1}{3}\cos\beta v) \\
& \left.\pm\frac{p_e^{\,2}}{M_{Li}E_e}\cos\beta v(3\cos\alpha\beta\bullet\cos\alpha v-\cos\beta v)\pm\frac{-(M_{Li}-M_{Be}-E_e)}{2M_{Li}}(1+\sqrt{3}g_M)(\cos^2\alpha v-\frac{1}{3})\right]
\end{aligned}
$$

(4.2)

in which $d\Gamma_+$ represents the pure axial-vector coupling, while $d\Gamma_-$ represents the pure Tensor coupling. g_M is the weak magnetism term.

The decay location is generated with a 3D Gaussian distribution of (x,y,z) with the centroid at (0,0,0), where (0,0,0) is the center of our trap. The FWHM of the distribution is set to be (1.8mm, 1.8mm, 1.8mm), in which the value 1.8mm is obtained by comparing the simulation result with the experimental data, which will be discussed in detail in section 5.1. The Gaussian distribution is an approximation of the ion cloud and some other distributions are also considered in a systematic uncertainty analysis which will be described in detail in section 5.4.

4.2 Geant4 simulation

The GEANT4 simulation includes the geometry of the detectors and of the BPT trap, the ion cloud distribution, the energy resolution of the silicon detectors, and β scattering.
However, the simulation does not include: RF field, helium buffer gas, finite ion temperature, and the shielding mesh in front of the Si detector. The systematic effect of

these will not be visible in our current precision. (1)RF field: The peak-to-peak voltage of the RF is less than 1 kV, compared with the typical alpha energy of 1.5 MeV, so the correction for energy or direction will be less than 0.1%. (2)He buffer gas: the helium buffer pressure is kept at ~10^{-6} torr, and a 1.5 MeV alpha will deposit less than 1 eV energy in passing through the gas. (3)Ion temperature: systematic effects will be discussed in section 5.4. (4)Shielding mesh: the nickel mesh has 95% transmission. The wire thickness is 32 μm which will block all alpha particles hitting on the wire. The electroformed mesh has ultra precision and the transmission does not have any angular preference.

The geometries and positions of each detector correspond to the actual experimental set up. The detectors are made from pure silicon. The DSSD in the simulation is made as a single solid detector, while the strip number is read from the position where the particles hit. The GEANT4 set up of the whole BPT, presented in Figure 4.2, tries to reproduce the actual condition of the experiment. All other components, except for the detectors, are mainly built for the purpose of investigating the beta scattering effect. The electrodes, detector mounting plate, trap frame, trap end plates are made of stainless steel; the detector shielding is made of aluminium.

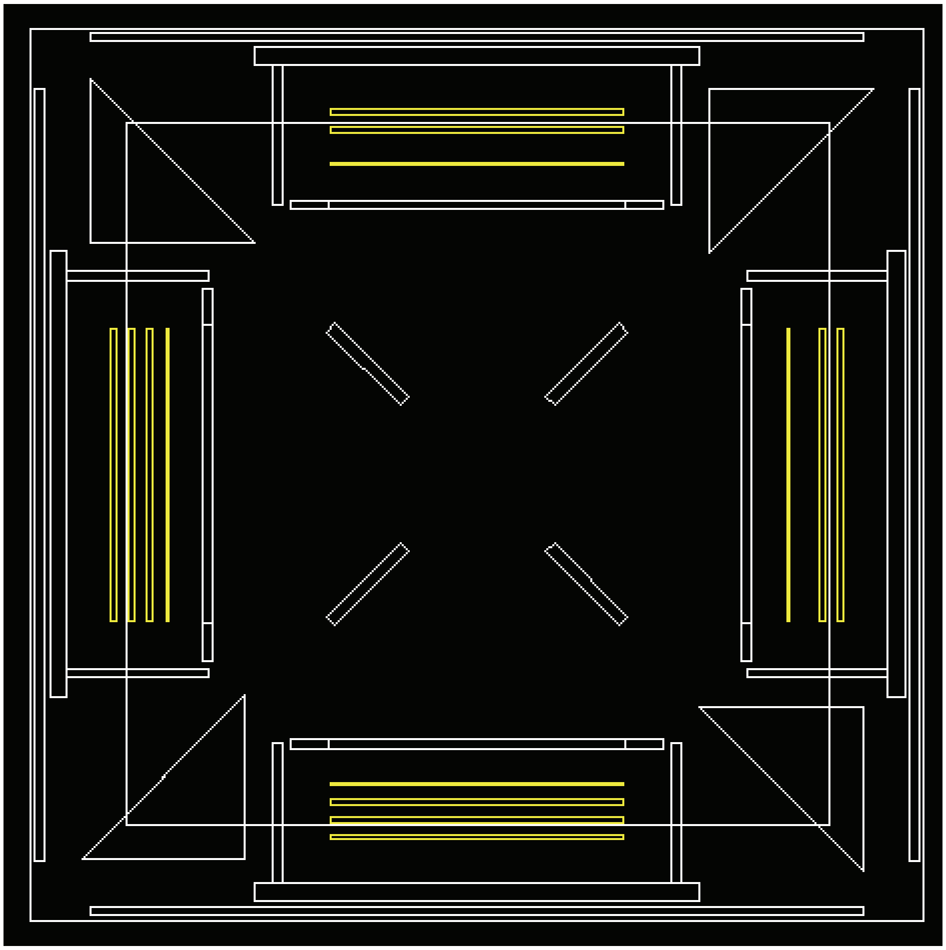

Figure 4.2: GEANT4 set up of BPT. The yellow plates are Si detectors. Each element in the drawing can be compared with the schematic drawing of the detector system in Figure 3.15.

4.3 Results of the simulations

4.3.1 Geant4 detector response

In the simulation the alpha particles in the ^{8}Li decay have about 1.5 MeV energy, and always deposit their full energy in the DSSD. The DSSD is constructed of pure silicon without a dead layer. The dead layer correction will be included when analyzing the experimental data. The end-point energy of the beta spectrum in ^{8}Li decay is about 13 MeV. Figure 4.3 shows the beta energy spectrum generated by the event generator in our program. Most of the betas will pass through the whole Si detector array, while in some cases, they will be scattered out or lose their full energy in one detector.

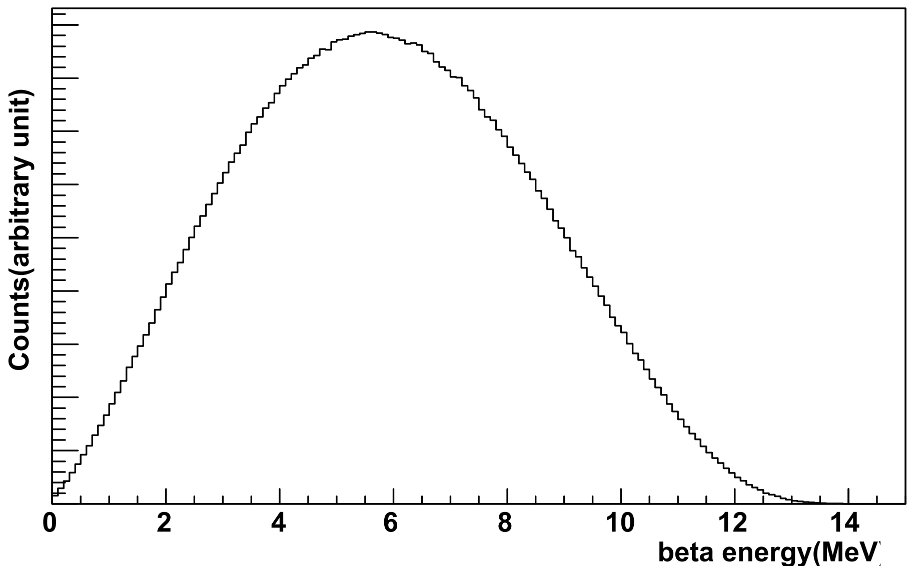

Figure 4.3: Beta spectrum generated in the simulation

Most of the electrons lose about 100 keV energy in the DSSD, which make them hard to separate from background, especially from the ohmic side of the DSSD, which typically has worse energy resolution than the junction side. In our experimental data, we are not able to extract a clean beta spectrum from the DSSD, while the beta signals show up clearly in the 1 mm silicon detectors. The simulated β energy deposits in silicon detectors are shown in Figure 4.4.

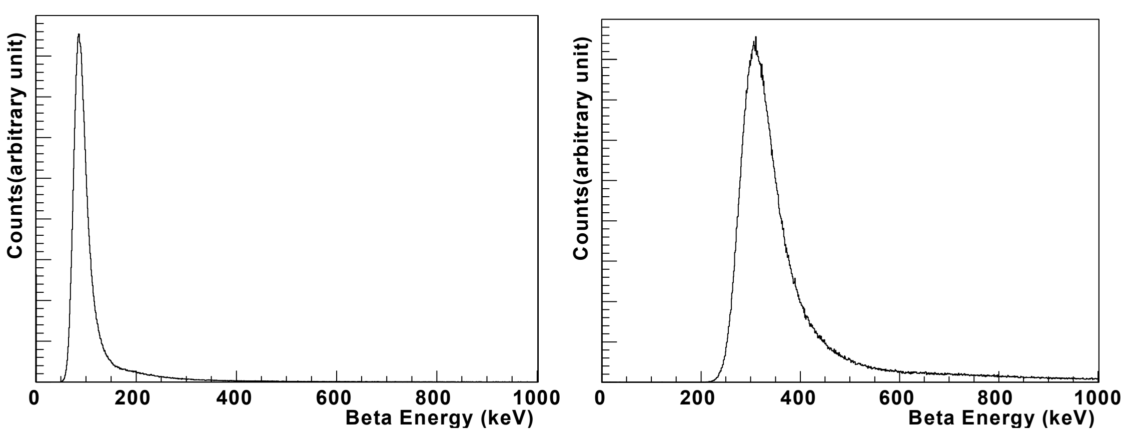

(a) β energy in DSSD (b) β energy in 1mm Si detector

Figure 4.4: Simulated β spectrum in the DSSD, and in the SD. All electrons are incident perpendicular with 6 MeV energy.

4.3.2 Reconstructing the events

In the final decay products of ^{8}Li ($^8Li^{3+} \rightarrow \alpha + \alpha + e^- + \bar{\nu}_e$), there are 12 degrees of freedom: three for each of the four outgoing particles. The constraints from energy and momentum conservation eliminate 4 degrees of freedom. In the experiment 8 quantities are measured: the 3-momentum of the 2 α particles, and the direction of the beta. Therefore the entire decay kinematics can be fully reconstructed.

The calculation of the beta momentum and neutrino's 3-momentum are from the two alpha's 3-momentum and beta direction follows:

alpha 1: p_{1x}, p_{1y}, p_{1z}; (knowing the three-momentum)

alpha 2: p_{2x}, p_{2y}, p_{2z}; (knowing the three-momentum)

beta: $r_x \bullet p_\beta$, $r_y \bullet p_\beta$, $r_z \bullet p_\beta$; (the absolute beta momentum p_β is unknown, the directions r_x, r_y and r_z are known, and $r_x^2 + r_y^2 + r_z^2 = 1$)

neutrino: p_{vx}, p_{vy}, p_{vz}; (three momentum is unknown)

In the decay: $^8Li^{3+} \rightarrow \alpha + \alpha + e^- + \bar{\nu}_e + 16.097$ MeV

$^8Li^{3+}$ mass: E = 7471.366 MeV

beta mass: m_e = 0.511 MeV

alpha 2^+ mass: m_α = 3727.37911 MeV

Momentum conservation:

$$p_{1x} + p_{2x} + r_x \cdot p_\beta + p_{vx} = 0;$$
$$p_{1y} + p_{2y} + r_y \cdot p_\beta + p_{vy} = 0; \tag{4.3}$$
$$p_{1z} + p_{2z} + r_z \cdot p_\beta + p_{vz} = 0;$$

Neutrino 3-momentum:

$$
\begin{aligned}
p_{vx} &= -(p_{1x} + p_{2x} + r_x \bullet p_\beta) \\
p_{vy} &= -(p_{1y} + p_{2y} + r_y \bullet p_\beta) \\
p_{vz} &= -(p_{1z} + p_{2z} + r_z \bullet p_\beta)
\end{aligned} \tag{4.4}
$$

Energy conservation:

$$
\begin{aligned}
E = &\sqrt{{p_{1x}}^2 + {p_{1y}}^2 + {p_{1z}}^2 + {m_\alpha}^2} + \sqrt{{p_{2x}}^2 + {p_{2y}}^2 + {p_{2z}}^2 + {m_\alpha}^2} \\
&+ \sqrt{{p_\beta}^2 + {m_e}^2} \\
&+ \sqrt{{p_{vx}}^2 + {p_{vy}}^2 + {p_{vz}}^2}
\end{aligned} \tag{4.5}
$$

Substitute (4.4) into (4.5), solve for p_β, and get:

$$
a \bullet {p_\beta}^2 + b \bullet {p_\beta}^2 + c = 0 \tag{4.6}
$$

$$
p_\beta = \frac{-b \pm \sqrt{b^2 - 4ac}}{2a} \tag{4.7}
$$

where a, b, c are defined as:

$$
\begin{aligned}
a = &4(E - \sqrt{{p_{1x}}^2 + {p_{1y}}^2 + {p_{1z}}^2 + {m_\alpha}^2} - \sqrt{{p_{2x}}^2 + {p_{2y}}^2 + {p_{2z}}^2 + {m_\alpha}^2})^2 \\
&+ 4[p_{1x} + p_{2x})r_x + (p_{1y} + p_{2y})r_y + (p_{1z} + p_{2z})r_z]^2
\end{aligned} \tag{4.8}
$$

$$
\begin{aligned}
b = &4[(E - \sqrt{{p_{1x}}^2 + {p_{1y}}^2 + {p_{1z}}^2 + {m_\alpha}^2} - \sqrt{{p_{2x}}^2 + {p_{2y}}^2 + {p_{2z}}^2 + {m_\alpha}^2})^2 \\
&- (p_{1x} + p_{2x})^2 - (p_{1y} + p_{2y})^2 - (p_{1z} + p_{2z})^2 + {m_e}^2] \\
&\bullet [(p_{1x} + p_{2x})r_x + (p_{1y} + p_{2y})r_y + (p_{1z} + p_{2z})r_z]
\end{aligned} \tag{4.9}
$$

$$
\begin{aligned}
c = &4(E - \sqrt{{p_{1x}}^2 + {p_{1y}}^2 + {p_{1z}}^2 + {m_\alpha}^2} - \sqrt{{p_{2x}}^2 + {p_{2y}}^2 + {p_{2z}}^2 + {m_\alpha}^2})^2 {m_e}^2 \\
&- [(E - \sqrt{{p_{1x}}^2 + {p_{1y}}^2 + {p_{1z}}^2 + {m_\alpha}^2} - \sqrt{{p_{2x}}^2 + {p_{2y}}^2 + {p_{2z}}^2 + {m_\alpha}^2})^2 \\
&- (p_{1x} + p_{2x})^2 - (p_{1y} + p_{2y})^2 - (p_{1z} + p_{2z})^2 + {m_e}^2]^2
\end{aligned} \tag{4.10}
$$

After p_β is solved the neutrino 3-momentum can be obtained directly from equation (4.4).

Energy conservation (4.5) leads to a quadratic equation (4.6), which has two roots. To determine which solution of (4.7) represents the real beta momentum, or whether the two roots are both legitimate, the coefficients a, b and c can be simplified as following:

Let E_{ev} denote the total energy of beta and neutrino,

$$E_{e\nu} = E - \sqrt{p_{1x}{}^2 + p_{1y}{}^2 + p_{1z}{}^2 + m_\alpha{}^2} - \sqrt{p_{2x}{}^2 + p_{2y}{}^2 + p_{2z}{}^2 + m_\alpha{}^2} \quad (4.11)$$

Let p denote the total momentum of the beta and the neutrino, and $\theta_{e\nu}$ denote the angle between the beta and the neutrino, then

$$p\cos\theta_{e\nu} = -(p_{1x} + p_{2x})r_x - (p_{1y} + p_{2y})r_y - (p_{1z} + p_{2z})r_z \quad (4.12)$$

$$(p_{1x} + p_{2x})^2 + (p_{1y} + p_{2y})^2 + (p_{1z} + p_{2z})^2 = p^2 \quad (4.13)$$

Therefore (4.7) is simplified to

$$p_{\beta\pm} = \frac{(E_{e\nu}{}^2 + m_e{}^2 - p^2)p\cos\theta_{e\nu} \pm \sqrt{E_{e\nu}{}^2(E_{e\nu}{}^2 + m_e{}^2 - p^2)^2 - 4E_{e\nu}{}^2 m_e{}^2 + 4p^2\cos^2\theta_{e\nu}E_{e\nu}{}^2 m_e{}^2}}{2(E_{e\nu}{}^2 - p^2\cos^2\theta_{e\nu})}$$

(4.14)

To study the two roots, we plot the two roots with variable p and $\cos\theta_{e\nu}$. We select $E_{e\nu}$ to be 13.5 MeV, which is a typical value in the beta neutrino energy sum spectrum generated by the event generator in Geant4, as presented in Figure 4.5. In most cases, p_β^+ is above zero, and p_β^- is below zero (as seen in Figure 4.6). In the experiment, since we already know the beta direction, the real solution has to be positive, i.e. p_β^+ is the real solution. But sometimes, as shown in Figure 4.6(b), both roots could be positive.

To know which root is the real solution when both roots are positive, we plot the β momentum spectra in Figure 4.7. The $p_{\beta-}$ distribution dominates at the very low momentum side, which has very few beta events as shown in Figure 4.7(b). So most probably $p_{\beta+}$ represents the real solution. But there is still about 0.15% chance that $p_{\beta-}$ represents the real solution as shown is Figure 4.7(c). Without detecting the β energy with the current detector system, $p_{\beta+}$ is assumed to be the correct solution. When calculating the neutrino momentum from equation(4.4), using the wrong β momentum will give a false neutrino direction, and therefore it will slightly distort the extracted β-ν angular distribution.

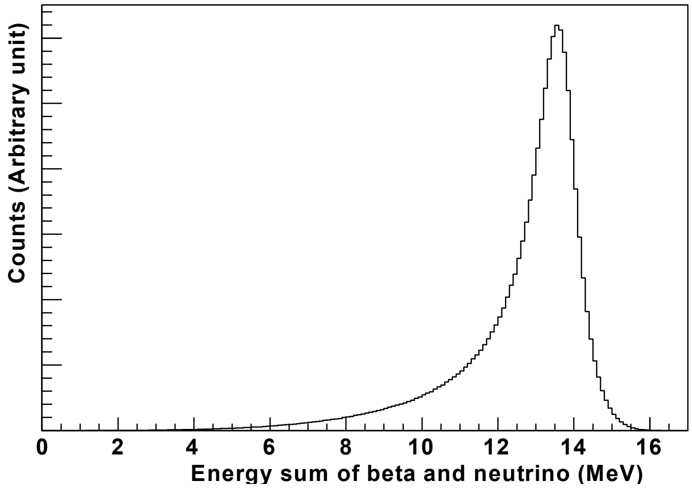

Figure 4.5: Energy sum of beta and neutrino in ^{8}Li decay. The broad peak is due to the broad states of ^{8}Be*.

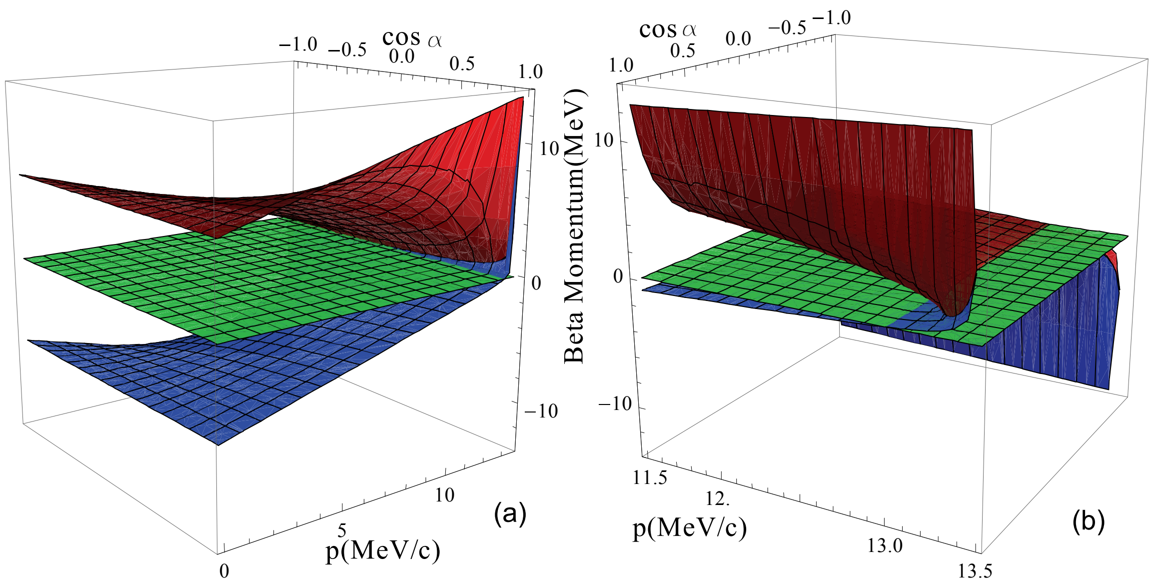

Figure 4.6: Two solutions of the β momentum. The red surface is the solution with the "+" sign in equation (4.14); The blue surface is with the "—" sign, the green surface is the z=0 plane for reference purpose. (a) is the plot in the whole momentum range of p and (b) is the zoomed-in high momentum range of p(p_{max}-2,p_{max}) to show the details of two positive solutions.

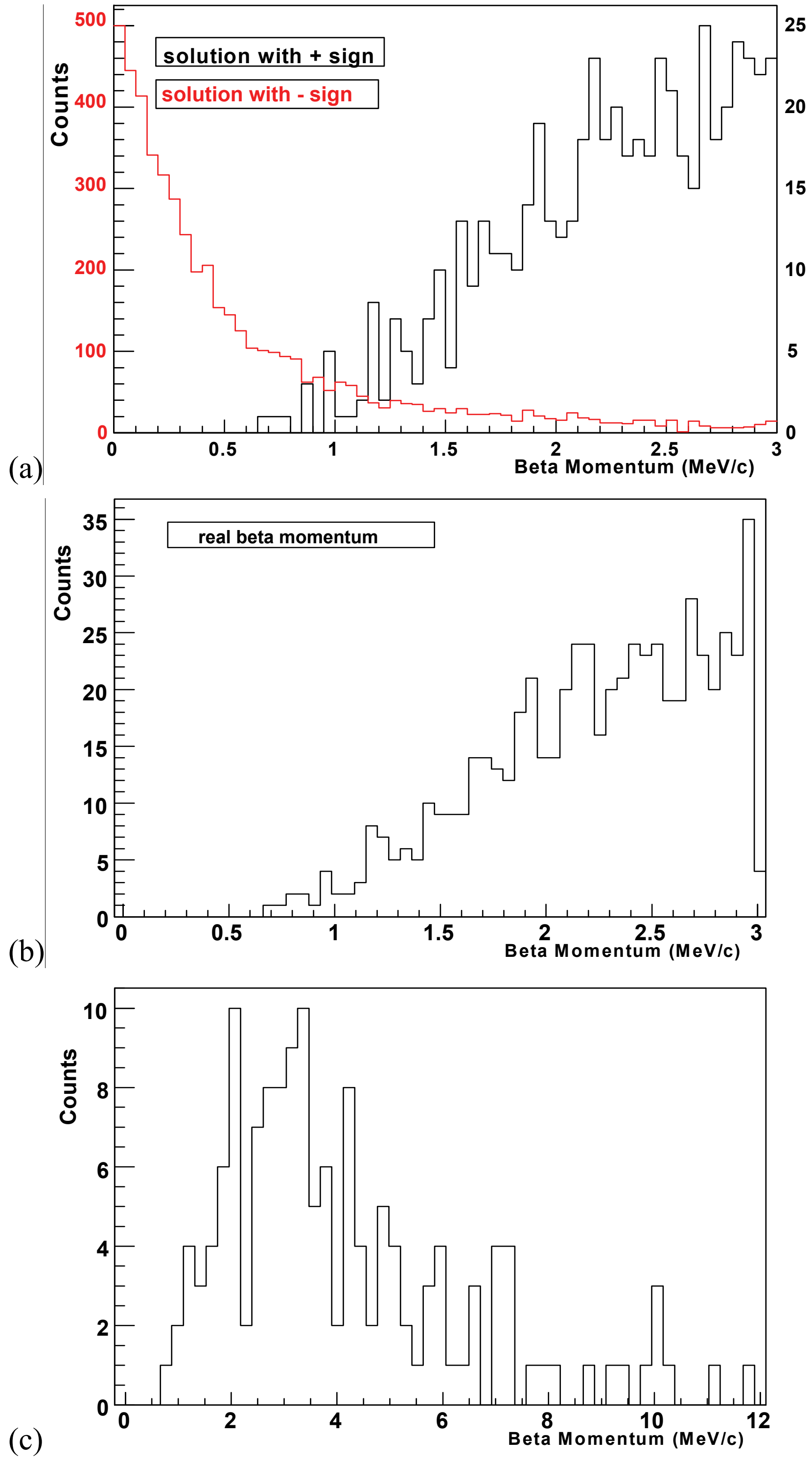

Figure 4.7: β momentum spectra. All spectra are from a simulation of about 10^5 events. $p_{\beta+}$ and $p_{\beta-}$ are solved from equation (4.14). (a) Two solutions $p_{\beta+}$ and $p_{\beta-}$ show the spectrum in the low momentum range (0-3 MeV), when $p_{\beta+}$ and $p_{\beta-}$ are both positive. $p_{\beta-}$ dominates in low momentum. (b) The real β momentum in 0-3 MeV range. (c) $p_{\beta-}$ spectrum in the whole range when it represents the real beta solutions.

4.3.3 Statistic properties in simulation

To compare the simulation with the experimental data, we mimic the same situation as the experiment: if some strips on DSSD are dead, we do not use those strips either; beta directions are obtained from the 1mm SD. To investigate systematic effects we also check the results under various conditions, i.e. assuming the real beta directions are known to study the detector angular resolution effect; using different ion cloud size, etc.

4.3.3.1 Alpha energy difference spectrum

The most direct and sensitive observable to identify the axial-vector coupling or Tensor coupling is the two alphas energy-difference spectrum, as discussed in section 1.6 and shown in Figure 1.4. The simulated two alphas energy-difference spectrum is shown in Figure 4.8 and Figure 4.9, assuming pure axial-vector interaction and pure Tensor Interaction respectively.

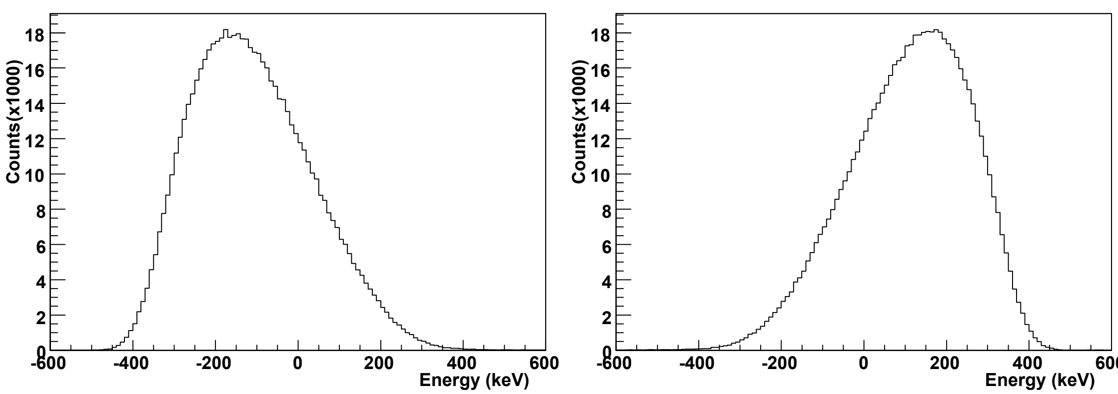

(a) Axial-vector coupling (b)

Figure 4.8: Two alphas energy difference spectra assuming pure axial-vector coupling. X axis is the energy difference between alphas detected by top and bottom DSSDs. The β particles trigger top 1 mm SD in (a), and trigger bottom SD in (b). The conditions of the simulation are described in section 4.2.

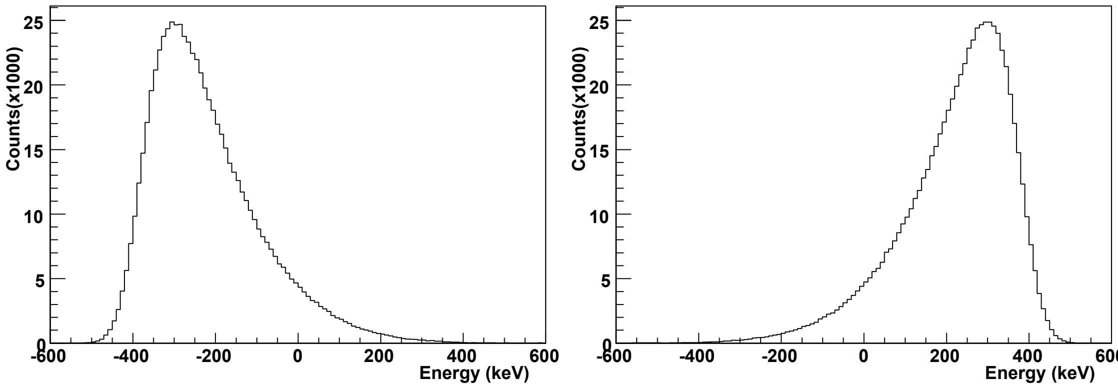

(a) Tensor coupling (b)

Figure 4.9: Two alphas energy-difference spectrum assuming pure tensor coupling. Two alphas hit top and bottom DSSDs, betas trigger top single SD in (a), and betas trigger bottom single SD in (b). The mean energy shift is about 110 keV larger than with pure axial-vector coupling.

4.3.3.2 Beta neutrino angular distribution spectrum

With the two α' momenta and β's direction detected, the neutrino momentum can be solved by equation (4.7) and (4.4); therefore the β-ν angular distribution is obtained. In principle the β-ν angular correlation coefficient *a* can be extracted from the β-ν angular distribution. The angular distribution is certainly affected by the detector geometry and resolution; therefore simulation is necessary when comparing with the data. Figure 4.10 and Figure 4.11 compare the theoretical distribution and the reconstructed distribution from simulation.

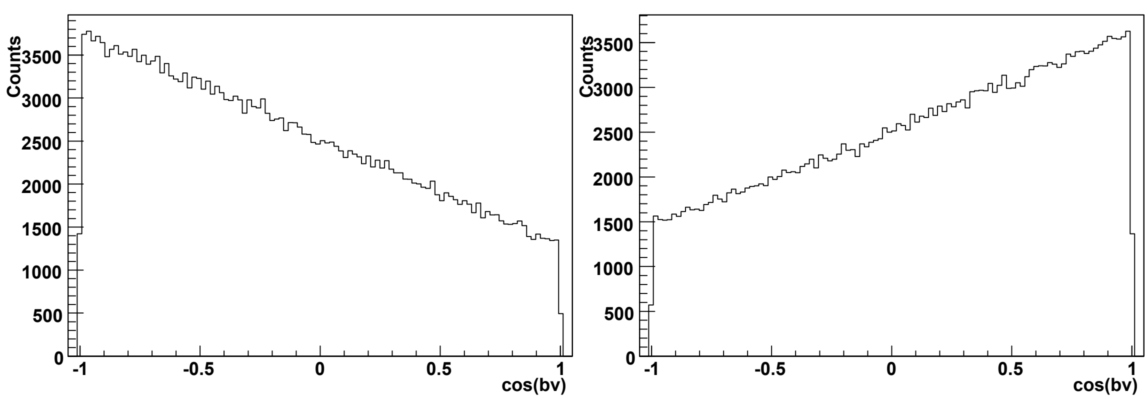

(a) pure axial-vector (b) pure tensor

Figure 4.10: Theoretical β-ν angular distribution. The x axis is the angle between β and ν from the original event generation in the simulation. These are not reconstructed events from detector response.

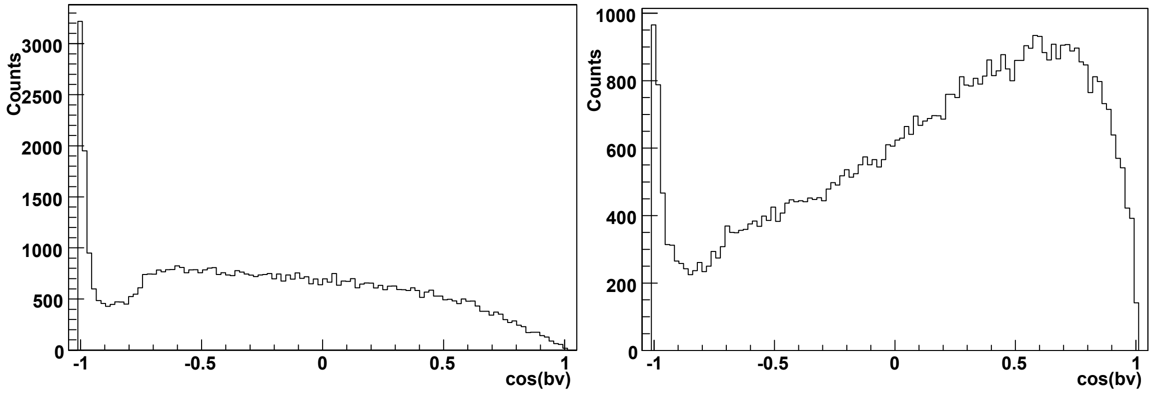

(a) pure axial-vector (b) pure tensor

Figure 4.11: β-ν angular distributions, reconstructed from detector response in Geant simulation. Alpha momentum is read from the DSSD response. Beta particles are recorded in single SD, so the directions can only be assumed to be along the axis which is perpendicular to the silicon detector surface. Both α and β are detected either by the top-bottom pair detectors or by the left-right pair detectors. The significant deviation from the theoretical distribution is mainly due to the angular resolution of DSSDs.

Chapter 5 Measurement and results

5.1 Ion trapping

5.1.1 Strip distribution of α particles

The two α particles breaking up from $^{8}Be^{*}$ decay provide an excellent source to study the ion trap properties. From the hit position pattern of the two α particles on the opposite DSSDs, the ion cloud cooling process, ion cloud size, and ion cloud distribution can be investigated. As illustrated in Figure 5.1, if two α particles are emitted 180° back to back from the trap center they will hit the same strip number on opposite DSSDs. Due to the recoil effect of electron and neutrino, and because ^{8}Li ions are not located exactly in the trap center, the strip number difference on opposite DSSDs forms a distribution centered at 0. An example of this distribution, showed in Figure 5.2, can be fitted to a Gaussian distribution. The FWHM of the Gaussian distribution gives information on the ion cloud distribution. Since the front side strips are along the beam direction and back side strips are perpendicular, the strip difference distributions on both sides can be used to study the ion cloud properties along the axial direction confined by DC potential and in the radial direction confined by RF field independently.

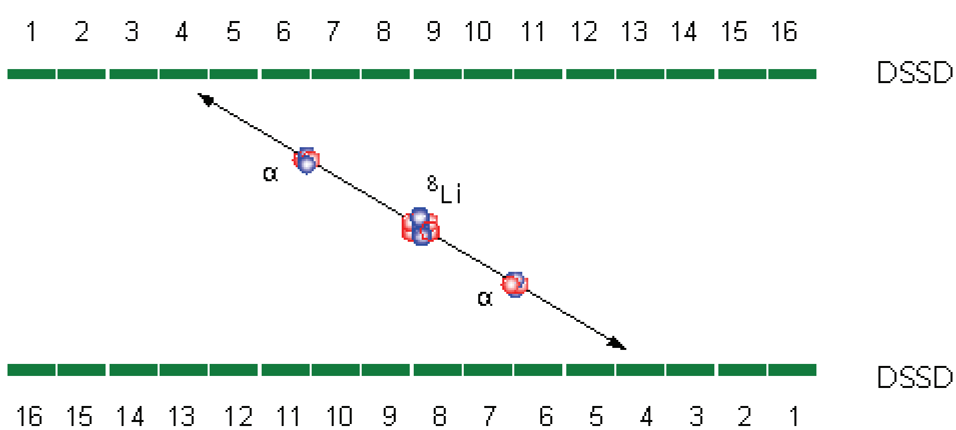

Figure 5.1: Schematic geometry of DSSD and ions. This is a zoomed in cross section view of one pair of DSSD in Figure 3.15. α particles emitted 180° back to back from the trap center will hit the same strip number on opposite DSSDs.

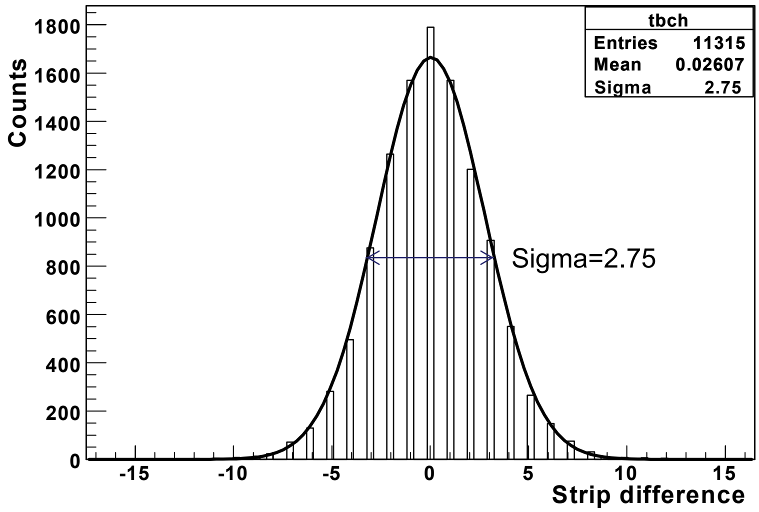

Figure 5.2: Strip number difference distribution. The x axis is the difference of two triggered strip number on opposite DSSDs as shown in Figure 5.1. The distribution is a simulated result assuming 10 mm FWHM Gaussian ion cloud distribution.

5.1.2 Ion cloud size

The ion cloud distribution is determined by the ion motion which has been discussed in section 2.2.2. When $a,q << 1$ (a,q defined in equation 2.10), which is the operation condition of the BPT trap, the ion motion is composed of a macro motion and a micro motion, which can be illustrated by Figure 2.4(a) and Figure 2.5(b). With this ion motion, the ion cloud spatial distribution can be approximated by a two-peaks structure as shown in Figure 5.3. As a first step, we start with a simple Gaussian distribution at the trap center. The FWHM of the Gaussian distribution characterizes the ion cloud size. Under this assumption, the ion cloud size is basically linear with the width of the strip difference distribution, as shown in Figure 5.4. When the ion cloud is small (FWHM< 2 mm), the width of the strip difference distribution is dominated by the kinematic shifts due to the nuclear recoil. When the ion cloud becomes large, the strip difference width is dominated by the ion cloud size. The strip difference distributions from the data have a FWHM of 0.97 in both front and back strips, which correspond to a Gaussian ion cloud distribution with FWHM 1.8 mm. The final ion cloud size is determined by trap field and the buffer gas. How the buffer gas affects the ion cloud is discussed in section 2.2.4 and section 6.2.3.2.

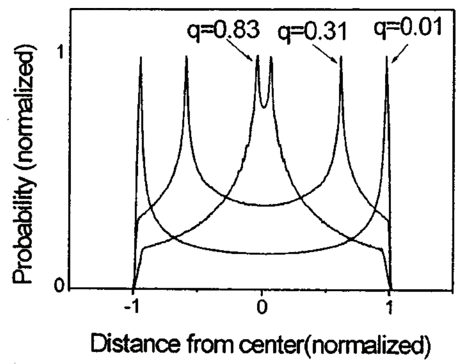

Figure 5.3: Calculated ion cloud spatial distribution in a Paul trap at different values of q based on the Brownian-motion model. Figure is from [76].

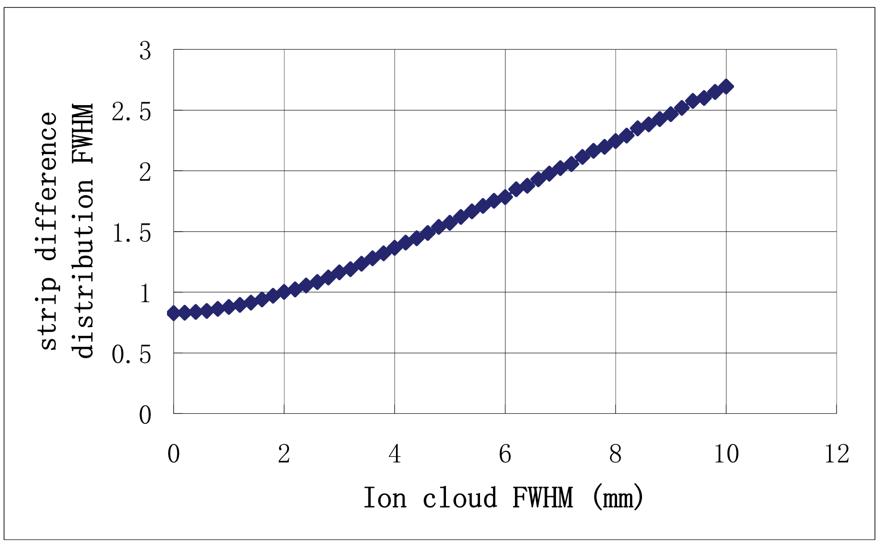

Figure 5.4: Relation between the strip difference distribution and ion cloud size. The x axis is the FWHM of the Gaussian ion cloud distribution used in the simulation. The y axis is the FWHM of the strip difference distribution as shown in Figure 5.2. When the FWHM in the simulation is 0, the width of the strip difference distribution is purely due to the recoil effect of electron and neutrino.

5.1.3 Ion cooling

As section 2.2.4 discussed, the average motion of an ion under an applied electric field E can be approximated by

$$m\ddot{x} = -\frac{e}{k}\dot{x} + eE \qquad (5.1)$$

Where m = 1.33×10^{-26} kg is the mass of $^{8}Li^{+}$. k is the reduced mobility of $^{8}Li^{+}$ in helium at experimental temperature T and pressure p, which can be obtained from k = $(N_0/N)\times k_0$

$= k_0\times(p/p_0)\times(T_0/T)$, where $k_0 = 22\ cm^2/(Volt\text{-}sec)$ [77] is the mobility at p_0=1 atm, T_0 = 18 ℃. The trap is cooled close to liquid nitrogen temperature T=77 K, and helium gas pressure is measured to be p = $2.3\times10^{-6}/0.18$ torr = 1.3×10^{-5} torr, where 0.18 is the gas correction factor for helium gas in the ion gauge [78].

Along the axial direction the ions are confined by a DC potential, which is approximately expressed as following near the trap center.

$$\Phi = \Phi_0 x^2 \tag{5.2}$$

where $\Phi_0 \approx 2\times10^4$ V from Simion7 [79] at our trap geometry and operation voltage, and x is the distance along the axial direction from the trap center in the unit of meter. The electric field can be expressed as:

$$E = -d\Phi / dx = -2\Phi_0 x \tag{5.3}$$

The solution of Equation (5.1) is:

$$x_{[t]} = x_{[0]} + c \cdot \exp(-140t) \cdot \sin(7\times10^5 t) \tag{5.4}$$

where c depends on the initial velocity. The sinusoidal part represents the ion oscillation in the DC field and the exponential part represents the damping effect from the buffer gas.

The ion cooling process can be followed by the hit pattern of opposite DSSDs. As discussed in the previous paragraph, the width of the fitted Gaussian function to the strip difference is directly proportional to the ion cloud size. The data shows that the ion cloud size decreases exponentially with time for about 20 ms after the ions are loaded until the ion cloud reaches the final size, as shown in Figure 5.5.

The ions were confined in a small bunch in the isobar separator and then loaded into the BPT (Figure 3.7). The ions obtain about 100 eV energy during the loading process, and spread out quickly along the beam direction. The spread of ions in this direction is measured by the back strips of the DSSDs. The cooling process measured in this direction generally agrees with the calculation. The most uncertain value used in the calculation is the buffer gas pressure, because the ion gauge is outside of the trap.

The black curve in Figure 5.5 shows the ion cloud size change perpendicular to the beam direction. The ion cloud dimension here is much smaller than that in the beam direction after loading because the ions do not gain energy directly in this direction from loading.

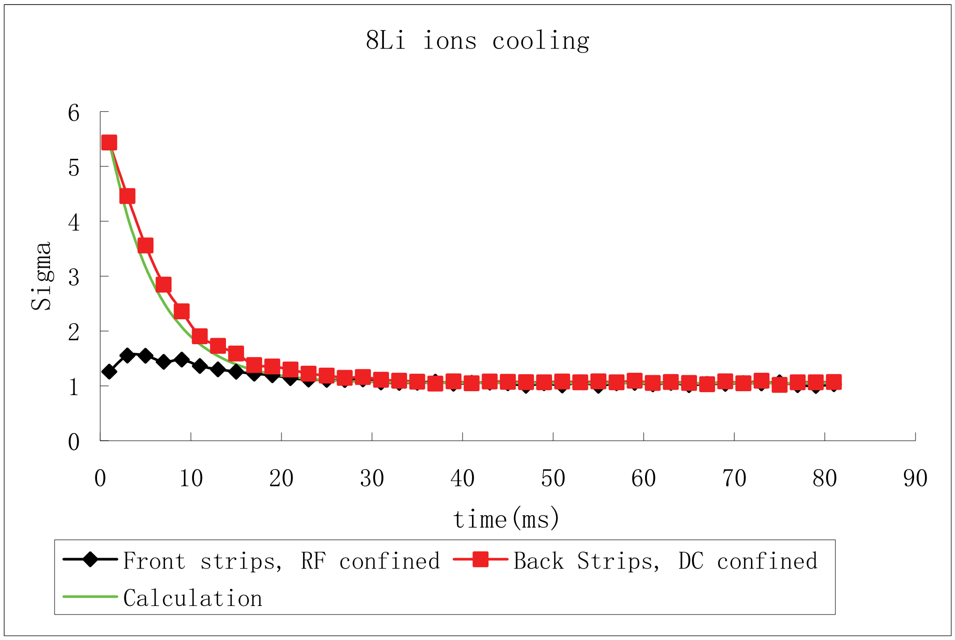

Figure 5.5: Ion cooling after capture, in both the beam direction confined by DC potential (red line), and perpendicular to the beam direction confined by RF field (black). The green line is the calculated cooling process based on equation (5.4), with added offset to match the final ion cloud size.

5.1.4 Ion storage

The trap ion storage lifetime has been tested offline with stable nucleus ^{14}N. By adjusting the time interval between capture and subsequent ejection of the ion bunches, the number of ions that remain trapped can be determined as a function of storage time. The ejected ions hit an MCP detector and the number of ions can be approximately determined by the total signal charge. The ion detections by the MCP detector at different storage time are shown in Figure 5.6. After the ions are initially loaded into the trap, they spread out in a large space so the signal on the MCP detector does not show a clear peak. After 25 ms, a peak clearly shows up which means that the ions have been cooled into a small cloud. After 4 seconds there is no obvious attenuation of MCP signal, so the trap lifetime is much longer than 4 seconds. For ^{8}Li, with a half-life of only 0.84 second, essentially all of the ions will decay within the trap.

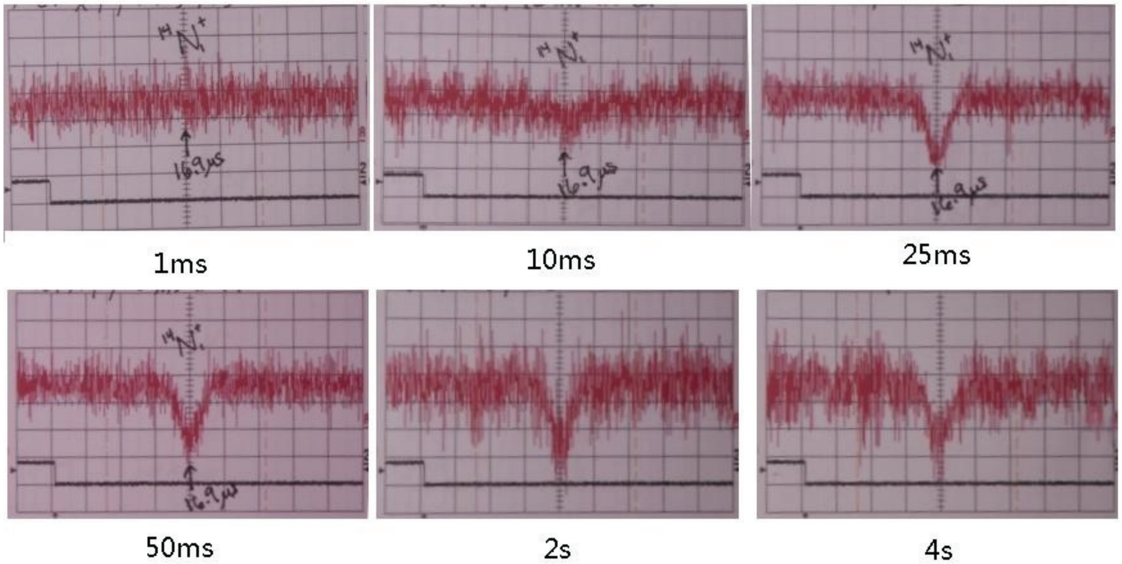

Figure 5.6: MCP detector signal vs. storage time

The trap lifetime can also be estimated from the online ^{8}Li data by looking at the decay rate of trapped ^{8}Li, as shown in Figure 5.7. The detected decay rate depends on both the ^{8}Li decay half life and trap storage lifetime.

$$N = \frac{1}{2} N_0 \exp(-1/T_{Li} - 1/T_{trap}) \tag{5.5}$$

The ions require about 20 ms to be cooled as shown in Figure 5.5, and confined into a small cloud (less than 4 mm^3). The detection efficiency during this period is less than that when ions are confined, so the first 20 ms data are not included in Figure 5.7. The BPT trap captures ions every 100 ms, limited by the trapping lifetime of the isobar separator. Due to a vacuum contamination right before the experiment, the isobar separator has a very short lifetime of about 50 ms. To prevent losing too many ions, the isobar separator has to eject ions to the BPT frequently. Compared with the ^{8}Li half life of 840 ms, the 100 ms BPT capture cycle is too short for a precise half-life measurement. The data still give an exponential decay with a slope of $-(8.1\pm1.3)\times10^{-4}$/ms, corresponding to the half life of $T_{1/2}$= 878±141 ms, which is consistent with the ^{8}Li half life, and indicates that the trap storage lifetime is much longer than the ^{8}Li half life.

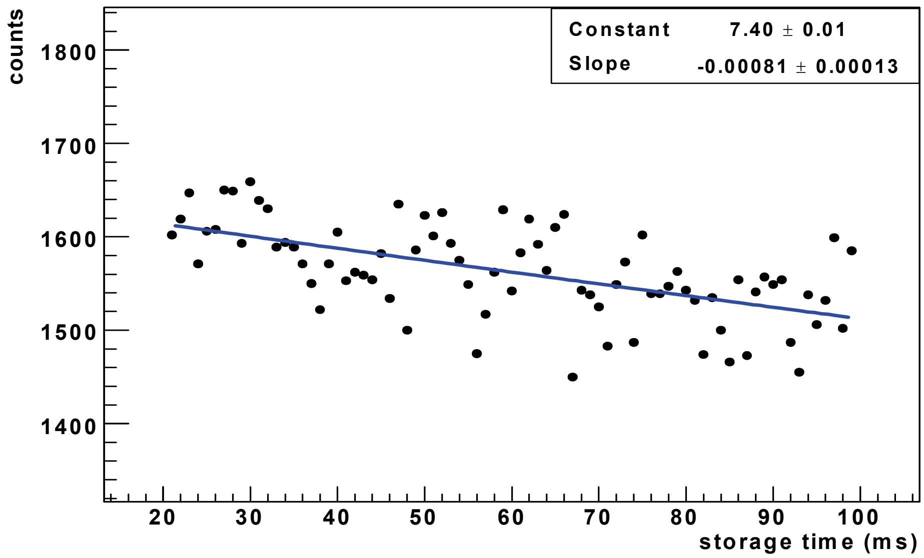

Figure 5.7: Number of ^{8}Li decays during the capture cycle. The x axis is the time after capture and the y axis the number of observed decays. The blue line is the fitted exponential function $N = Ce^{-S \cdot t}$, where C is the Constant and S is the Slope in the text box of the picture.

5.1.5 Detector position

In reconstructing each event it is important to know the direction of the two alpha particles. The geometry of the trap is designed to be able to mount the detectors within 0.2 mm tolerance, and the position of DSSD can be further corrected from the hit pattern of the two alpha particles. If the detectors are symmetrical with respect to the ion cloud, the hit pattern should be centered at zero. The deviation from zero indicates a detector mounting offset. This effect has been studied with the Geant4 simulation. Table 5.1 summarizes the results of the simulation.

The offset of DSSD pair positions from trap center can be estimated by the mean values in Figure 5.8. The results are summarized in Table 5.2. The top and bottom pair lies within the design tolerance. The significant offset in the left and right pair is due to the defective manufacture found after the experiment. The right DSSD active area is not centered at the detector board. This offset can be corrected in the Geant4 simulation.

DSSD offset (mm)	0.2	0.4	0.6	0.8	1
center of strip difference distribution	0.068	0.127	0.200	0.239	0.332
calculated offset (mm)	0.21	0.40	0.63	0.75	1.04

Table 5.1 Simulation of the detector offset. The first row is the offset of one DSSD along axial direction. The second row is the mean value of the strip difference distribution similar as Figure 5.8. The third row is the calculated offset based on the mean value, by multiplying the mean value with the strip width 3.125 mm. The calculated offset is within 0.05 mm of the actual offset which is due to statistics.

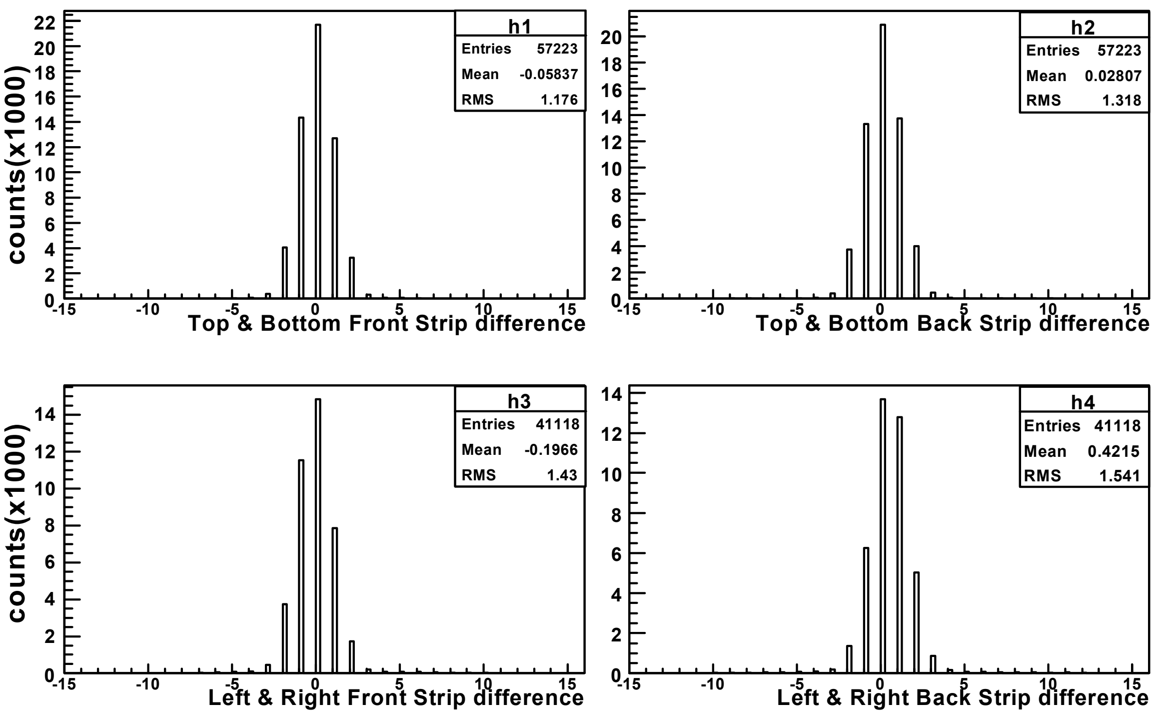

Figure 5.8: Strip difference distribution of two pairs of DSSD. The front strip is along the beam direction and the back strip is perpendicular to the beam direction.

DSSD pair	Top Bottom Front	Top Bottom Back	Left Right Front	Left Right Back
Center of strip difference	-0.058	0.028	-0.197	0.422
calculated offset (mm)	-0.18	0.09	0.62	1.32

Table 5.2: Detector offset indicated by the strip difference spectrum.

5.2 Energy calibration

5.2.1. Calibration sources

The calibration sources are made of ^{148}Gd which provides an α energy of 3182.69 keV, and ^{244}Cm, which provides an α energy of 5804.77 keV. The sources were dissolved in dilute HCl and deposited on Au foils, shown in Figure 5.9. The sources are deposited at several locations on a Au foil and four Au foils are attached to the outer layer of the RF shield to be able to illuminate every strip on every DSSD, with a rate of about two events per second per strip. The positions of the detectors and the calibration sources are shown in Figure 5.10.

5.2.2 α source energy calibration

The sources stay in the trap during the experiment to give a real time energy calibration and provide a monitor for the detector performance. A typical spectrum from the calibration source is shown in Figure 5.11. The calibration source does not contribute background to the ^{8}Li decay measurement because the α-α-β triple coincidence significantly reduces all background.

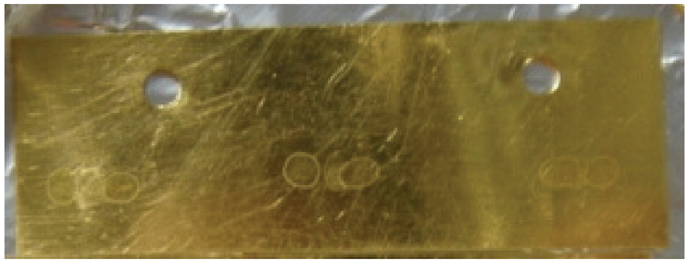

Figure 5.9: Calibration alpha sources. ^{148}Gd and ^{244}Cm are each deposited at three locations.

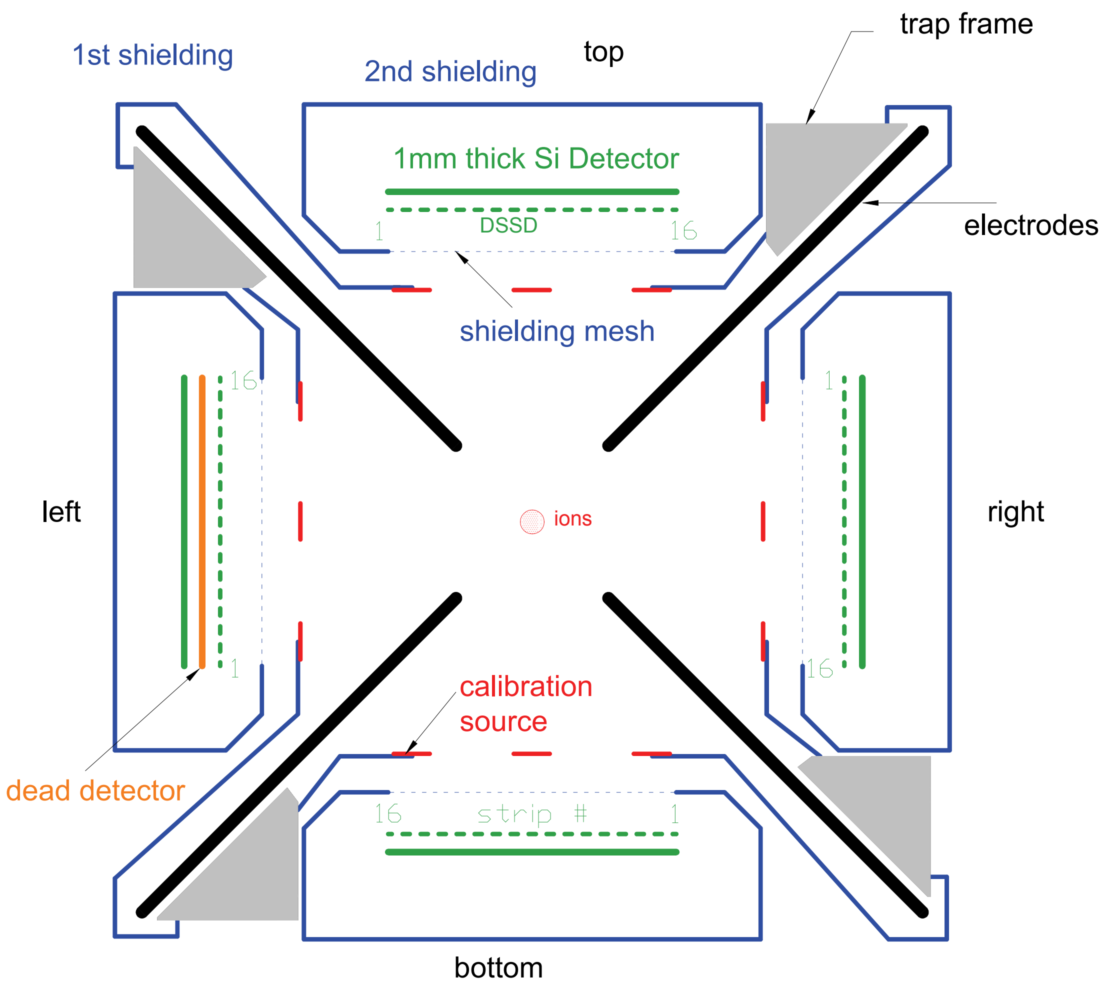

Figure 5.10: Trap, detector and calibration source geometry.

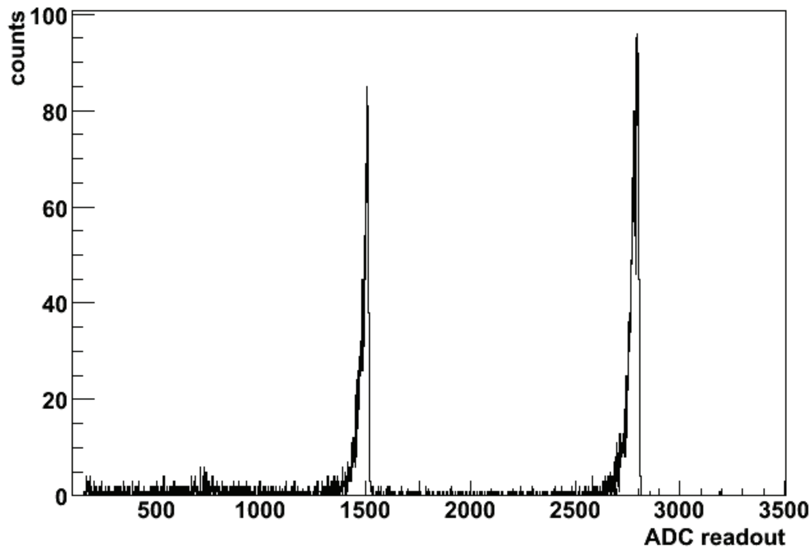

Figure 5.11: A typical spectrum from the calibration sources. The two peaks correspond to 3183 keV and 5805 keV.

5.2.3 Source thickness

The sources were not specifically made to be very thin, which makes the energy calibration a little more difficult. The thin sources will be made for the future experiments. Some a particles lose energy when passing through the source material, broadening the low energy slope of the energy spectrum (as seen in Figure 5.11). α particles emitted from the surface of the source still deposit full energy in the detector, so the high-energy falloff from the two strong alpha lines remains quite sharp (as seen in Figure 5.11).

To study the source thickness effect, we compared our sources with a very thin ^{148}Gd source. Figure 5.12 confirms that even with the significant low energy tail, the peak and especially the high energy falloff of our sources are very close to the thin source.

The peak position of the calibration source is neither selected as the highest point nor fitted to a Gaussian distribution because the low energy tail slightly affects the peak. The positions of the two calibration sources are selected as following:

$$peak = X_{HM} - \tfrac{1}{2} FWHM \qquad (5.6)$$

where X_{HM} is the position at the half-maximum on the high energy side of the ^{148}Gd or ^{244}Cm spectra. The FWHM is not obtained from the calibration source energy spectra due to the low energy tail, but obtained from the pulser signal as mentioned in section 3.10.5. The width of the pulser signal represents all the noise from detector and electronics.

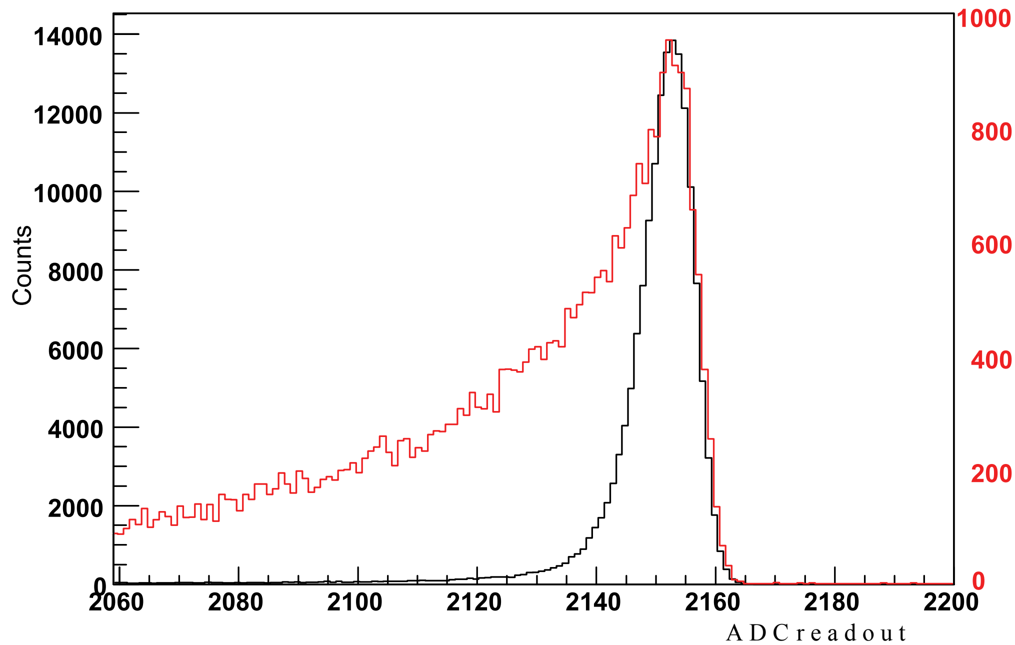

Figure 5.12: Comparison between the BPT ^{148}Gd calibration source and a very thin ^{148}Gd source. The black spectrum is the peak from the thin source and the red line is the spectrum from the BPT source. The peaks and high energy falloffs of the two sources are very close to each other regardless of the low energy tail.

5.2.4 Detector dead layer

The DSSD is furnished with a thin layer of aluminum on each strip, for electrical contact. The DSSDs were initially manufactured for measuring the beta directions for another project, so the aluminum layer was not specified to be very thin. The energy loss for 1.5 MeV alpha particles in the aluminium window is significant. A thin region also exists near the surface of the bulk semiconductor in solid state radiation detectors to which the depletion region does not extend. The ionization produced in this region is not collected by the detector. Since the energy loss in neither the aluminum window nor this silicon region will be collected, the combination of these two regions is usually called the dead layer.

The dead layer is determined by measuring the energy of α particles from the same calibration sources used in the experiment. The source is placed at two locations one after another to form different angles to the DSSD. The first location is 65 mm vertically away from DSSD front side giving a normally incident angle to the DSSD center point. The second location is moved horizontally along front strip direction by 65 mm, giving a 45°

incident angle to the DSSD center. Each pixel on the DSSD, which is defined by the cross of front and back strip, will receive α particles from two different angles. The energy calibration on each pixel is obtained from both the ^{148}Gd and ^{244}Cm sources. The dead layer of each pixel is calculated from the energy lost of α particles from ^{148}Gd, because they lose more energy than the alphas from ^{244}Cm. The SRIM program [80] is used to calculate the energy loss rate dE/dx of α particles in aluminium at different energies, as shown in Figure 5.13. The calculated dead layer profile from one DSSD is plotted in Figure 5.14 and the measured dead layer thickness for top, bottom, left and right detectors (referring to Figure 5.10 for detector geometry) are 0.62±0.05 μm, 0.60±0.05 μm, 0.6±0.1 μm, 0.6±0.1 μm respectively. The larger uncertainties on the left and right DSSD are due to limited statistics. With this precision of the measured dead layer thickness, the correction to the final result is below the statistical uncertainty.

The dead layer correction of α particle energies in ^{8}Li decay is done in the following way. For each DSSD a uniform dead layer is assumed, but for each pixel the actual thickness d is corrected based on the incident angle of the α particle. The energy loss △E in the dead layer is added to the measured energy by integrating the energy loss rate provided by SRIM as Figure 5.13:

$$\Delta E = \int_0^d (dE/dx)\cdot dx \tag{5.7}$$

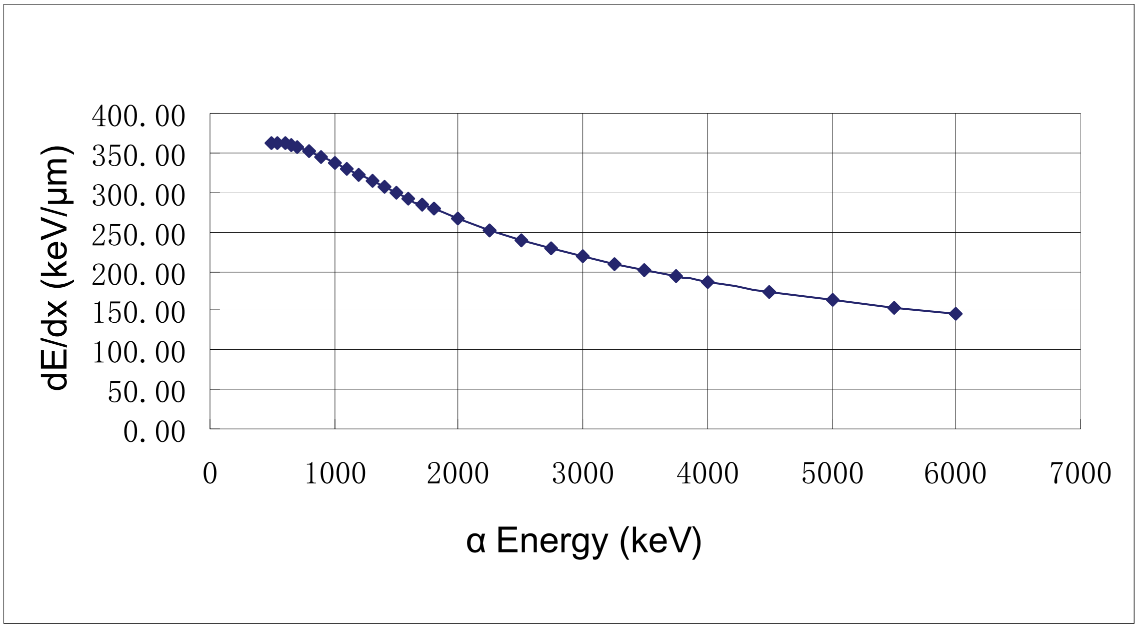

Figure 5.13: α energy loss in aluminium as a function of energy. Data points are from SRIM. The line is a cubit function fitted to the data points and used in equation (5.7).

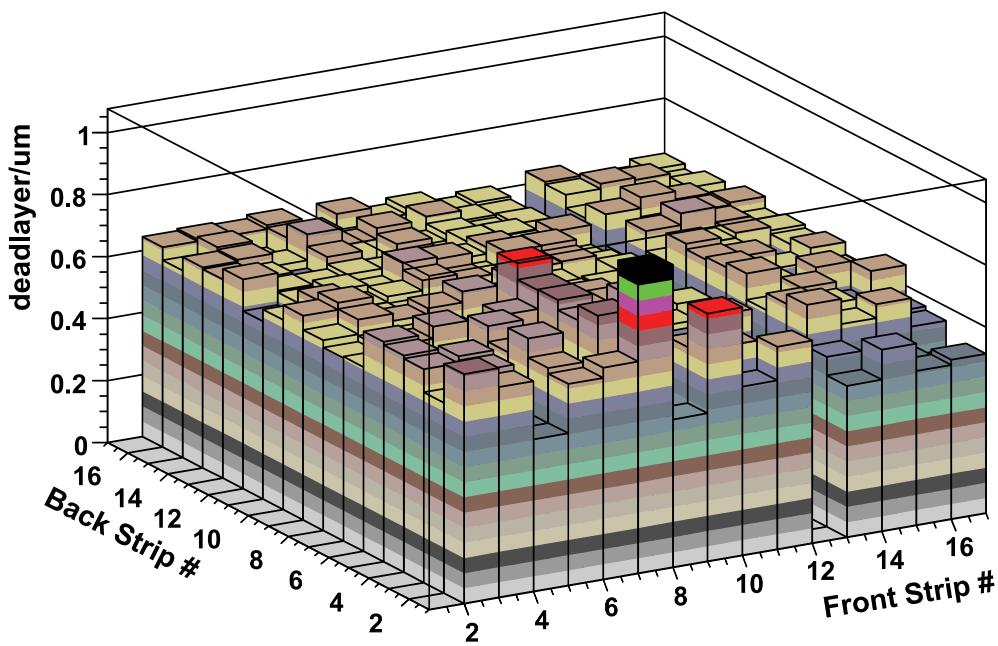

Figure 5.14: Dead layer measurement on each pixel of the top DSSD. Note that there is no data on front strip 1 and 12 due to a loose connection. Only a few pixels have significant deviation from the average.

5.2.5 Gap effect

Neighboring DSSD strips are separated by an insulating SiO_2 gap on both front and back sides. When an α particle hits the gap on the front side, one of the neighboring strips will produce a reduced pulse height. As shown in Figure 5.15, the events that do not lie on the diagonal line are produced in the gaps. This is due to the distorted electric field between the strips [81].

In Figure 5.15, 95% of the events are located in region 1, which are the normal events depositing full energy of ^{148}Gd and ^{244}Cm in the DSSD. The events located in the diagonal line but with less energy than the two peaks are from the α particles that lose part of energy in the source material. The events in region 2 are from α particles hitting the front strip at the position corresponding to the gap of the back strips. The front strip collects the full charge while the charge spits into the back two adjacent strips. The events in region 3 are produced when α particles hit the gap between the front side strips. The reduced energy response is believed to occur because of negative charge trapping due to the shape of the electric field between the strips [81]. Most of these gap events are centralized in a peak which is at about half of the full energy peak. However there is also a continuum of the gap event distribution from zero energy up to the full energy. This distribution is in agreement with the proposed model of Yorkston et. al. [81].

The gap events can be removed by requiring that the α energies measured by the front and back side to match each other. Figure 5.16 is the ratio of the energy measured by the front side to the energy measured by the back side of the DSSD. The width of the peak in Figure 5.16 is mainly due to the different energy calibrations on front and back sides. The long high value tail is due to the gap effect. On the left side of the peak center all events fall in the window of (0.85~1). Assuming symmetry for the good event distribution, 1.15 is a reasonable value to cut the gap events.

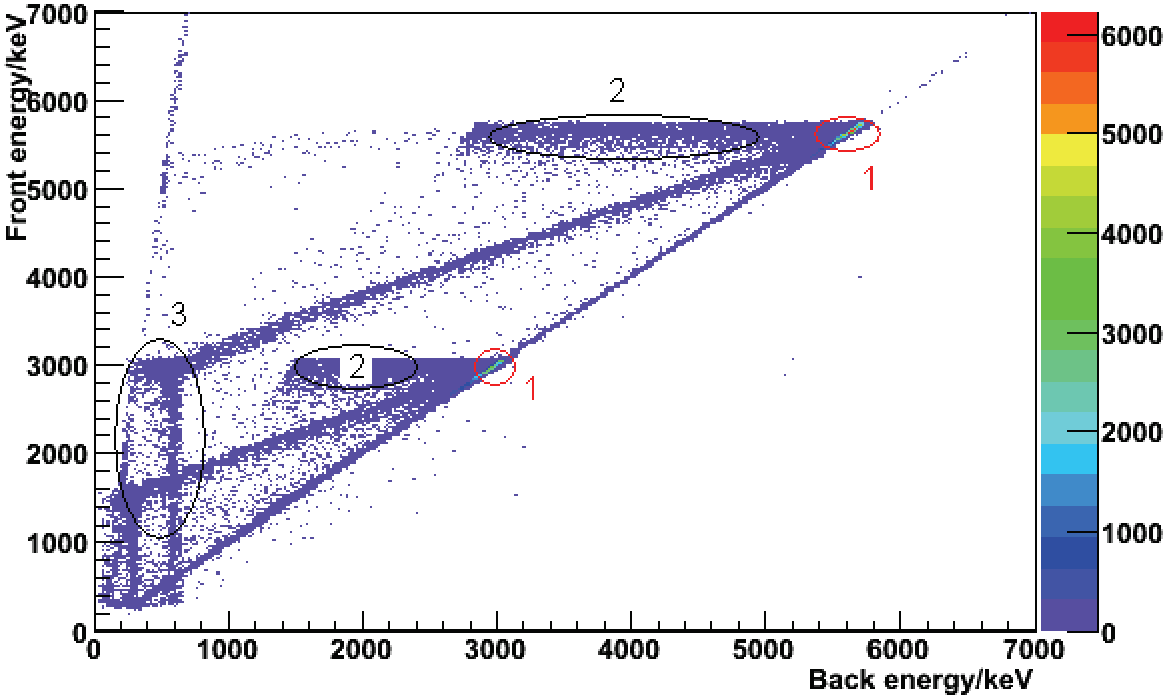

Figure 5.15: Front and back side DSSD response to ^{148}Gd and ^{244}Cm sources. Front strip # 8 (a typical strip), vs. all back strips. The x axis is the energy read from the back side and the y axis is from the front side.

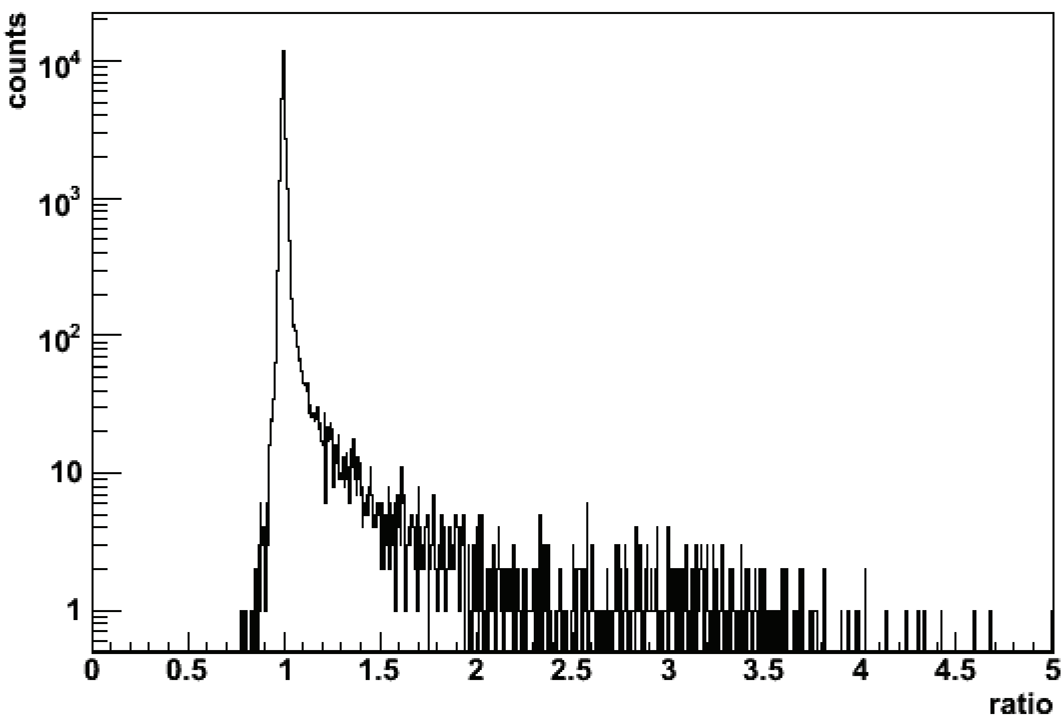

Figure 5.16: The ratio of the alpha energy measured by all strips of the front side and back side of the top DSSD. The events are from the calibration alpha source.

5.3 Alpha energy spectrum

5.3.1 Alpha energy sum spectrum

The broad ^{8}Be final-state continuum populated in ^{8}Li β decays has been precisely measured [75]. The two alpha's energy sum spectrum is sensitive to the energy calibration and the detector dead layer measurement. The measured energy sum spectra in our experiment are compared with the published result in [75], and they basically agree with each other. This is just to verify that the detectors are functioning properly.

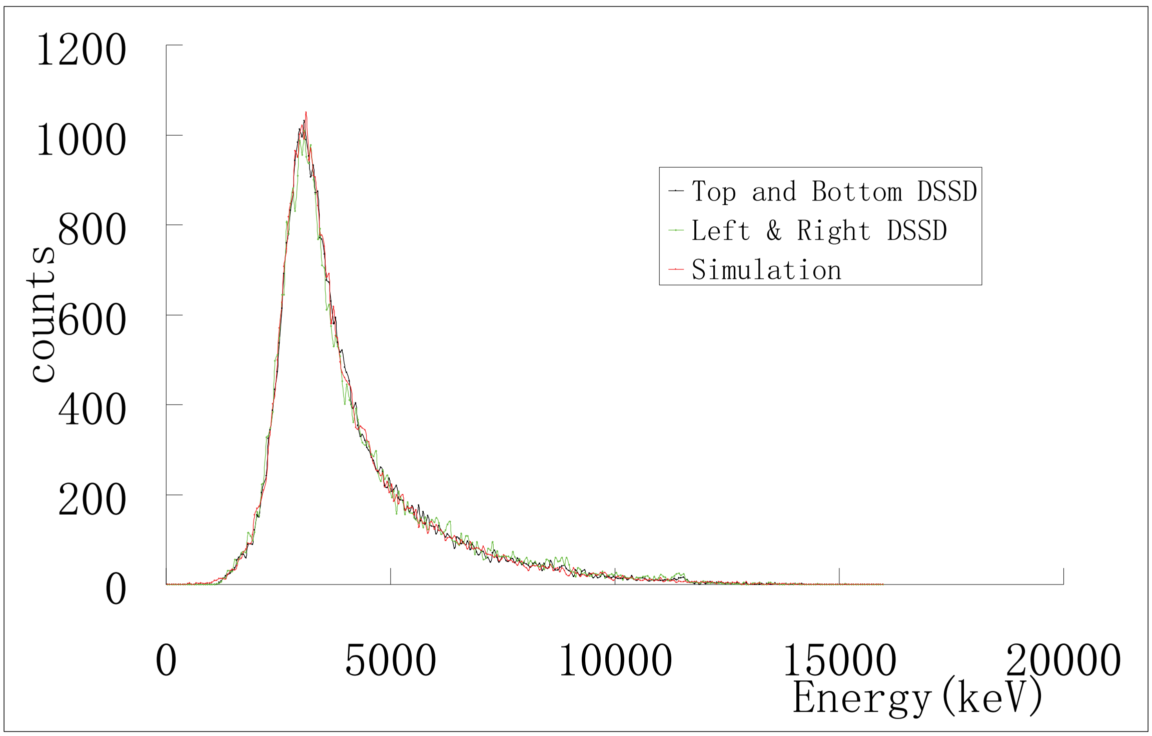

Figure 5.17: The alpha sum spectrum from the top and bottom pair DSSD, from the left and right pair DSSD, and from the simulation. There is no cut on the electron direction. The total number of counts has been normalized. The measured spectra are in good agreement with the simulation based on a published measurement [75].

5.3.2 Alpha energy difference spectrum

When the electron momenta are parallel with the α particles momenta, the energy difference spectrum is sensitive to any mixture of tensor interactions. As discussed in section 1.6.4 when the electrons and the alphas are measured along the same axis the neutrino angular distribution is approximately $W(\theta_{\beta\nu}) = 1 + \frac{v}{c}\cos\theta_{\beta\nu}$ for Tensor interaction and $W(\theta_{\beta\nu}) = 1 - \frac{v}{c}\cos\theta_{\beta\nu}$ for axial-vector, where $\theta_{\beta\nu}$ is the angle between the electron and the neutrino, resulting in a correlation which has the maximum sensitivity to any tensor admixture. This difference is further enhanced by the fact that ^{8}Be breaks into two α particles, which transfer the ^{8}Be kinetic energy to the two α particles energy difference by a factor of $2v/V$ (typical value of several tens), where v and V are the velocities of the a and the ^{8}Be, respectively. (Figure 1.4). All these considerations make it possible to get a meaningful result with rather few events.

When the electrons momenta are perpendicular to the α particles momenta, the energy difference spectrum should be symmetric about zero and therefore it can be used to check for systematic effects.

5.3.2.1 Electron direction detection

The electron is detected by the 1 mm thick silicon detector (SD) behind the DSSD (as seen in Figure 5.10). Electrons do not deposit full energy in the SD; therefore only the β directions are obtained from the SD. A typical β spectrum is shown in Figure 5.18.

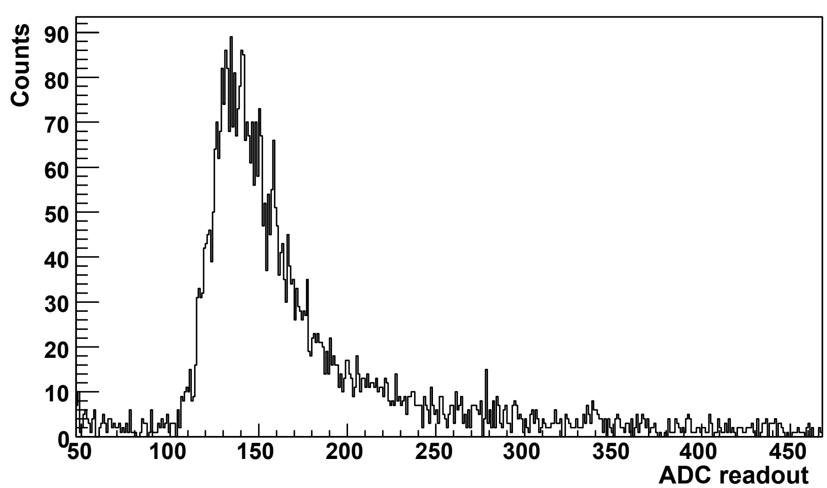

Figure 5.18: β spectrum of bottom SD. The high energy tail is due to the β scattering inside of the detector material.

5.3.2.2 Data from top and bottom DSSDs

The mean value of the two α's energy difference spectrum without considering the β direction should be zero but there is an offset indicated by Figure 5.19. This offset could come from the uncertainty of the energy calibration or dead layer measurement, while the possible mixture of tensor interaction will not cause this offset. The simplest way to correct this offset is to linearly move the whole spectrum by adding 7 keV in Figure 5.19 to make it centered at zero. The analysis hereinafter shows the result after this correction.

The energy difference spectra of two alphas detected by top and bottom DSSDs with beta detected in four different directions are shown in Figure 5.20. The spectrum is built under two conditions: (1) the ions have been loaded in the trap for more than 20 ms, which is the time required to thermalize the ions and (2) the α energies measured by the front and back side of the DSSD agree to within 10%; otherwise this would indicate a hit in the gap between adjacent strips, known as the gap effect [81]. The stringent triple coincidence of two α particles on opposite DSSD within several hundreds of keV energy difference and a clear β signal essentially removes almost all background.

Due to the symmetry between the top and bottom detectors, the spectra in Figure 5.20 should be symmetric between electrons going up(Figure 5.20(a)) and down(Figure 5.20(b). When we fit the data, we combine these two spectra together to get a higher statistics and to cancel the energy calibration offset to first order. The combined spectrum is obtained by reversing the spectrum of Figure 5.20(b) then adding these two spectra together. The comparison of the combined spectrum and the simulated spectra for a pure axial-vector and a pure tensor interaction is shown in Figure 5.21.

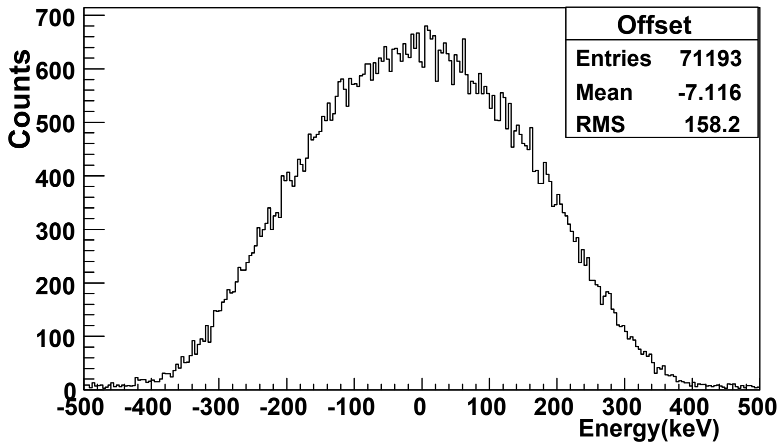

Figure 5.19: Energy difference spectrum of two α's detected by top and bottom detector, with electrons going any direction (not necessary observed by a detector). The X axis is the top α energy minus bottom α energy.

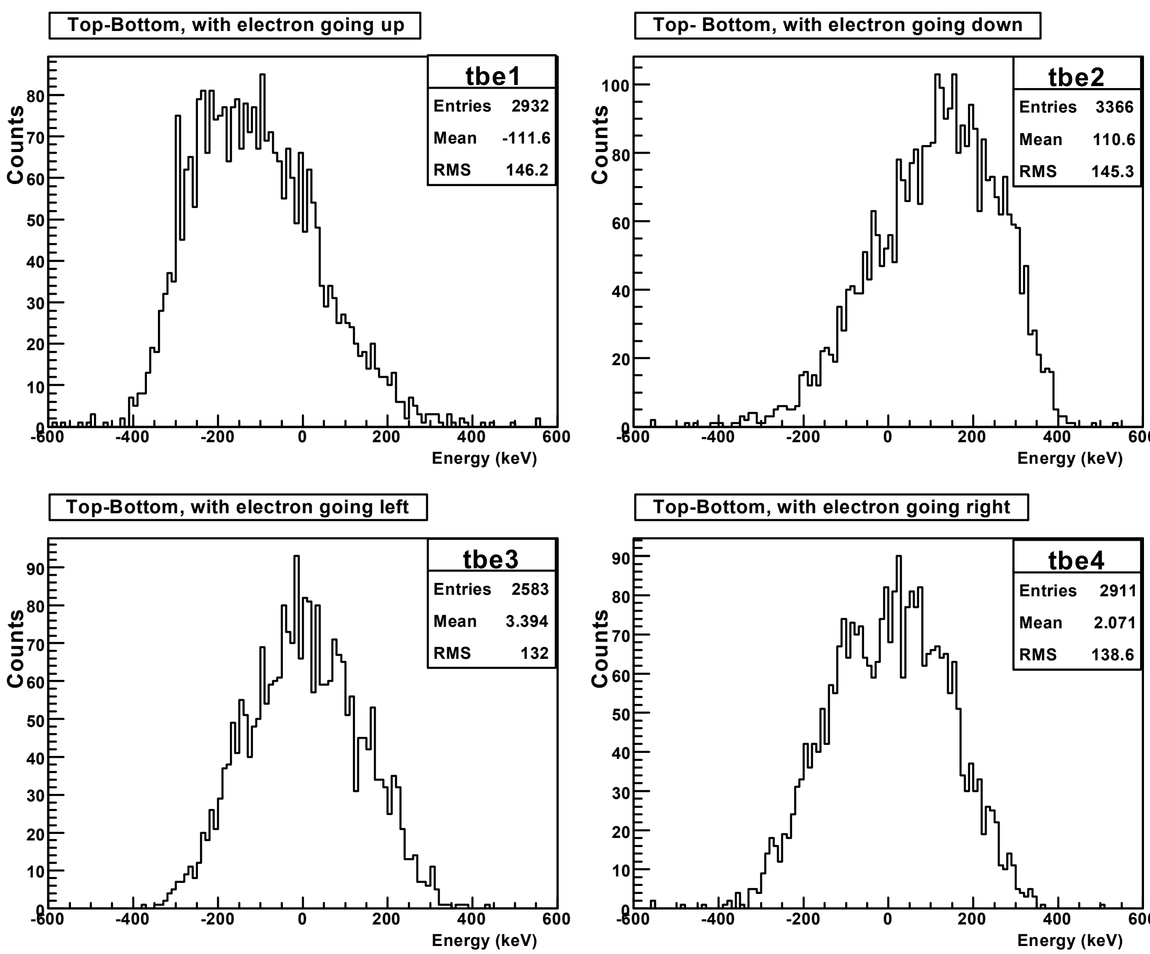

Figure 5.20: Energy difference spectrum of two α's from top and bottom DSSDs.

The function

$$f = c \cdot f_A + (1-c) \cdot f_T \tag{5.8}$$

is fitted to the combined spectrum in Figure 5.21. The fitting function f is the linear combination of two simulated spectra f_A and f_T, in which f_A is the spectrum assuming pure axial vector coupling, and f_T is the spectrum assuming pure tensor coupling; c is the only fitting parameter which represents the amount of the axial vector interaction. The simulations are taken under the following conditions: 1.8 mm FWHM Gaussian ion cloud distribution; 0 initial ^{8}Li kinematic energy; trap set up includes detectors, detectors shielding, trap frame, electrodes, detector mounting plates, two plates at each end of trap; one million α-α-β coincidence events in both f_A and f_T.

The Maximum Likelihood method is chosen over the Least Squares method to fit the data. The counts in each bin do not have high statistics and they obey the Poisson distribution. With limited numbers of entries in bins, the least squares method could result in error larger than statistical uncertainty [82]. An experiment comparing these two methods with gamma spectrometry confirms that with high statistics the counts in each bin are close to a Gaussian distribution, and the Least Square method is justified, while for low statistical quality spectra the Maximum Likelihood method is more suitable [83]. The following likelihood function *l(c)* is minimized to search for the fitting parameter c in function (5.8):

$$l(c) = \sum_{i=1}^{N} Ln \frac{f_{i(c)}^{y_i} \exp(-f_{i(c)})}{y_i!} \tag{5.9}$$

where the summing is performed over the N bins, y_i is the bin count of experimental data and fi is the fitting function (5.8).

The fit result from the top-bottom pair of detectors gives $c = 1.000 \pm 0.012_{(stat)}$, which is consistent with the Standard Model prediction that the interaction is pure axial vector.

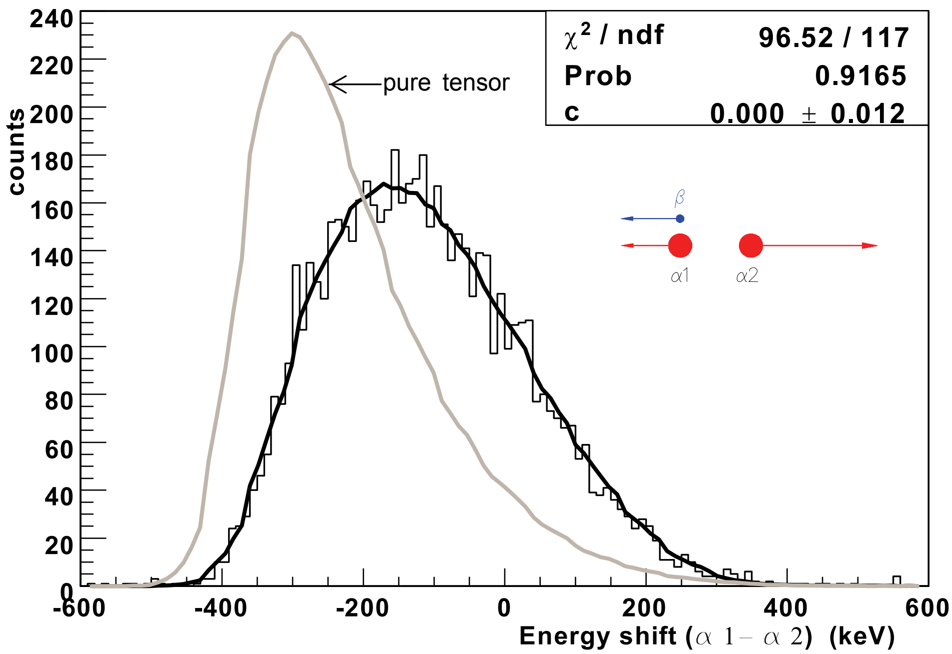

Figure 5.21: The result from top and bottom DSSDs. The data are the combined alpha energy difference spectrum from top and bottom DSSDs, with electrons detected by the top or bottom single silicon detectors. The grey line is the lineshape for a pure tensor interaction and the black line is the lineshape for a pure axial-vector interaction. The resulting fit is not distinguishable from a pure axial-vector spectrum.

5.3.2.3 Data from left and right DSSDs

The left and right pair of DSSDs also observes the similar offset as the top and bottom pair (as seen in Figure 5.19), and the offset is adjusted in the same way. The energy difference spectra of two alphas detected by the left and right DSSDs with beta detected in four different directions are shown in Figure 5.22. The detector geometry of the left and right pair is not completely symmetric. When the electron's direction is up or down, the mean value of the energy difference spectrum should be 0. However, the actual mean value is 7.0 keV when electron goes up, and is -5.3 keV when electron goes down (as seen in Figure 5.22). This is mainly due to the dead strips on left and right DSSD. Strip 16 on the left DSSD and strip 12 on the right DSSD are dead (the strip number can be referred in Figure 5.10). Therefore the average active area of the left DSSD is lower than the right DSSD. When the electron goes up, the left DSSD has a slightly larger chance to catch the α particle which is going down.

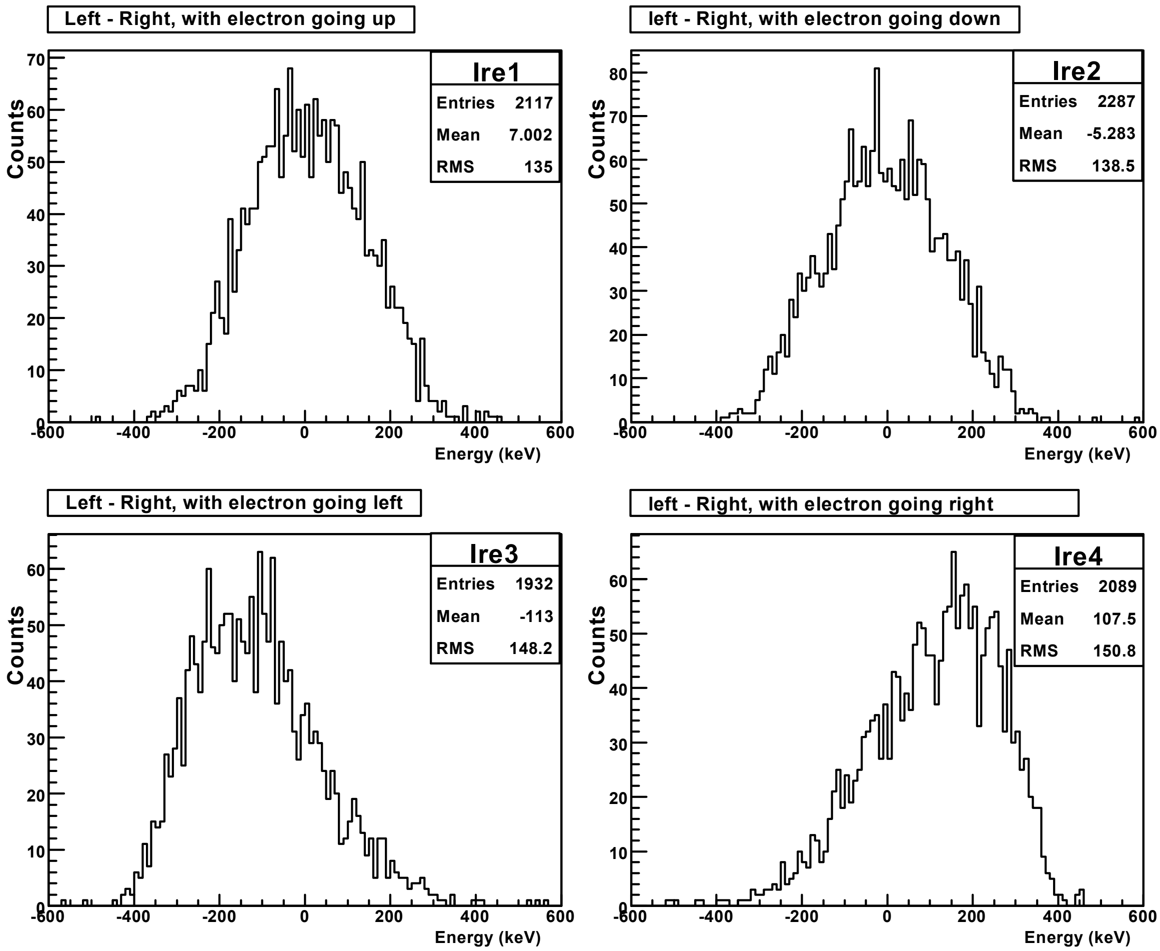

Figure 5.22: Energy difference spectrum of two α particles from left and right DSSDs. The x axis is the left α energy minus the right α energy.

The mean energy shift with left electron direction is noticeably larger than that with right electron direction (as shown in Figure 5.22). This is due to the non-symmetry SD geometry. On the left side between the DSSD and the active SD, there is a dead SD (as shown in Figure 5.10), which should have been removed before the experiment. Electrons need to pass through this extra 1 mm Si in order to be detected by the active SD, so the electrons detected by the left detector have larger average energy than the right side, therefore the recoiling ^{8}Be has a greater momentum. Because of the asymmetric properties, the spectra cannot be combined. The comparison of the α energy difference spectrum with the simulated spectra, with electrons detected on the left side is shown in Figure 5.23, and the spectrum when the electrons detected on the right side is shown in Figure 5.24.

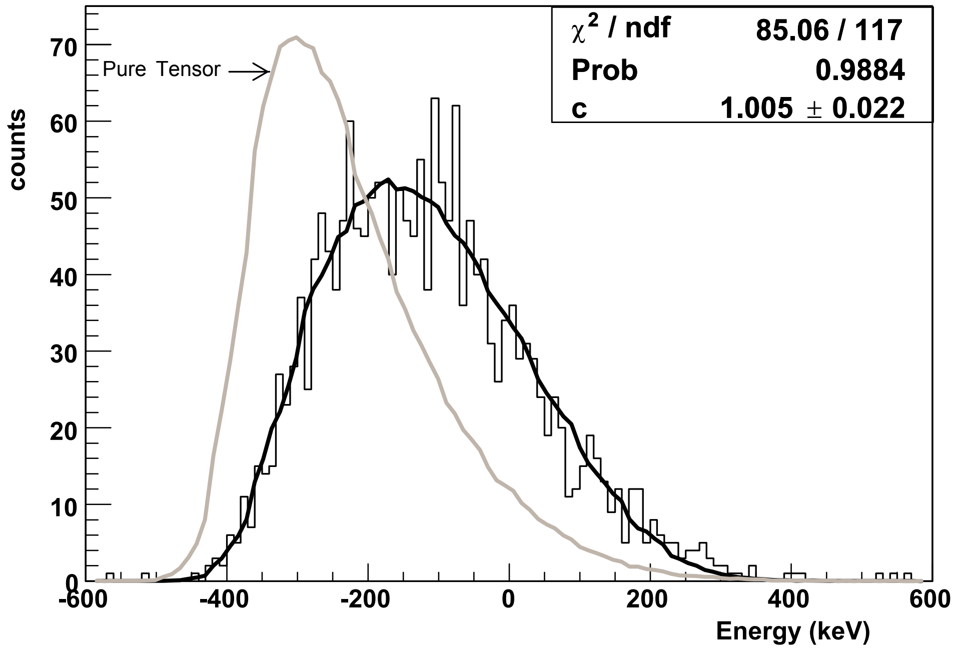

Figure 5.23: The result from left and right DSSDs with betas going left. The data are the alpha energy difference spectrum from left and right DSSDs, with electrons detected by the left 1mm silicon detector. The grey line is the lineshape for a pure tensor interaction and the black line is the lineshape for a pure axial-vector interaction. The fit result is shown in the text box.

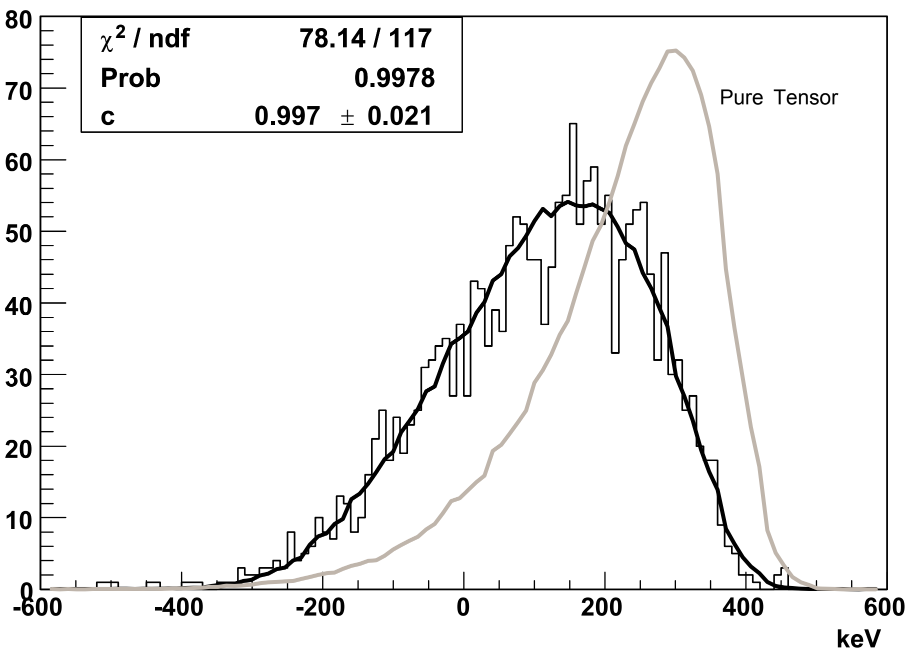

Figure 5.24: The result from left and right DSSDs with betas going right. The data are the alpha energy difference spectrum from left and right DSSDs, with electrons detected by the right 1mm silicon detector. The grey line is the lineshape for a pure tensor interaction and the black line is the lineshape for a pure axial-vector interaction. The fit result is shown in the text box.

The results from these three measurements are:

from Top and Bottom detectors, Figure 5.21: $c_1 \pm \Delta c_1 = 1.000 \pm 0.012_{stat}$

from Left and Right detectors, Figure 5.23: $c_2 \pm \Delta c_2 = 1.005 \pm 0.022_{stat}$

from Left and Right detectors, Figure 5.24: $c_3 \pm \Delta c_3 = 0.997 \pm 0.021_{stat}$

The final result is combined in the following way.

The combined statistical error:

$$\Delta c = \sqrt{\frac{1}{\frac{1}{\Delta c_1^{\,2}} + \frac{1}{\Delta c_2^{\,2}} + \frac{1}{\Delta c_3^{\,2}}}} = 0.009 \qquad (5.10)$$

The combined value of parameter c is weighted by its statistical error:

$$c = \left(\frac{c_1}{\Delta c_1^{\,2}} + \frac{c_2}{\Delta c_2^{\,2}} + \frac{c_3}{\Delta c_3^{\,2}}\right)\Delta c^2 = 1.000 \qquad (5.11)$$

This result does not include systematic uncertainties which will be discussed next.

5.4 Systematic uncertainties

Source	Uncertainty	Δc %	Method
beta scattering	15%	0.3	Geant4
ion cloud distribution	see text	0.3	data and Geant4
ion cloud temperature	see text	0.1	calculation and Geant4
DSSD energy calibration	5 keV	0.5	data
dead layer (Top&Bottom)	0.5 μm	0.5	data
dead layer (Left&Right)	1.0 μm	0.8	data
β energy in DSSD	10%	0.3	Geant4
gap effect on DSSD	see text	0.1	data
detector location	0.1 mm	0.1	off-line measurement

Table 5.3. Dominant sources of systematic uncertainties.

Table 5.3 lists all the major systematic uncertainties on the value of c in equation (5.8). Each item discussed above is independent; therefore the total systematic error is the square root of the quadratic sum of all of the individual items. Each of these uncertainties is discussed in the following section. It is also verified that the sensitivity of each uncertainty to the value of c is negligible at the current precision level.

Beta Scattering: Beta scattering can be a significant source of systematic uncertainties. β particles can be scattered towards the detectors by electrodes, trap frame, etc. The Geant4 simulation includes the most relevant trap geometry and material. The simulation indicates that about 8% α-α-β coincidences are from scattered betas which otherwise would not be detected. Removing all other materials except for detectors will eliminate all scattering in the simulation. By comparing the data to the simulation without β scattering, we found that scattering contributes 2% correction on the Tensor coupling in fits to the data. Considering 10% relative error [84] on the β scattering provided by Geant4, and considering 5% uncertainty of the geometry construction in Geant4 (for example the cables, screws are not included), the uncertainty induced by β scattering is estimated to be 0.3%.

Ion cloud distribution: Section 5.1 discussed the ion cloud distribution. Assuming a Gaussian distribution, by changing the FWHM for a large range of 0－1.8 mm only affects the fitting value by 0.3%. The width of 1.8 mm is determined by the strip pattern distribution as discussed in section 5.1.2. Another tested distribution is the uniform distribution. No matter what distribution is selected, the characteristic size of this distribution can be determined by the strip number difference spectrum as Figure 5.2. Replacing the Gaussian distribution with the uniform distribution changes the fitting value by 0.1%. A distribution indicated in Figure 5.3 will be between the Gaussian and uniform distribution. Therefore 0.3% is the estimated uncertainty from ion cloud distribution. In all other data analysis the Gaussian distribution of 1.8 mm FWHM is used.

Ion cloud temperature: The ion cloud temperature is neglected in the simulation. The ions thermal temperature can be estimated in several ways. Firstly, ions lose energy through collision with the helium buffer gas which is cooled by liquid nitrogen circulating in the trap frame. Ideally at thermal equilibrium of the buffer gas, the thermal energy of ^{8}Li ions will be about

$$E_K = 3/2kT = 0.01\ eV \tag{5.12}$$

where T is at liquid nitrogen temperature. Due to RF heating [51] the actual ion temperature will certainty be higher than the thermal equilibrium energy of the buffer gas. As discussed in section 5.1 most ions are located within ±1 mm in all direction. Considering that in the axial direction ions are confined by the DC potential described in Figure 3.13,

$$V_Z = 0.033z^2 - 42.4(Volt) \tag{5.13}$$

where z is the displacement in mm along axial direction and V_Z is DC potential, the maximum kinetic energy which will allow ions to be confined within ±1 mm is 0.03 eV. In the radial direction the kinetic energy can be estimated by the pseudo-potential model described in section 2.2.3. From formula (2.32) and (2.33), the maximum kinetic energy of ^{8}Li ions will be

$$E_{k(\max)} = e\bar{D}_{u(r_0=1mm)} = \frac{e^2V^2}{4m_{Li}r_{eff}^2\omega^2} = 0.03 \text{ eV} \tag{5.14}$$

where V=450 Volt is the RF voltage applied on the electrodes, r_{eff} = 19.9 mm is the effective distance from electrode to trap center, ω is the RF frequency at 2.01 MHz. The estimated kinetic energies in both axial and radial direction are consistent. RF heating increases the ions energy in the radial direction and the kinetic energy can be transferred to the axial direction through collisions with the buffer gas. In comparison with the ^{8}Be average kinetic energy of 4-5 keV, the initial ^{8}Li temperature is negligible.

DSSD energy calibration: The DSSD energy calibration is one major uncertainty because the energy difference spectrum directly relies on the energy calibration. Formula (5.6) is used to select the peak position. The position selected in this way is usually 2 to 4 channels higher than the position of the highest point of the alpha energy spectrum. The highest point location tends to be a little lower than the real peak position due to the low energy tail, while the position selected by (5.6) tends to be a little higher because the energy resolution of the pulser signal can only be smaller than the α particle energy resolution. The range between these two positions is the uncertainty range. The calibration error is tested by moving the peaks of the calibration sources within this uncertainty range. The calibration function obtained from the two sources is:

$$E_\alpha = k \cdot x + E_0 = \frac{E_{Cm} - E_{Gd}}{x_{Cm} - x_{Gd}} \cdot x + \frac{E_{Gd}x_{Cm} - E_{Cm}x_{Gd}}{x_{Cm} - x_{Gd}} \tag{5.15}$$

where x is the ADC readout value, E_{CM} and E_{Gd} are alpha energies from calibration sources after the dead layer correction. If both peaks of ^{148}Gd and ^{244}Cm are moved in the same direction, only E_0 is affected and this effect will be cancelled in the energy difference spectrum of two alphas. If the two calibration peak positions are not moved in the same direction, the slope k in the calibration function (5.15) is affected. In this case, the fitted value of axial-vector component c is affected by 0.5%.

Dead layer: The DSSD dead layer is another major uncertainty. The dead layer affects the result in the sense that low energy alphas lose more energy than high energy alphas in dead layer (as seen in Figure 5.13), so a thicker dead layer used in the calculation will give a smaller average energy shift between two alphas. The dead layer uncertainty is tested by varying the thickness in the uncertainty range. In each pair of DSSDs this test is done in several ways: changing dead layer in one DSSD or changing dead layer in two DSSDs in the same direction or in a different direction. The maximum effect on the fit result is 0.5% for Top and Bottom DSSDs and 0.8% for Left and Right DSSDs.

β energy in DSSD: In the current setup, the electron direction is obtained from the 1 mm thick single detectors behind the DSSD. The electron deposits about 100 keV energy in the DSSD but the position on the DSSD cannot be identified. There is about 7% chance that the β will hit the same strip as one α. The energy difference spectrum of two alphas is slightly enlarged by about 5 keV because of the β energy deposit. This is also included in the simulation but considering 10% uncertainty of Geant4 simulation, this effect will give 0.3% uncertainty on the value of c.

Gap effect on DSSD: Although most events from the gap can be distinguished by comparing the energy on both front and back side, the energy spectrum of gap events could extend to the full energy (Figure 5.15). The data analysis requires the ratio of front side energy over back side energy to be less than 1.15. Some gap events will still fall in this window, but the energy of these events will be very close to the full energy, and therefore will have little effect. By changing this ratio from 1.1 to 1.2, the result is affected by 0.001.

Detector location: Detector location is measured offline and can also be corrected by the strip difference spectrum as shown in Figure 5.8. Within ±0.1 mm uncertainty of detector position, this effect is studied in the simulation and the result is affected by less than 0.1%.

5.5 Limit of the tensor interaction

Considering the statistical uncertainty discussed in section 5.3 and the systematic uncertainties discussed in section 5.4, the axial-vector component c in equation (5.8) is:

$$c = 1.000 \pm 0.009_{stat} \pm 0.010_{syst} \tag{5.16}$$

From Holstein's equation (53) and the expressions of the spectral functions of this equation in appendix B of Ref. [34], the ratio of $(1-c)/c$ represents the relative intensities of the coupling constants $|C_T^2 / C_A^2|$, with the value of

$$|C_T^2 / C_A^2| = (1-c)/c = 0.000 \pm 0.009_{stat} \pm 0.010_{syst} \tag{5.17}$$

The tensor contribution is constrained to $|C_T / C_A| \leq 0.12$ (at a 68% confidence level), consistent with the Standard Model prediction.

5.6 β-ν angular correlation coefficient $\boldsymbol{a}_{\beta\nu}$

The β-ν angular correlation coefficient $a_{\beta\nu}$ is inferred from the result of $|C_T^2 / C_A^2|$.

The expression of $a_{\beta\nu}$ in equation (1.17) is in the allowed approximation. Due to the large decay Q value and light nucleus mass, the recoil order corrections are relatively large and they contribute several percent corrections to the angular correlation parameters. Many of these terms are proportional to the weak magnetism form factor b_M and the induced tensor form factor g_{II}. The weak magnetism b_M of ^{8}Li has been measured to be 60 ± 1.6 [85], a result that is consistent with the conserved-vector-current hypothesis prediction [33,85]. A recent experimental limit of g_{II} from the A=8 system is $g_{II}/g_A = -0.28 \pm 0.32$ [86], in which g_A is the axial-vector coupling constant, and thus is negligible in our current precision.

The calculation of $a_{\beta\nu}$ including the recoil order terms is based on Holstein's equation (53) [34],

$$a_{\beta\nu} = \int_0^{E_{end}} \frac{g_2(E)}{g_1(E)} f(E) dE = -0.329 \tag{5.18}$$

in which $f(E)$ is the normalized β energy distribution with end point energy E_{end}, extracted from the β energy spectrum in Figure 4.3. $g_2(E)$ and $g_1(E)$ are spectral functions defined in Ref. [34]. Including both the statistical and systematic uncertainties, the β-ν angular correlation coefficient is:

$$a_{\beta\nu} = -0.329 \pm 0.009 \tag{5.19}$$

5.7 β-ν angular distribution

In principle the β-ν angular correlation coefficient can also be extracted from the β-ν angular distribution, which is the most intuitive picture of $a_{\beta\nu}$. However, until now no experiment has used this spectrum directly to obtain the β-ν angular correlation coefficient $a_{\beta\nu}$. In most of the completed experiments (refer to Figure 1.2), the entire decay kinematics were not fully determined; therefore the neutrino momentum could not be extracted. Some experiments, for example the ^{38m}K measurement [29], were able to extract the β-ν angular distribution, but the final result of $a_{\beta\nu}$ was still obtained from some other observable which is more sensitive to the exotic interactions. In our experiment, because the β particle direction is not detected by DSSDs and the α angle resolution is limited by the DSSD strip width, the angle between the neutrino and the electron is rather poorly determined. Due to the poor angular resolution of α and β particles, the β-ν angle distribution spectrum cannot be used to set a limit on the tensor interaction that is comparable to that obtained from the energy difference spectra. Nevertheless, useful information can be obtained by comparing the data to the simulation, and the β-ν angle distribution is in agreement with pure axial-vector coupling and not with the tensor coupling. The angle distributions constructed from the top-bottom pair of detectors, and from left-right pair of detectors are shown in Figure 5.25 and Figure 5.26 respectively.

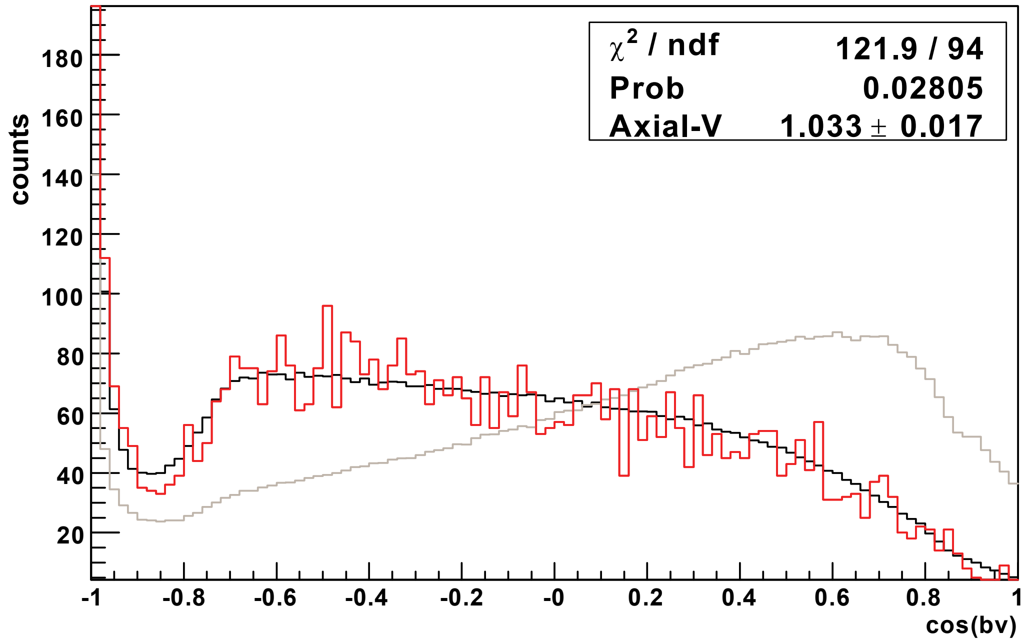

Figure 5.25: Distribution of angle between β and ν obtained from top and bottom detectors, compared with simulation. The red line shows the data from top and bottom pair of detectors, with alphas detected by the top and bottom DSSDs and with the electrons detected by top or bottom single silicon detectors. The black line is the Geant4 simulation assuming pure axial-vector coupling, and the gray line is the simulation assuming pure Tensor coupling. The sharp peak at around -1 corresponds to β and ν emitted oppositely. In this case, the two α particles have minimum energy shift, so the events in this case are badly separated.

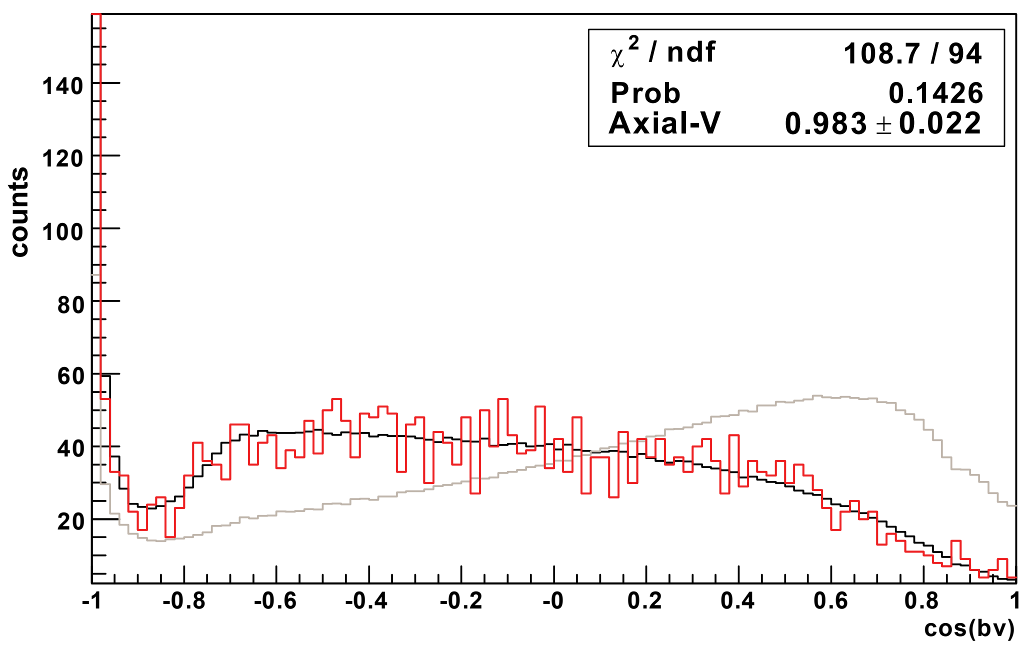

Figure 5.26: Distribution of angle between β and ν obtained from left and right detectors, compared with simulation. The red line shows the data from left and right pair of detectors. The black line is the Geant4 simulation assuming pure axial-vector coupling, and the gray line is the simulation assuming pure Tensor coupling.

Chapter 6 Summary and outlook

6.1 Summary

In this thesis we have demonstrated the use of the ion trap technology for a precision β-ν angular correlation measurement. Data were taken for 20 hours with a total of about 20,000 α-α-β coincidence events recorded. The measured β-ν angular correlation coefficient a can be expressed as $a_{\beta\nu} = -0.333 \pm 0.009$. With relatively few events the statistics uncertainty reached the 1% level. This is mainly because that the alphas energy-difference spectrum is very sensitive to the tensor interaction. The result is consistent with the Standard Model and the tensor contribution is constrained to the level of 12% (at 68% confidence level) in this measurement. The comparison of our measurement with other measurements in history is shown in Figure 6.1. The present upper limit of the tensor interaction is 8% (at 95% CL) obtained from a global analysis [11], which is mainly determined from the very precise β-ν angular correlation measurement of ^{6}He in 1963 [23].

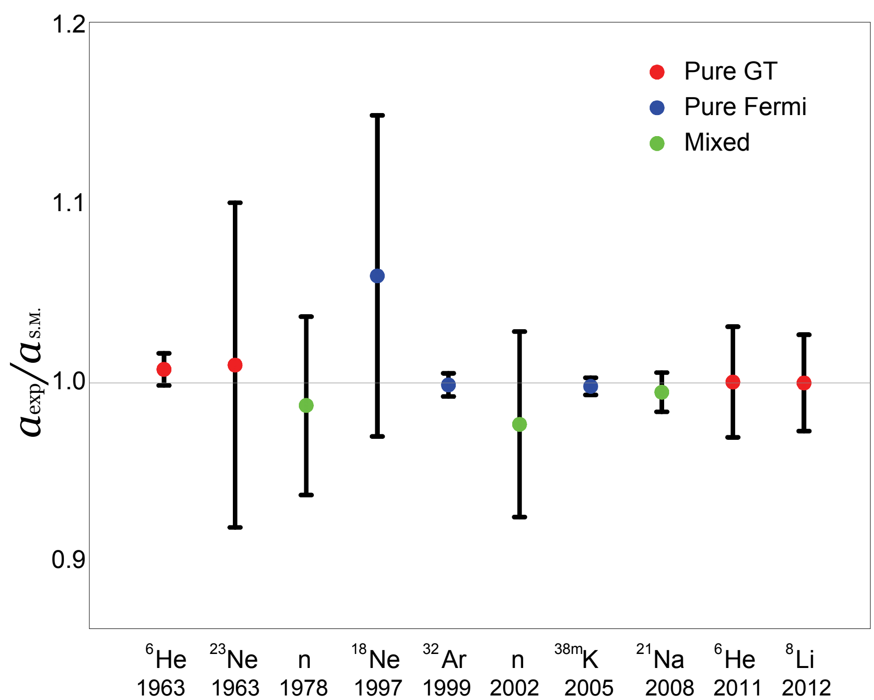

Figure 6.1: World status of β-ν angular correlation $a_{\beta\nu}$ measurements. This is the updated Figure 1.2 with our ^{8}Li result added.

The trap technology, including both Magneto-Optical Traps (MOT) and ion traps, has triggered a series of β-ν correlation measurement in recent years. All the completed measurements with better than 10% precision since 2000 are done in the trap(except for the neutron measurement), and almost all on-going and new proposed experiments [87] [88] [89] [90] will use the trap technology. The ^{8}Li measurement is the first experiment initiated to measure the β-ν correlation in the Linear Paul trap. (The ^{6}He measurement was the first experiment utilizing an ion trap with solely RF voltage.) MOTs are able to confine atoms with smaller size and at much lower temperature but are usually limited to alkali elements, and the efficiencies with noble gas atoms are quite low. However, the ion trap can confine all kinds of ions and the trap efficiency is much higher than MOTs. It should be noted that for the Linear Paul trap the efficiency is usually >90% because the ions are not subject to an RF retarding and accelerating field. The Linear Paul trap can also be used to measure any appropriate radioactive ions.

This measurement is the first and preliminary result of our experiment and there is room for many improvements. The ^{8}Li has been demonstrated to be a very promising candidate for the β-ν correlation measurement. The goal of the future β-ν correlation measurement with the BPT is aiming at 0.1% level.

6.2 System upgrade

The high precision β-ν angular correlation measurement using ^{8}Li requires high statistics, precise detection of decay products and small ion cloud size. The improvements focus on these three aspects.

6.2.1 Improvement of transmission efficiency

The transmission efficiency is currently limited by the gas catcher saturation. The ^{7}Li beam intensity used during the experiment was 6 electrical nano-amps (enA) while the available beam intensity could be up to 60 enA. Increasing beam intensity does not increase the collected ^{8}Li ions because of the saturation in the gas catcher. A new gas catcher has been built and will be installed for future experiments. The electrodes of the new gas catcher are more closely spaced allowing a higher RF frequency, which should greatly improve the transmission efficiency for light ions.

6.2.2 Upgrade of the detector system

6.2.2.1 New DSSD

The main upgrade of the detector system is the replacement of the 300 μm thick 16×16 strips DSSD. The new DSSD is also manufactured by Micro of model BB7 type 7p [68]. It has 32×32 strips on each side with 64×64 mm^2 active area and 1 mm thickness. The dead layer is requested to be around 0.1 μm.

Increasing the thickness of the DSSD will allow us to record electron signals in the DSSD. In the 300 μm DSSD, an electron deposits about 100 keV energy and the electron signal shows up in most strips on the junction side, while the signal cannot be well separated from noise on the ohmic side. In the current setup, the electron direction is obtained from the SD behind the DSSD. With the new DSSD, most electrons will deposit about 300 keV energy so the electrons will be clearly detected by the DSSD, providing much better angular resolution. As analyzed in section 5.4, not knowing whether electron and alpha hit the same strip will contribute a 0.3% uncertainty, which will not be an issue for the new DSSD. The angular resolution for alpha particles will also be improved by about a factor of 2. The current data analysis relies on the energy spectrum of two alphas, but does not use the alpha angular information because the angular resolution is very poor. The data from the new DSSD might be able to use both energy and angular information, probing the tensor interaction more sensitively. Figure 6.2 compares the Geant4 simulation of β-ν angular distribution, constructed from the two alpha momenta and the beta direction, with the current detector system and the upgraded detector system.

The new DSSD has a dead layer of 0.1 μm, which is due purely to the shallow implant. Currently the 0.6 μm dead layer is one of the main systematic effects which gives 0.5% uncertainty on the value of *a*. This dead layer correction with the new DSSD is expected to be below 0.1%.

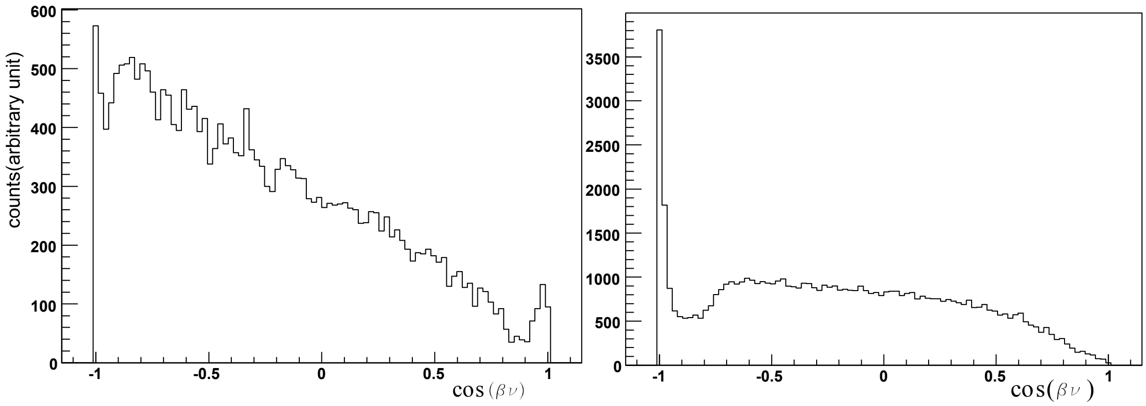

(a) (b)

Figure 6.2: Simulation of the beta-neutrino angular distribution. (a) is constructed by the two alphas momenta and β direction detected by the new DSSDs. (b) is constructed by two alphas momenta detected by present DSSDs and β direction detected by the single silicon detector. The peak around cos(βν)=－1 is due to the DSSDs angular resolution of alpha and beta particles.

6.2.2.2 Plastic scintillator detector

Four plastic scintillator detectors of about 12×12×12 cm^3 have been designed and will be used in the future experiment to detect the β energy. Knowing the β energy will overconstrains the entire decay kinematics. With higher statistics it will be possible to carry out internal systematic checks. For example, the data can be cut on high energy β's to study the energy shift of alphas because in this case the neutrino has little effect, which simplifies the kinematics. As pointed out in section 4.3.2, calculating the β and the neutrino momenta from the two alpha momenta and beta direction will give two solutions from the quadratic equation of energy and momentum conservation. Without knowing the β energy, there are about 0.15% cases in which we cannot know which is the correct solution. Detecting the β energy will provide enough information to select the unique solution.

6.2.2.3 Precise calibration source

Energy calibration contributes another major uncertainty. As Figure 5.11 and Figure 5.12 show, the difficulty of energy calibration is mainly due to the thickness of the calibration sources. As a preliminary experiment, theses sources were not specially designed to be thin. If a 0.1% level measurement is to be made in the future, better calibration sources will be necessary.

6.2.3 Improve trapping properties

6.2.3.1 Optimize trap operation

The trap was operated at 2.13 MHz, 850 $V_{peak\text{-}to\text{-}peak}$, corresponding to the q value defined at section 2.3 of

$$q = \frac{2eV}{m\Omega^2 r_0^2} = 0.13$$

This is a relatively low q value for a linear Paul trap. Although theoretically any point in the stability region in Figure 2.7 can be used to operate a trap, a trap is usually operated at around q=0.4. Based on the Brownian-motion model [91], the q value as low as 0.1 may increase the ion cloud size [92]. The spatial distribution of the ion cloud density might be represented as two separate peaks instead of one peak at the trap center as shown in Figure 5.3 [76].

Operating the trap with this condition is partially due to the compromise between the RF pick-up and the properties of the ion cloud. Section 3.10.5 indicated that higher frequency is helpful for the suppression of RF pick-up. Further reducing the RF pick-up will simplify the trap voltage tuning and smaller ion cloud size is expected with higher q value.

6.2.3.2 H_2 buffer gas

The "RF heating" [51] phenomenon limits the final ion cloud size [92]. The heating is worse when the ion mass is comparable with the buffer gas. The DSSD and two α particles offer an excellent way to monitor the ion cloud size. The ^{8}Li ion cloud is approximately equivalent to a Gaussian distribution of 1.8 mm FWHM as analyzed in section 5.1. The mass ratio of ^{8}Li to the helium buffer gas is only 2, so if H_2 is used as a buffer gas the ion cloud is expected to be smaller. Trapping and cooling ions as light as $^4He^+$ and $^6He^+$ have been demonstrated using H_2 buffer gas at GANIL [93] [31]. Special cautions are necessary if H_2 is used as a buffer gas due to safety issues.

6.2.3.3 Minimize beta scattering

Beta scattering is an important systematic uncertainty in many β-ν angular correlation measurements. Currently 8% coincidence events are from scattered beta particles and this contributes 0.3% uncertainty. Replacing the current stainless steel electrodes and trap mounting frame with lighter material, such as gold plated aluminium, or even beryllium will significantly reduce the beta scattering. With the updated detector system, the decay kinematics is overconstrained, which will also help to identify the scattered events.

6.3 Future physics goals

Conserved-vector-current and second-class currents studies

The current system can also be used to measure the β-decay of the mirror nucleus of ^{8}Li: ^{8}B. Comparing the angular correlations of decay products in the mass 8 system presents an excellent opportunity [94] to test the Conserved Vector Current (CVC) [10] hypothesis and search for the possible existence of the Second Class Currents (SCC) [95]. The CVC hypothesis is analogous to the electromagnetic current conservation, stating that the vector current of the weak interaction is not influenced by the strong interactions. The SCC is defined as the induced terms with a different G-parity symmetry from the strong interaction and these are expected to be absent in the Standard Model [96].

The CVC and SCC terms cause small shifts in the directional correlation of β-decay in ^{8}Li→^{8}Be*←^{8}B and the subsequent α particles [34]. Previously the CVC test measurement in the mass 8 system mainly focused on the β-α angular correlation [97] [98] [99] or the β-ray angular correlation of aligned ^{8}Li and ^{8}B [100]. These two methods have intrinsic similarity because β-delayed α particle emission is related to the spin alignment of the daughter nucleus ^{8}Be. In the BPT, the complete reconstruction of the decay allows a measurement of the β-ν，β-α and β-ν-α angular correlations (which each have different CVC and SCC terms) in a single experiment.

Glossary

terms	Explanation	Page
S	Scalar	13
P	Pseudoscalar	13
V	Vector	13
A	Axial Vector	13
T	Tensor	13
V-A	Vector − Axial vector description of weak interaction	16
CKM	Cabibbo-Kobayashi-Maskawa	18
RFQ	Radio Frequency Quadrupole	28
RF	Radio Frequency	29
CPT	Canadian Penning Trap	45
ANL	Argonne National Laboratory	45
BPT	Beta-decay Paul Trap	45
ATLAS	Argonne Tandem Linac Accelerator System	45
C.M.	Center of Mass frame	48
MCP	MicroChannel Plate detector	53
DSSD	Double-sided Silicon Strip Detector	61
SD	1 mm thick unsegmented Silicon Detector	61
LN_2	Liquid Nitrogen	66
MOT	Magneto-Optical Traps	118
enA	electrical nano-Amps	118

LIST OF REFERENCES

[1] E. Fermi, Zeitschrift Fur Physik **88**, 161-177 (1934).

[2] C. Strachan, *The Theory of Beta-decay*, [1st ed.]. (Pergamon Press, Oxford;New York, 1969).

[3] W. Pauli, *Die Allgemeinen Prinzipien Der Wellenmechanik* (Springer Verlag, 1933).

[4] T. D. Lee and C. N. Yang, Phys. Rev. **104**, 254-258 (1956).

[5] C. S. Wu, E. Ambler, R. W. Hayward, D. D. Hoppes, and R. P. Hudson, Phys. Rev. **105**, 1413-1415 (1957).

[6] R. L. Garwin, L. M. Lederman, and M. Weinrich, Phys. Rev. **105**, 1415-1417 (1957).

[7] J. I. Friedman and V. L. Telegdi, Phys. Rev. **105**, 1681-1682 (1957).

[8] E. C. G. Sudarshan and R. E. Marshak, in (1957).

[9] E. C. G. Sudarshan and R. E. Marshak, Phys. Rev. **109**, 1860 (1958).

[10] R. P. Feynman and M. Gell-Mann, Phys. Rev. **109**, 193 (1958).

[11] N. Severijns, M. Beck, and O. Naviliat-Cuncic, Rev. Mod. Phys. **78**, 991-1040 (2006).

[12] G. Sheldon L., Nuclear Physics **22**, 579-588 (1961).

[13] S. Weinberg, Phys. Rev. Lett. **19**, 1264-1266 (1967).

[14] A. Salam and J. C. Ward, Physics Letters **13**, 168-171 (1964).

[15] M. Kobayashi and T. Maskawa, Progress of Theoretical Physics **49**, 652-657 (1973).

[16] E. D. Commins and P. H. Bucksbaum, *Weak Interactions of Leptons and Quarks* (Cambridge University Press, 1983).

[17] J. D. Jackson, S. B. Treiman, and H. W. Wyld, Phys. Rev. **106**, 517 (1957).

[18] M. Fierz, Zeitschrift Für Physik **104**, 553-565 (1937).

[19] J. C. Hardy and I. S. Towner, Phys. Rev. C **79**, 055502 (2009).

[20] W. B. Herrmannsfeldt, D. R. Maxson, P. Stähelin, and J. S. Allen, Phys. Rev. **107**, 641-643 (1957).

[21] C. S. Wu and A. Schwarzschild, *a Critical Examination of the He-6 Recoil Experiment of Rustad and Ruby* (Columbia University, New York, 1958).

[22] J. S. Allen, R. L. Burman, W. B. Herrmannsfeldt, P. Stähelin, and T. H. Braid, Phys. Rev. **116**, 134-143 (1959).

[23] C. H. Johnson, F. Pleasonton, and T. A. Carlson, Phys. Rev. **132**, 1149 (1963).

[24] T. A. Carlson, Phys. Rev. **132**, 2239-2242 (1963).

[25] C. Stratowa, R. Dobrozemsky, and P. Weinzierl, Phys. Rev. D **18**, 3970-3979 (1978).

[26] V. Egorov et al., Nuclear Physics A **621**, 745 (1997).

[27] E. G. Adelberger et al., Phys. Rev. Lett. **83**, 1299 (1999).

[28] J. Byrne, P. G. Dawber, M. G. D. van der Grinten, C. G. Habeck, F. Shaikh, J. A. Spain, R. D. Scott, C. A. Baker, K. Green, and O. Zimmer, Journal of Physics G: Nuclear and Particle Physics **28**, 1325-1349 (2002).

[29] A. Gorelov et al., Phys. Rev. Lett. **94**, 142501 (2005).

[30] P. A. Vetter, J. R. Abo-Shaeer, S. J. Freedman, and R. Maruyama, Phys. Rev. C **77**, 035502 (2008).

[31] X. Fléchard, E. Liénard, A. Méry, D. Rodríguez, G. Ban, D. Durand, F. Duval, M.

Herbane, M. Labalme, F. Mauger, O. Naviliat-Cuncic, J. C. Thomas, and P. Velten, Phys. Rev. Lett. **101**, 212504 (2008).
[32] N. Severijns and O. Naviliat-Cuncic, Annu. Rev. Nucl. Part. Sci. **61**, 23 (2011).
[33] L. Grenacs, Annu. Rev. Nucl. Part. Sci. **35**, 455 (1985).
[34] B. R. Holstein, Rev. Mod. Phys. **46**, 789 (1974).
[35] A. Sirlin, Phys. Rev. **164**, 1767-1775 (1967).
[36] F. Glück, Comp. Phys. Commun. **101**, 223 (1997).
[37] E. K. Warburton, Phys. Rev. C **33**, 303 (1986).
[38] W. T. Winter, S. J. Freedman, K. E. Rehm, and J. P. Schiffer, Phys. Rev. C **73**, 025503 (2006).
[39] R. Wiringa, (private communication).
[40] E. T. H. Clifford et al., Phys. Rev. Lett. **50**, 23 (1983).
[41] V. Vorobel et al., Eur. Phys. J. A **16**, 139 (2003).
[42] K. Siegbahn, *Alpha- Beta- and Gamma-ray Spectroscopy* (North-Holland Pub. Co., 1965).
[43] M. Morita, Phys. Rev. Lett. **1**, 112 (1958).
[44] C. Barnes, Phys. Rev. Lett. **1**, 328 (1958).
[45] R. F. Christy, E. R. Cohen, W. A. Fowler, C. C. Lauritsen, and T. Lauritsen, Phys. Rev. **72**, 698-711 (1947).
[46] K. H. Lauterjung, B. Schimmer, and H. Maier-Leibnitz, Zeitschrift Für Physik **150**, 657-659 (1958).
[47] T. Lauritsen, C. A. Barnes, W. A. Fowler, and C. C. Lauritsen, Phys. Rev. Lett. **1**, 326-328 (1958).
[48] D. R. Denison, Journal of Vacuum Science and Technology **8**, 266 (1971).
[49] I. E. Dayton, F. C. Shoemaker, and R. F. Mozley, Review of Scientific Instruments **25**, 485-489 (1954).
[50] P. H. Dawson, Journal of Vacuum Science and Technology **8**, 263 (1971).
[51] H. G. Dehmelt, Advances In Atomic And Molecular Physics **3**, 53-72 (1967).
[52] R. E. March and J. F. Todd, *Quadrupole Ion Trap Mass Spectrometry , 2nd Edition*, 2nd ed. (Wiley-Interscience, 2005).
[53] V. Fernande, International Journal of Mass Spectrometry and Ion Processes **106**, 33-61 (1991).
[54] R. E. March, in (San Antonio, TX, 1984), pp. 513-514.
[55] M. Drewsen and A. Brøner, Phys. Rev. A **62**, 045401 (2000).
[56] Y. Xia, X. Liang, and S. A. McLuckey, Anal. Chem. **77**, 3683-3689 (2005).
[57] G. G. Dolnikowski, M. J. Kristo, C. G. Enke, and J. T. Waston, Int. J. Mass Spectrom. Ion Proc. **82**, 1 (1988).
[58] D. J. Douglas, A. J. Frank, and D. Mao, Mass Spectrom Rev **24**, 1-29 (2005).
[59] G. Savard et al., Nuclear Physics A **626**, 353 (1997).
[60] N. D. Scielzo et al., Nucl. Instr. and Meth. A **681**, 94 (2012).
[61] W. F. Henning, Nuclear Physics News **5**, 12-22 (1995).
[62] *ATLAS Website* (http://www.phy.anl.gov/atlas/userbook/accelfacilities.html).
[63] Y. Han, *Calculation and Analysis of d+7Li Reaction* (International Atomic Energy Agency Nuclear Data Services, n.d.), pp. 45-52.
[64] J. P. Schiffer, G. C. Morrison, R. H. Siemssen, and B. Zeidman, Phys. Rev. **164**, 1274-1284 (1967).

[65] M. Reiser, *Theory and Design of Charged Particle Beams* (Wiley-VCH, 2008).
[66] G. Savard et al., Nucl. Instr. and Meth. B **204**, 582 (2003).
[67] G. Savard et al., Phys. Lett. A **158**, 247 (1991).
[68] *Micron Semiconductor, Ltd* (www.micronsemiconductor.co.uk).
[69] *Rutherford Appleton Laboratory* (www.ssd.rl.ac.uk).
[70] P. Wilt, in *Electronics for the Si Detectors in APEX* (Fourth Annual Electronics for Future Colliders Conference, Chestnut Ridge, NY, 1994).
[71] *Scarlet Documents* (http://www.phy.anl.gov/scarlet/).
[72] E. H. Rhoderick and R. H. Williams, *Metal-Semiconductor Contacts*, 2nd ed. (Oxford University Press, USA, 1988).
[73] *GEANT4 2005* (http://geant4.web.cern.ch/geant4).
[74] N. D. Scielzo, S. J. Freedman, B. K. Fujikawa, and P. A. Vetter, Phys. Rev. Lett. **93**, 102501 (2004).
[75] M. Bhattacharya, E. G. Adelberger, and H. E. Swanson, Phys. Rev. C **73**, 055802 (2006).
[76] J. Hou, Y. Wang, and D. Yang, J. Appl. Phys **88**, 4334 (2000).
[77] H. W. Ellis, R. Y. Pai, E. W. McDaniel, E. A. Mason, and L. A. Viehland, Atomic Data and Nuclear Data Tables **17**, 177-210 (1976).
[78] *Gas Correction Factors for Ionization Vacuum Gauges, MKS Instruments.* (http://www.mksinst.com/docs/UR/gaugeGasCorrection.aspx).
[79] *Simion7* (http://simion.com/).
[80] *Srim* (http://www.srim.org/#SRIM).
[81] J. Yorkston, A. C. Shotter, D. B. Syme, and G. Huxtable, Nucl. Instr. and Meth. A **262**, 353 (1987).
[82] G. Cowan, *Statistical Data Analysis* (Oxford University Press, USA, 1998).
[83] V. A. Muravsky, S. A. Tolstov, and A. L. Kholmetskii, Nuclear Instruments and Methods in Physics Research Section B: Beam Interactions with Materials and Atoms **145**, 573-577 (1998).
[84] S. A. Hoedl, Ph.D. Thesis, Princeton University, 2003.
[85] T. Sumikama et al., Phys. Rev. C **83**, 065501 (2011).
[86] T. Sumikama et al., AIP Conference Proceedings **915**, 230 (2007).
[87] P. Müller, in (Advances in Radioactive Isotope Science, Belgium, Brussels, 2011).
[88] S. Vaintraub, M. Hass, O. Aviv, O. Heber, and I. Mardor, arXiv:1005.4145 (2010).
[89] H. W. Wilschut and K. Jungmann, Nuclear Physics News **17**, 11-15 (2007).
[90] M. Beck, S. Coeck, V. Y. Kozlov, M. Breitenfeld, P. Delahaye, P. Friedag, M. Herbane, A. Herlert, I. S. Kraev, J. Mader, M. Tandecki, S. Van Gorp, F. Wauters, C. Weinheimer, F. Wenander, and N. Severijns, arXiv:1008.0207 (2010).
[91] R. Blatt, P. Zoller, G. Holzmuller, and I. Siemers, Zeitschrift Für Physik D Atoms, Molecules and Clusters **4**, 121-126 (1986).
[92] I. Siemers, R. Blatt, T. Sauter, and W. Neuhauser, Phys. Rev. A **38**, 5121-5128 (1988).
[93] G. Ban, G. Darius, D. Durand, X. Fléchard, M. Herbane, M. Labalme, E. Liénard, F. Mauger, O. Naviliat-Cuncic, C. Guénaut, C. Bachelet, P. Delahaye, A. Kellerbauer, L. Maunoury, and J. Y. Pacquet, Nuclear Instruments and Methods in Physics Research Section A: Accelerators, Spectrometers, Detectors and Associated Equipment **518**, 712-720 (2004).

[94] L. Grenacs, Annual Review of Nuclear and Particle Science **35**, 455-500 (1985).
[95] S. Weinberg, Phys. Rev. **112**, 1375-1379 (1958).
[96] P. Langacker, Phys. Rev. D **15**, 2386-2400 (1977).
[97] R. E. Tribble and G. T. Garvey, Phys. Rev. C **12**, 967-983 (1975).
[98] R. D. McKeown, G. T. Garvey, and C. A. Gagliardi, Phys. Rev. C **22**, 738-749 (1980).
[99] M. Beck, D. W. Storm, D. C. Wright, and Z. Zhao, Proceedings of The 6th Conference on the Intersections of Particle and Nuclear Physcis **412**, 416-418 (1997).
[100] T. Sumikama, K. Matsuta, T. Nagatomo, M. Ogura, T. Iwakoshi, Y. Nakashima, H. Fujiwara, M. Fukuda, M. Mihara, K. Minamisono, T. Yamaguchi, and T. Minamisono, arXiv:1105.1584 (2011).